TECHNISCHE UNIVERSITÄT WIEN
Vienna University of Technology

D I P L O M A R B E I T

Adsorption and Reactivity Studies on Oxide (V_2O_5, Bi_2O_3)-Carbon Nanotube Hybrid materials

Ausgeführt am Institut für

Materialchemie

der Technischen Universität Wien

unter Anleitung von

Univ.Prof. Mag.rer.nat. Dr.rer.nat. Günther Rupprechter

und

Dipl.-Ing. Dr.techn. Karin Föttinger als verantwortlich

mitwirkende Universitätsassistentin

durch

Roman Tiefenthaller

Petrinaweg 4

4840 Vöcklabruck

Österreich

Wien, 31. Oktober 2012

Danksagung

An dieser Stelle möchte ich einigen Personen danken, die zur vorliegenden Arbeit auf unterschiedliche Art beigetragen haben.

Zunächst möchte ich **Prof. Günther Rupprechter** für die Ermöglichung der Diplomarbeit, die interessante Fragestellung und die gute Aufnahme in seiner Arbeitsgruppe danken.

Weiters möchte ich einen besonderen Dank **Dr. Karin Föttinger** ausdrücken, die mir stets fachlich beratend zur Seite stand – egal ob während laufender Experimente oder zur Diskussion der Ergebnisse - und sich bei Bedarf immer für (teils sehr zeit-) intensive Gespräche Zeit genommen hat.

Beiden Betreuern möchte ich auch für die rasche Korrektur der Arbeit danken.

Außerdem gilt mein Dank allen Mitarbeitern des Instituts für Materialchemie, die eine angenehme Arbeitsatmosphäre ermöglichten. Im Besonderen möchte ich hier **Dipl.-Chem.(FH) Sebastian Buhr** und **Dipl. Ing. Astrid Kitla** anführen, die immer ein offenes Ohr für kleinere und größere plötzlich auftretende Probleme hatten.

Dennis Dieterle von der Universität Münster, der die in dieser Arbeit untersuchten Hybridproben hergestellt hat, möchte ich auch ein besonderes Dankeschön sagen.

Auch **Dr. Klaudia Hradil**, die die XRD Messungen und Auswertungen durchgeführt hat, sei hier gedankt.

Ebenfalls möchte ich dem FWF (Fonds zur Förderung wissenschaftlicher Forschung) Danke sagen für die finanzielle Förderung der Diplomarbeit durch den Spezialforschungsbereich (SFB) F45 „Functional Oxide Surfaces and Interfaces (FOXSI)".

Schließlich möchte ich mich bei meinen Eltern, **Mag. Heimo** und **Mag. Margit Tiefenthaller** bedanken, die mir das Studium überhaupt ermöglicht haben und genauso wie mein Bruder **Dr. Gernot Tiefenthaller** immer für diverse Probleme ein offenes Ohr hatten.

Abstract

The goal of the thesis was the characterization of the catalytic performance of new metal oxide - carbon nanotube hybrid materials by adsorption and reactivity studies. Namely, Bi_2O_3 – carbon nanotube and V_2O_5 – carbon nanotube hybrids were investigated and compared to the respective bulk metal oxide powders in order to evaluate the influence of the carbon nanotube support. Pd was added to the samples to decrease the required temperatures for the reactivity studies to prevent combustion of the carbon nanotubes.

The hybrid materials were prepared in several steps: The synthesis of carbon nanotubes (CNTs) in a chemical vapor deposition process was followed by a sol-gel process creating a metal oxide layer on the nanotubes. Calcination at about 300 °C enabled the formation of a crystalline layer. In a final step Pd was impregnated onto the samples.

In this thesis transmission electron microscopy (TEM), temperature programmed reaction (TPReaction), transmission IR spectroscopy of CO and methanol as probe molecules and kinetic studies were the techniques used for characterization of the materials.

TEM revealed a layer like coating of the CNTs by Bi_2O_3, while V_2O_5 was attached to the nanotubes in a more particulate form. Pd was finely dispersed both on the metal oxides and on residual uncovered CNTs.

In TPReaction measurements and kinetic studies the hybrid catalysts were highly active for the methanol oxidation reaction. Compared to the reference bulk metal oxides the hybrids were active already at lower temperatures. The products formed over the respective Pd – metal oxide catalysts were the same. All catalysts were highly selective towards methyl formate at low temperature (<100 °C); however, with increasing temperature the selectivity changed towards CO_2 formation.

FTIR spectroscopy was utilized to identify surface sites and reaction intermediates. CO did not adsorb on Bi_2O_3. After methanol adsorption undissociated methanol, methoxy, formate, dimethyl ether and formaldehyde adsorbed on Pd-Bi_2O_3 were detected. On V_2O_5 V^{4+} and V^{3+} sites were detected after CO adsorption at -110 °C. Methanol adsorption studies on Pd-V_2O_5 samples revealed bands of adsorbed methoxy and formaldehyde species.

Zusammenfassung

Ziel dieser Arbeit war es, neue Hybridmaterialien, die aus Metalloxiden und Kohlenstoffnanoröhren (CNTs) aufgebaut sind, hinsichtlich ihrer katalytischen Eigenschaften zu charakterisieren. Bi_2O_3 – CNT Hybride bzw. V_2O_5 – CNT Hybride wurden hergestellt, mittels Adsorptions- und Reaktivitätsstudien untersucht und mit den jeweiligen Referenzmetalloxiden verglichen. Um aussagekräftige Reaktivitätsstudien bei niedrigen Temperaturen zu ermöglichen ohne die CNTs zu verbrennen, wurden die Proben zusätzlich mit Palladium imprägniert.

Für die Herstellung der Hybride wurden zunächst die CNTs in einem CVD-Prozess synthetisiert, bevor im nächsten Schritt die Metalloxide mittels Sol-Gel Prozess auf den CNTs aufgebracht wurden. Kalzinierung bei ~300 °C resultierte in einer kristallinen Beschichtung der CNTs. Zum Schluss erfolgte die Imprägnierung mit Pd.

Die in dieser Arbeit verwendeten Charakterisierungsmethoden umfassten Transmissions-elektronenmikroskopie (TEM), Temperatur programmierte Reaktion (TPReaktion), Transmissions-Infrarotspektroskopie mit CO und Methanol als Sondenmoleküle, sowie kinetische Messungen.

Mittels TEM konnte die Beschichtung der Nanotubes mit den Metalloxiden untersucht werden: Bi_2O_3 bedeckte die CNTs schichtartig, während bei V_2O_5 eher eine partikuläre Beschichtung festgestellt wurde. Pd war in allen Hybridproben fein verteilt auf den Metalloxidpartikeln und nicht beschichteten Nanoröhren sichtbar.

Als Testreaktion wurde die selektive Methanoloxidation untersucht. Die Hybridmaterialien waren schon bei signifikant niedrigeren Temperaturen aktiv als die jeweiligen Referenzoxide. Hinsichtlich der Produktverteilung konnte kein Unterschied zwischen den Metalloxid - Hybriden und den jeweiligen Referenzoxiden festgestellt werden. Bei niedrigen Temperaturen (~100 °C) und geringen Umsätzen (<50 %) waren alle Katalysatoren hoch selektiv für die Bildung von Methylformiat; jedoch bewirkte die Erhöhung der Temperatur eine zunehmende CO_2-Bildung.

IR-Adsorptionsuntersuchungen zeigten, dass CO auch bei -110 °C nicht an Bi_2O_3 adsorbierte. Die Methanol-Adsorption führte zu verschiedenen Spezies adsorbiert an der Oxidoberfläche: undissoziertes Methanol, Methoxy, Formiat, Dimethylether und Formaldehyd. Auf V_2O_5 hingegen konnten mittels CO-Adsorption bei -110 °C V^{4+} und V^{3+} auf der Oberfläche nachgewiesen werden. Bei der Methanol-Adsorption wurden adsorbierte Methoxy-Spezies und Formaldehyd an der Pd-V_2O_5 – Oberfläche detektiert.

Contents

1 Introduction

1.1 Historical Development of Catalysis and Its Significance Today

According to its definition 'catalysis' is described as a process, where a substance called catalyst increases the rate of the reaction without altering the overall standard Gibbs energy change of the reaction. At the end of the reaction the catalyst regains its initial state. Catalysis is divided into two groups: homogenous and heterogeneous catalysis. While in homogeneous catalysis all reactants, products and the catalyst are present in the same phase, in heterogeneous catalysis the reaction takes place near or at an interface between two phases. [1]

The first catalytic process known dates back to the very beginning of human civilization: the fermentation of carbohydrates, taken from plants, to produce ethyl alcohol. In these early times, however, catalysis was based on single observations without any efforts to study or explain the phenomena.

Only in 1835 Jöns Jacob Berzelius made an effort to classify the catalytic observations and study them systematically. Thanks to the subsequent growing knowledge about catalysis, new catalysts were found and catalytic processes could be introduced into industrial applications. [2] The processes based on catalytic systems allowed the tremendously fast development of modern society, especially in the second half of the 20th century. The connection of the development of modern society on the one hand, but the one of catalytic processes on the other hand, is based on the opportunities catalysis offers: Chemical molecules can be obtained fast and selectively, which is necessary for the production of big quantities of materials without an accumulation of many by-products. [3]

There are many examples of processes, where catalysts have to be applied in order to obtain the needed quantities of the desired product: The agricultural production can only meet the demands of today's population of the world by the application of fertilizers, which are obtained by catalytic processes. The introduction of fluid catalytic cracking, which sums up cracking, hydrodesulfurisation, isomerisation and alkylation of crude oil, was an important step to the motorization and aviation. These processes, at length, made the globalization possible. When the catalytic activity of transition metal oxides was discovered, catalysts of these components could be established for the production of base chemicals and monomers.

Even for most of the polymerization processes catalysts are used. Finally, without the synthetic fibers, which are derived from monomers as well, the world's demand of fibers could not be satisfied. Enzymes are another category of catalysts. They find application in biotechnology and can produce molecules regio- and stereoselectively.

A further more and more important field is catalysis for environmental control and protection. One aspect is to reduce the by-products already during the production, but another one is the need to destroy pollutants or undesired by-products. The three way catalyst for cleaning up the exhaust emitted by cars is one example of already applied techniques in these fields. The exhaust emitted by cars consists of not totally burnt hydrocarbons like aldehydes, ketones and CO as well as of nitrous gases. The three way catalyst has to oxidize the carbon containing substances to CO_2 and reduce the nitrous gases to N_2 at the same time.

Another current problem where catalysis plays an important role is the need for new sources of energy. Fuel cells have been lately discussed as a promising alternative, since they can convert chemical into electrical energy over an electrocatalyst at high efficiencies and low emissions of noxious compounds. Fuel cells make use of the overall reaction

$$2H_2 + O_2 \rightarrow 2H_2O \qquad (1)$$

In order to gain electrical energy the combustion of hydrogen is realized as two spatially separated reactions occurring at the surface of the electrocatalysts. The reaction at the anode can be formulated as

$$H_2 \rightarrow 2H^+ + 2e^- \qquad (2)$$

At the cathode oxygen is reduced by electrons and can react to water with protons that diffused from the anode to the cathode.

$$O_2 + 4H^+ + 4e^- \rightarrow 2H_2O \qquad (3)$$

The electrons produce the electrical energy, while they flow through an external circuit.

The realization of a sufficiently stable hydrogen supply is still one unsolved problem, as this gas is difficult and dangerous to store. One approach tries to use liquid fuels that are converted directly at the fuel cell to hydrogen which can immediately be used for the electrochemical reaction. This setting requires a highly active and selective catalytic system that is not only able to oxidize the fuel producing hydrogen, but also to perform the electrochemical reactions. A further demand is a low operating temperature, depending on the fuel cell system. [3]

One example of such a fuel cell system is the direct methanol fuel cell (DMFC). This type of fuel cells uses methanol as liquid fuel and has the advantage of an easy handling and processing, a potential fuel production from renewable resources, high energy conversion efficiency, low operating temperature and low pollutant emission. [4]

Furthermore, methanol is a potential carrier for automotive fuel. Decomposition (reaction 4) or steam reforming of methanol produces hydrogen, which can immediately be used as a fuel for the motor engine. Daimler Chrysler has already realized this idea in the NECAR (New Electric CAR) and is trying to advance this technology to market maturity. Preferential oxidation of the second decomposition product carbon monoxide leads to formation of carbon dioxide. [5]

$$H_3C{-}OH \longrightarrow CO + 2\ H_2 \qquad (4)$$

1.2 Methanol Oxidation

Methanol oxidation is not only interesting for the production of hydrogen, but can also be applied for the (selective) production of several other chemicals, depending on the catalyst used. In literature many different reaction products are reported to result from this reaction: formaldehyde (FA), dimethylether (DME), methyl formate (MFA), dimethoxymethane (DMM), CO_2 and CO. [6]

The oxidation of methanol (MeOH) to produce formaldehyde has gained industrial importance.

$$2\ H_3C{-}OH + O_2 \longrightarrow 2\ H_2C{=}O + 2\ H_2O \qquad (5)$$

$$H_3C{-}OH \longrightarrow H_2C{=}O + 2\ H_2 \qquad (6)$$

From an environmental point of view this reaction is advantageous, since it is a phase reaction; consequently there is no need for solvents. Moreover, by an optimization of the catalyst a high selectivity can be achieved, which is beneficial for the economic aspect as well. [7] FA is of great industrial importance, since it is one of the most important base chemicals and serves as a building unit in a variety of substances. Therefore the consumption of FA has grown steadily in the past two decades. [8] At present silver or ferric molybdate catalysts are in use in industrial processes. [7]

Methyl formate is another important chemical, which is in use as a solvent, an insect control agent and serves as a base chemical for other products. In addition to the conversion of MFA to industrially relevant products like formic acid, acetic acid, formamide and ethylene glycol, dimethyl carbonate can be obtained. Dimethyl carbonate is a valuable product, as it is an important solvent and has the potential to replace phosgene. [9-11]

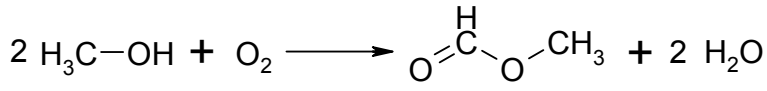

(7)

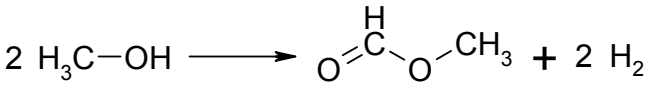

(8)

Dimethoxymethane is a solvent that is used in industrial processes due to its low toxicity. Recently researchers claimed that diesel / DMM blends lead to a reduction of particulate emissions and toxic gases. They found that the addition of ethers reduces smoke emissions more effectively than the addition of alcohols. [12-14]

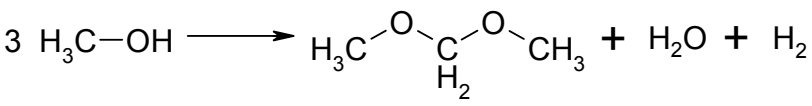

(9)

Further possible reactions of methanol with oxygen are the formation of carbon dioxide or carbon monoxide and water (reaction 10 – 11).

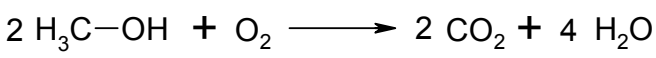

(10)

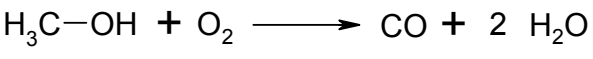

(11)

Another reaction is the dehydrogenation of methanol on acid sites to form dimethylether (reaction 12). This reaction can take place in absence of oxygen too.

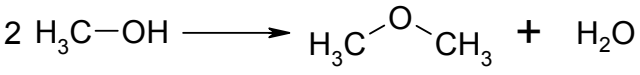

(12)

Finally, the methanol oxidation is used as a test reaction, because of the big diversity of products that can be obtained. Therefore, studying this reaction on a catalyst can give information about the active sites and functionalities of the catalyst. [6] The reaction is especially suitable for testing the performance of catalysts in exothermic reactions. As can be seen in table 1.1, the total oxidation to CO_2, for example, is highly exothermic and many of the other possible reactions have exothermic characteristics as well.

Table 1.1: Standard reaction enthalpies (ΔH_r° **)** for the possible gas phase reactions of methanol with oxygen. The standard formation enthalpies ΔH_f° of the molecules needed for the calculation of ΔH_r° were taken from literature [15].

Reaction	ΔH_r° [kJ/mol]
2 CH_3OH + O_2 → 2 CO_2 + 4 H_2O	-1352
2 CH_3OH + O_2 → $C_2H_4O_2$* + 2 H_2O	-439
2 CH_3OH → $C_2H_4O_2$* + 2 H_2O	45
2 CH_3OH → C_2H_6O** + 2 H_2O	-266
CH_3OH + O_2 → CO + 2 H_2O	-393
CH_3OH → CO + 2 H_2	91
2 CH_3OH + O_2 → 2 CH_2O♦♦ + 2 H_2O	-299
CH_3OH → CH_2O♦♦ + H_2	92
3 CH_3OH → $C_3H_8O_2$♦ + H_2O + H_2	13

*MFA, **DME, ♦DMM, ♦♦FA

1.3 Metal Oxide – Carbon Nanotube Hybrids: A New Class of Materials

Quite a lot of work has been done in the last time to obtain and stabilize smaller and smaller nanosized oxide particles. The small dimensions are advantageous for applications in reactions at the solid-gas or solid-liquid interface, because of the increasing specific surface area. [16] Although nanosized materials already show new characteristics compared to their bulk analogues, still not all demands for new technologies can be fulfilled. A new approach for the creation of materials with superior properties is the synthesis of organic-inorganic hybrids. They show new properties, different from their organic and inorganic building block. Therefore, the term inorganic-organic hybrids cannot be applied for nanocomposites, which just combine the individual properties of the two building blocks. Metal organic frameworks are already known to fulfill those requirements. [17, 18] A new class of inorganic-organic

hybrids uses carbon nanotubes (CNTs) as organic building block. In the final hybrid the inorganic compound coats the CNTs coaxially. CNTs seem to be an especially interesting type of organic building block due to their excellent mechanical, electrical and optical properties. Additionally, they have a high thermal conductivity and are supposed to stabilize inorganic moieties by acting as heat sink during calcination and activation treatments. CNTs as support of catalysts are expected to homogeneously distribute the heat in strongly exothermic reactions, reduce the heat peaks on the active sites and lead to better controllable conditions. In this way over-oxidation should be prevented and particle sintering reduced.

Latest research on CNT-inorganic hybrids has already shown promising results in different fields of application. In gas sensors, photovoltaics and photocatalysts they reduce the electron-hole recombination rate compared to bulk materials and they have already proven to improve intrinsic capacitors in supercapacitors and batteries. Charge transfer processes through the CNT-inorganic interface are believed to be the reason for these effects. [16]

There exist many routes to synthesize those hybrid materials. This allows certain tunability and compared to solid state reactions for the synthesis of inorganic materials the reaction temperatures are very low. The linkage between the organic and the inorganic component can be realized in two ways: via a strong covalent bond or via weaker interactions such as van der Waals forces, hydrogen bonding or weak electrostatic interactions. [17, 18]

Generally, the first step is the synthesis of the CNTs which are mainly synthesized by four techniques: arc discharge, laser ablation, molten salt intercalation and chemical vapor deposition. Metallic nickel is known to catalyze the growth of CNTs. Purification of the CNTs is another crucial step, since one has to pay attention not to damage or destroy the CNT's surface. Oxidizing techniques at lower temperature below 550 °C and annealing at higher temperatures in vacuum at 600 – 2000 °C are described in literature. [19-22]

In order to enable an interaction between the hydrophobic CNTs and hydrophilic inorganic compounds such as metal oxides, a functionalization of the CNTs is necessary. For a covalent functionalization an aggressive treatment with HNO_3/H_2SO_4 mixtures or plasma etching are common, creating carboxyl groups on the surface. [23] However, the covalent functionalization entails a change of the chemical properties of the CNTs in terms of their solubility and chemical reactivity. [24] Noncovalent functionalization is realized by van der Waals forces, hydrogen bonding or π-π interactions between aromatic compounds and the delocalized electron system of the CNTs. [25] One has to keep in mind the different reactivity of CNTs between the sidewall and the end-caps, due to the increased curvature causing a π-orbital mismatch. [26]

Although there are several ways to noncovalently attach nanoparticles to CNTs, all of them need linking agents – either functionalizing the nanotubes or the nanoparticles or both of them. Surfactants such as sodium dodecylsulfate which decorate the walls of CNTs and fix nanoparticles on the walls as well as hydrophobic capping agents which are functionalizing the inorganic nanoparticles have proven to be successful ways to provide a linkage between the CNTs and the inorganic compounds. [27, 28] Another possible route makes use of electrostatic interactions. In this case the CNTs are modified with ionic polyelectrolytes by deposition, allowing the creation of positively or negatively charged nanotubes, depending on the polyelectrolyte. Thus an attraction of charged nanoparticles is achieved. [29] Finally, there exists the possibility of a π-π stacking. Aromatics such as derivatives of pyrene, porphyrins, phthalocyanines or benzyl alcohol can interact with their aromatic π-system with the delocalized π-electrons of the CNTs. Modification of the aromatics with alkyl chains terminated with thiol, amine, acid or alcohol groups enables the connection to the inorganic nanoparticles (figure 1.1). [22, 30-32]

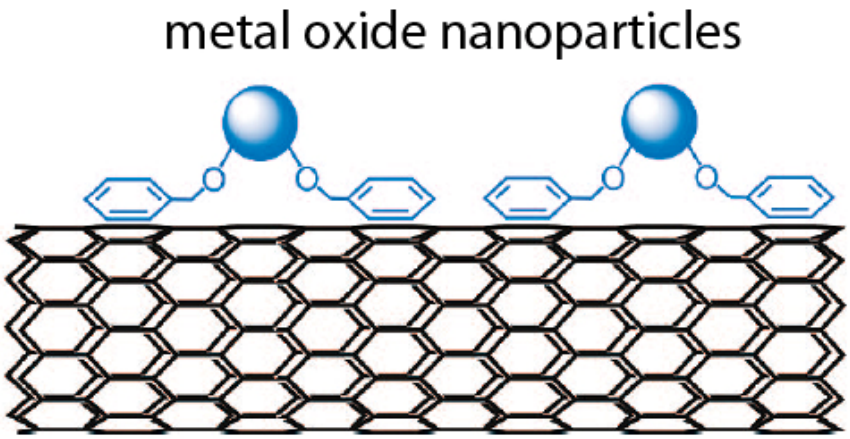

Figure 1.1: Schematic illustration of the linking agent benzyl alcohol used to attach metal oxide nanoparticles to the CNTs' surface via π-π interactions. Reprinted with permission from Eder, D.: Carbon Nanotube-Inorganic Hybrids. Chem. Rev., 2010, 110, pp.1348-1385. Copyright 2010 American Chemical Society.

Beside the opportunity to attach readily synthesized nanoparticles to the CNTs, it is possible to synthesize the nanoparticles directly on the CNTs. One approach makes use of the sol-gel process, which belongs to soft chemistry, because of its mild reaction conditions. In sol-gel processes metal oxide materials are obtained by progressive polycondensation reactions of molecular precursors in a liquid solvent. The first step is the formation of a sol, which is

defined as a "stable suspension of colloidal solid particles or polymers in a liquid".[1] Further aging of the sol leads to the formation of the gel, a porous, three—dimensional continuous solid network that is surrounded by a continuous liquid phase. This technique can be adapted to all metal oxides. Metal salts or metal alkoxides are common precursors which can easily undergo hydrolysis and condensation reactions, being the basis of the three-dimensional network. A final step includes a heat treatment under relatively mild conditions, in order to remove the organic groups from the gel. As this heat treatment is accompanied by the evaporation of the liquid phase, capillary forces transform the gel into a denser xerogel or even destroy the gel body completely, so that powders are obtained. A special drying treatment allows a minimization of shrinkage, so that an aerogel with the same structure as the gel after synthesis can be obtained. In any case, this method leads to amorphous structures. If crystalline products are needed, an annealing or crystallization treatment at higher temperatures is necessary. [33]

As already described above, linking molecules are needed to grow the inorganic component on the surface of the CNTs. Benzyl alcohol has been successfully applied in literature [22]. On the one hand, this molecule can adsorb via π-π interactions of its benzene ring to the CNTs' surface, and on the other hand, its hydrophilic hydroxyl group can initiate the hydrolysis of alkoxide groups of metal alkoxide precursors for a sol-gel process. This system is symbolized in figure 1.2.

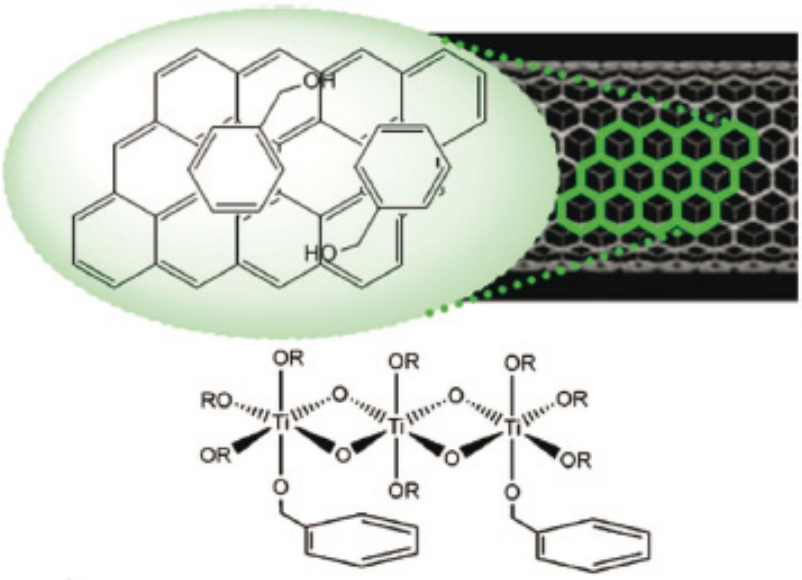

Figure 1.2: Schematic illustration of benzylalcohol attached to the CNT-surface and acting as initiator for the hydrolysis of titanium alkoxide precursors. Adapted with permission from Eder, D; Windle, A..: Carbon-inorganic hybrid materials: the carbon-nanotube/TiO2 interface. Adv. Mater., 2008, 20, pp.1787-1793. Copyright 2008 Wiley-VCH Verlag GmbH & Co.

[1] Schubert, U.; Hüsing, N.: Synthesis of Inorganic Materials. Wiley-VCH, Weinheim, 2012, p. 166.

2 Theoretical Background and Methodology

In heterogeneous catalysis the first step is the adsorption of the reacting gas to the catalyst. The adsorption comes along with a bond breaking or weakening of the adsorbed molecule, activating it for a further reaction. In the next steps, molecules adsorbed on the surface can undergo reactions on the surface before finally desorbing from it. Consequently, it is important to investigate the structure and surface of the catalyst in detail to identify the active sites and the way the catalyst works. In order to achieve a detailed characterisation of the catalyst different techniques need to be applied. While microscopic techniques are indispensable of a detailed surface analysis, spectroscopic techniques can reveal information about active sites and the interaction of the catalyst with the adsorbed molecules. Combination with reactivity tests allows establishing correlations between structure, surface sites and performance.

2.1 Transmission Electron Microscopy

Since modern research in the field of catalysis often focuses on nanoscaled and nanostructured materials, there is a need for microscopes resolving these dimensions. The smallest distance δ that can be resolved in the conventional visible-light microscopes is restricted according to the classical Rayleigh criterion for visible-light microscopes:

$$\delta = \frac{0.61 * \lambda}{\mu * \sin \beta} \qquad \text{equation 1}$$

λ: wavelength of the radiation [nm]

μ: refractive index of the viewing medium

β: semi-angle of collection of the magnifying lens

Consequently, good visible-light microscopes attain a resolution of ~300 nm.

The demand of a nanoscale-resolution can be met by transmission electron microscopy (TEM), whose best resolution can be approximated by the following expression:

$$\delta = \frac{1.22 * \lambda}{\beta} \qquad \text{equation 2}$$

Considering Louis de Broglie's equation relating the electrons' energy E with their wavelength (when neglecting relativistic effects)

$$\lambda = \frac{1.22}{\sqrt{E}}$$ equation 3

E: energy [eV]

λ: wavelength [nm]

and the fact that electrons in the transmission electron microscope (TEM) are accelerated to ~100 keV, one can estimate λ of the electrons to ~4 pm. In fact, the resolution of TEMs is not limited by wavelength, but by the difficulty of the construction of perfect electron lenses. [34, 35]

The principle of conventional TEM is the irradiation of a thin specimen with an electron beam and the detection of those electrons that have been transmitted through the specimen. Electrons as an ionizing radiation interact with matter and produce different kinds of secondary signals, which are characteristic of the specimen (figure 2.1). The term 'transmitted', actually, means scattered in the forward direction in the TEM. However, modern devices often have additional detectors, offering the possibility to analyze backscattered signals as well. Many of the secondary signals are used for analytical electron microscopy as for example X-ray energy-dispersive spectrometry (EDX) or electron energy-loss spectrometry (EELS). [34]

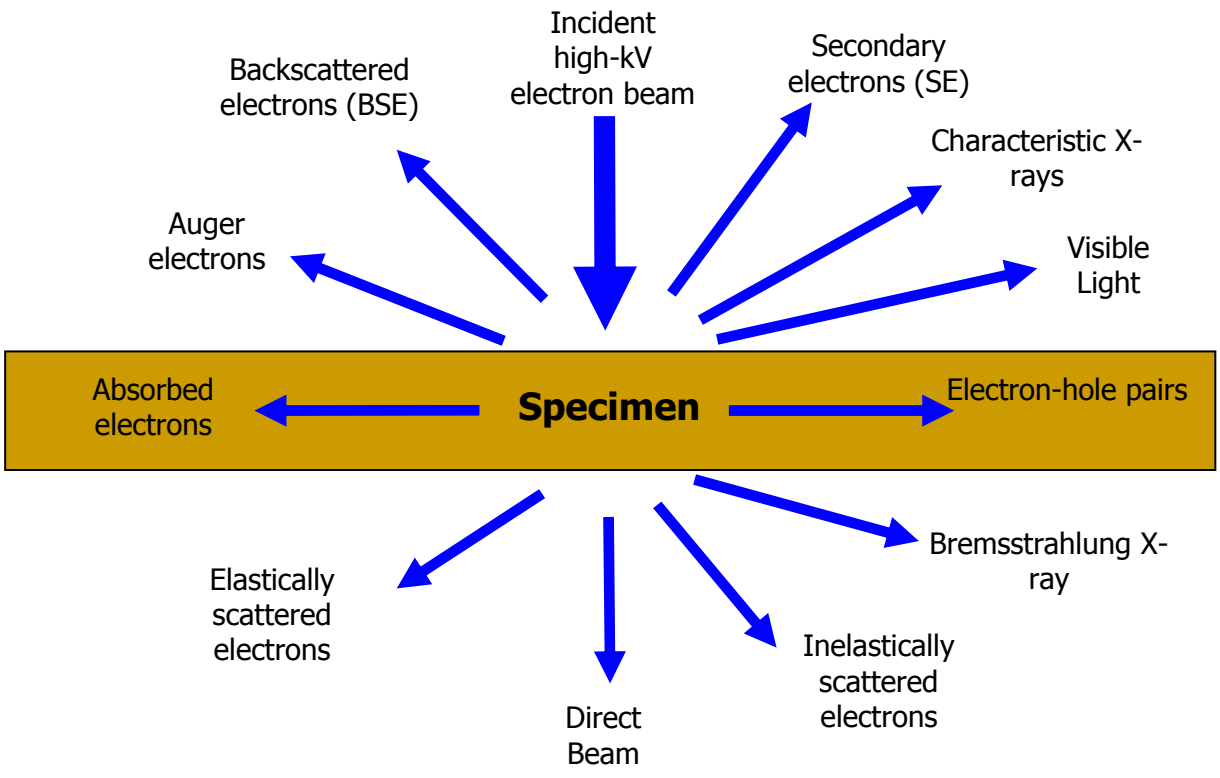

Figure 2.1: Secondary signals that can be detected after the interaction of a highly energetic electron beam with the sample.

2.1.1 Essential Components of the TEM

The most important components of TEMs are symbolized in figure 2.2.

The upper part of the electron microscope is called electron gun, which consists of the electron source and an electrode system which extracts the electrons, focuses them to a beam and directs the beam into the illumination system. The electrode system differs depending on the electron source that can be either a thermionic source (LaB_6-crystal) or a field-emission source (tungsten). While for thermionic sources Wehnelt electrodes are necessary, field-emission sources can be operated with simpler systems. The field-emission tip can be directly applied as cathode with respect to two other anodes. Field-emission guns form more monochromatic and better focused electron beams. In both cases a high voltage supply is indispensable.

Going down from the top to the bottom in the schematic from figure 2.2, the next part of the TEM is a system of lenses (condenser lenses and objective lenses) and apertures or rather diaphragms, which focus the electron beam to a spot or an almost plane-parallel illumination of a larger area.

The specimen holder, which must be inserted into the TEM stage through an airlock in order not to break the ultrahigh vacuum in the TEM, has to be located invariably within the objective lens. Furthermore, it is responsible for the moving or tilting of the specimen, which is necessary to study the specimen at different orientations and positions.

Finally, projector lenses transfer the image or diffraction pattern to a viewing screen, coated with a material that emits light after contact with electrons. Charge-Coupled-Device (CCD) Detectors are commonly used for the registration of the images or diffraction patterns.

The whole transmission electron microscope must be kept under ultrahigh vacuum, because of the strong scattering of the electrons by atoms or gas molecules. The ultrahigh vacuum is realized by a set of different vacuum pumps, to create a rough vacuum in a first step with roughing pumps and a high or ultrahigh vacuum in a second step with diffusion pumps, turbomolecular pumps, ion pumps or cryogenic adsorption pumps. [34]

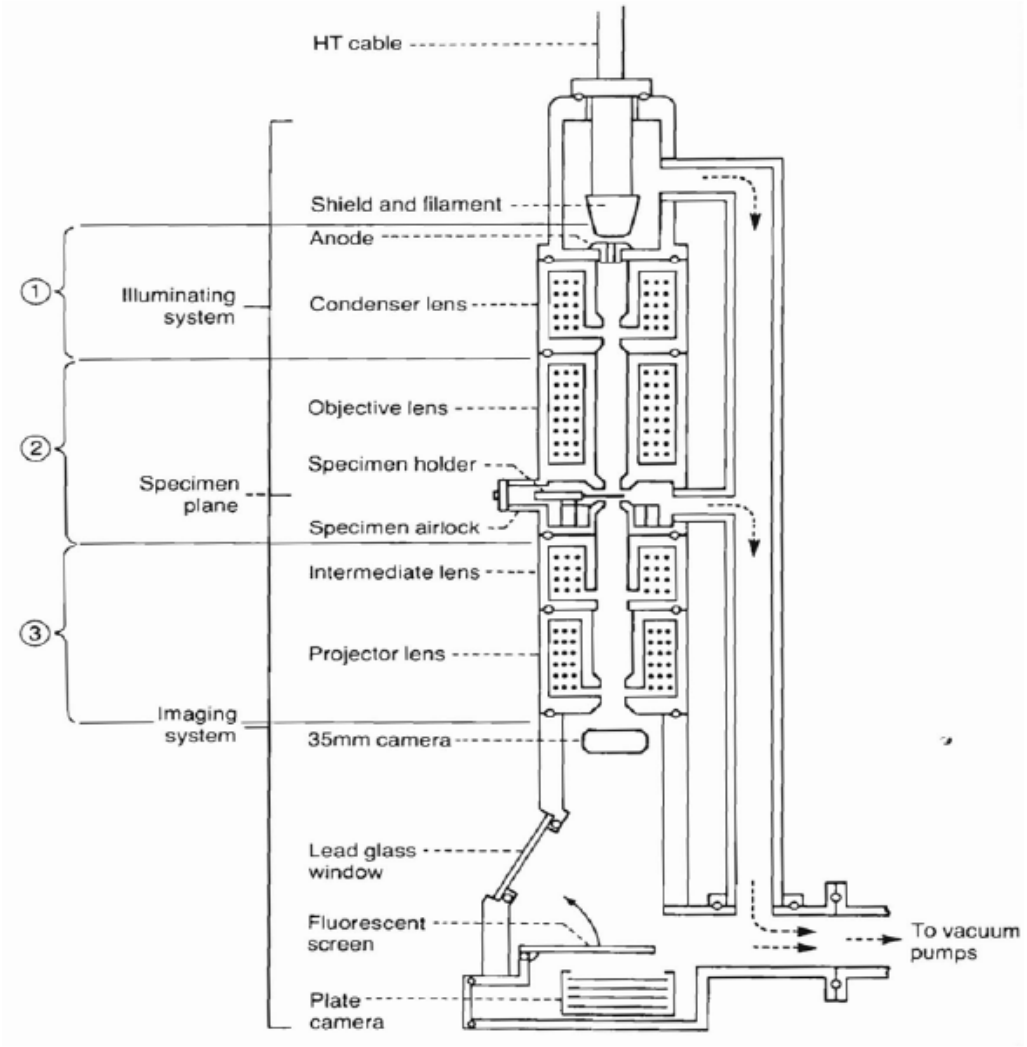

Figure 2.2: Schematic of a transmission electron microscope. Reprinted with permission from Hunter, E. E.: Practical Electron Microscopy: A Beginners Illustrated Guide. Cambridge University Press, 1993, p.106, figure 6.3. Copyright 1993 Cambridge University Press. [36]

Concerning the resolution in TEM the main limiting factor is the fact that real electromagnetic lenses cannot be constructed perfectly. Three resulting main lens defects are spherical aberration (C_s), chromatic aberration (C_c) and astigmatism. Modern techniques to compensate for these defects have entailed a big step forward in the resolution. These new techniques allow, for instance, the resolution of lattice frames of crystalline materials; TEM at these high resolutions is called High Resolution Transmission Electron Microscopy (HRTEM). The three defects and the ways to compensate for them are described in the following:

- When the lens field for off-axis rays behaves differently, electrons, which are further off-axis, are more strongly bent back towards the axis. As a consequence, point objects are imaged as disks of finite size, which is the reason, why this defect is called spherical aberration. Spherical aberration plays the most important role in the

objective lens, because all other lenses magnify the degradation of the resolution. Modern microscopes try to compensate for this defect by re-directing the off-axis beams in such ways that the whole beam re-converges to a point rather than a disk in the image plane. Practically, this is realized by a highly complex, computer-controlled set of quadrupoles and hexapoles or octupoles.

- The chromatic aberration, which is also observed in visible-light microscopes, arises from the different colors of visible light. Actually, this effect is related to the different wavelengths, energies or frequencies of the radiation being responsible for the image. Therefore, this phenomenon has to be considered for electrons as well. Nevertheless, depending on the electron source the energy distribution of the beam varies only marginally (~0.3 eV for a cold Field Emission Gun and ~1 eV for a LaB_6 source). In most cases the defect resulting from the C_c of the electron source is not resolution-limiting. However, when the electrons interact with the specimen, they undergo several scattering processes as described above. The thicker the sample is, the stronger the resulting chromatic aberration is and the stronger it impairs the resolution. If it is not possible to use thinner samples, energy-filtering seems to be the best solution.
- Astigmatism is the deflection of the electrons from the optical axis due to non-uniform magnetic fields. The reason of this non-uniformity can be microstructural inhomogeneities of the soft-iron pole pieces, not precisely centered apertures or not-clean apertures. The astigmatism can be corrected via stigmators, small octupoles that establish a compensating field. [34]

2.1.2 Imaging in TEM and Scanning Transmission Electron Microscopy (STEM)

While in the conventional TEM a bigger area of the specimen is illuminated, a part of the electrons emerging from this area is selected via apertures and displayed on the viewing screen, in STEM the electron beam is focused to a small spot that is scanned across the specimen. In the TEM-mode the magnified image on the viewing screen is obtained by an objective lens system situated underneath the specimen. On the contrary, the STEM-mode does not use lenses to form the image. The electron beam is scanned across the sample with the help of scan coils that are scanning the computer display synchronously. This arrangement is indispensable, since the beam must scan parallel to the optical axis at all time. Between specimen and display screen only an electron detector serves as interlink.

Consequently, STEM has the advantage not to be limited by lens defects. This is especially crucial for thicker samples, where chromatic aberration can seriously limit TEM image resolution. Furthermore, the illumination of just one spot of the specimen offers the possibility of microanalysis. One disadvantage of STEM is the time factor, since it is recording serially in contrast to TEM-imaging. [34]

2.1.3 Image Contrast in TEM

Contrast in TEM-images stems from the scattering of the incident electron beam by the specimen. Speaking about the electrons as waves, they can change their amplitude as well as their phase because of the scattering. Both events result in an image contrast, for which reason they are named amplitude contrast and phase contrast. Usually, both types contribute to the image at the same time.

Amplitude contrast comprises two main types of contrast forming: mass-thickness contrast and diffraction contrast.

Mass-thickness contrast is correlated to the incoherent elastic scattering (Rutherford scattering) of electrons, which in turn is a function of the atomic number Z on the one hand, but of the thickness of the specimen on the other hand. The higher Z is, the more the electrons are scattered, because of the bigger cross section of the atoms. Considering the thickness of the specimen, the thicker it is, the more electrons are scattered, since the mean free path remains fixed. In the end, the more electrons at one position are scattered, the lower the intensity of this position is.

While the mass-thickness contrast is most important for amorphous and non-crystalline materials, the diffraction contrast arises from the diffraction of the electron waves in a crystalline material, in other words from the coherent elastic scattering.

The phase contrast mechanism is very sensitive to many factors and can therefore be difficult to interpret. For instance, only small variations in the thickness, orientation or scattering factor of the specimen can cause phase contrast. However, variations in the astigmatism or focus of the objective lens can affect the phases as well. [34]

In any case, one has to be careful with the interpretation of TEM images, since they present 3D specimens in two dimensions.

2.2 Infrared Spectroscopy

The energy of molecules can be divided into translational, rotational, vibrational and electronic energy. For a first approximation it is valid to consider these energy contributions separately. [37] As it is known from quantum mechanics, every molecule possesses specific, discrete vibrational and rotational energy levels. Assuming that the atoms of the molecule are very near to their equilibrium position during the vibration, the potential energy can be very roughly approximated by a harmonic oscillator. This approximation results in equidistant energy levels with an energy difference that is depending on the mass of the molecule's atoms and the strength of the bond (equation 3).

$$\nu = \frac{1}{2\pi}\sqrt{\frac{k}{\mu}} \qquad \text{equation 4}$$

$$\mu = \frac{m_1 * m_2}{m_1 + m_2} \qquad \text{equation 5}$$

v: frequency of the vibration

k: force constant of the bond

μ: reduced mass

m_i: mass of the vibrating atoms

For a more accurate calculation a morse potential has to be used, which is physically more realistic.

As the energy distance between two vibrational levels is in the infrared range of the electromagnetic spectrum, a photon of the appropriate energy can be absorbed by the molecule. This absorption causes a transition of the molecule to a higher vibrational state.

According to quantum mechanics there exists a set of selection rules defining the allowed transitions. One general requirement for the absorption of a photon is the change of the dipole moment of the molecule during the vibration.

Possible vibrations of a molecule are classified in several types:

- Stretching vibrations (v) – are defined as the changing of the length of a bond (figure 2.3 a).
- Deformation vibrations – can be further categorized into two types:

- Bending vibrations in one plane (δ) – describe all vibrations that alter the angles in one plane, but leave the bond lengths unaltered. Examples of these vibrations are twisting, wagging, rocking and scissoring (figure 2.3 b).
- Bending vibrations out of plane (γ) – can be characterized by one atom oscillating through a plane described by three or more neighbouring atoms (figure 2.3 c).

- Torsional vibrations (τ) – describe the changing of the angle between two planes defined by atoms of the molecule (figure 2.3 d). [38]

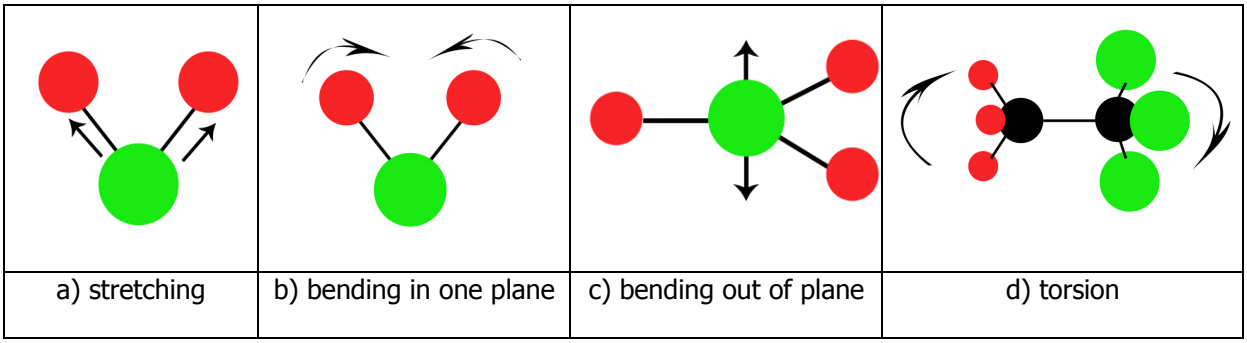

a) stretching	b) bending in one plane	c) bending out of plane	d) torsion

Figure 2.3: Visualization of the vibration types: a) symmetric stretching vibration, exemplified by a water molecule, b) scissoring as a form of the deformation vibration, exemplified by a water molecule, c) bending vibration out of plane, exemplified by a BF_3 molecule, d) torsional vibration, exemplified by a $C_2H_3Cl_3$ molecule.

Many vibrational modes are further divided into symmetrical and asymmetrical vibrations (usually marked by the subscribt 's' respectively 'as' behind the symbol of the vibration mode). Selection rules and tables showing which vibrations are allowed for which molecules can be found in literature [37, 39].

For the study of adsorbed gas molecules on a catalyst two techniques are commonly used.

The most direct technique is the transmission infrared spectroscopy. In this case the powdered catalyst sample is pressed into a self supporting thin disk. The thickness depends on the sample; however, the disk must remain transparent for the IR beam. If the sample is absorbing strongly in the mid-infrared range, it can be diluted with commercial powders like KBr, which only shows a cut-off at wavenumbers <400 cm^{-1}.

A second technique is the diffuse reflectance infrared Fourier transform spectroscopy (DRIFTS). In this method the IR beam is directed on the loose sample powder and the diffusely scattered radiation is collected by mirrors and focused on the detector. Via the Kubelka-Munk function the measured spectrum can be transformed into a spectrum

proportional to an absorption spectrum. This technique is especially advantageous for strongly scattering or absorbing particles, which are hard to measure by transmission IR spectroscopy. [38, 40]

The spectra of adsorbed molecules can provide lots of information about the available adsorption sites on the catalyst surface and the chemical environment. Carbon monoxide as a test molecule can be easily studied in vibrational spectroscopy, because of its strong dipole moment. Furthermore, the C-O stretch vibration frequencies appear in a spectral range, where hardly any other vibrations are overlapping. From the exact position of the absorption band of the CO molecule in the spectrum its adsorption configuration can be determined: The C-O stretching band of the gas molecule is at 2143 cm^{-1}. CO adsorbed on a metal surface in an on-top position can be found at frequencies between 2130 and 2000 cm^{-1}. Bridge bonded CO absorbs in the region of 2000 – 1880 cm^{-1} and threefold-hollow bonded CO from 1880 to 1800 cm^{-1}. [38] The shift of the vibration is explained by the backbonding of the substrate into the antibonding π*-orbitals of the CO molecule, which weakens the C-O bond. Therefore the stronger the molecule is bound to the surface, the stronger the shift is to lower wavenumbers. In figure 2.4 the possible adsorption sites are symbolized.

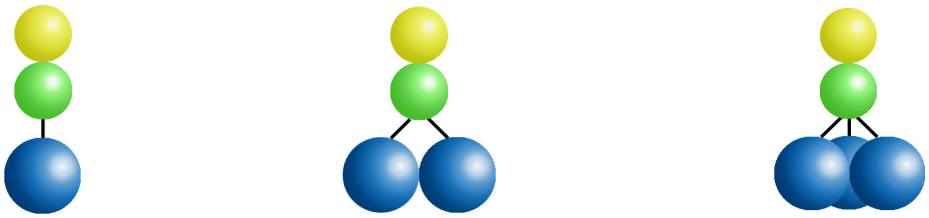

a) CO in on-top position b) CO in bridge position c) CO in three-fold-hollow position

Figure 2.4: Possible adsorption sites of the CO molecule on a surface.

The described redshift is characteristic of metals; for metal oxides in most cases a blueshift can be observed. The reason for this shift to higher frequencies is the bonding of the free electron lone pair at the carbon atom of the CO molecule to free d-orbitals of the metal oxide. Since the lone pair of the carbon atom has a partly antibonding character, the internal C-O bonding is strengthened this way. If many of the d-orbitals of the metal oxide are occupied, additionally, a back bonding to the antibonding π*-orbitals of the CO molecule is possible. Although the backbonding entails a redshift of the C-O stretch frequency, the sum of the two phenomena results in a blueshift for most metal oxides.

2.3 Temperature Programmed Techniques

There exists a range of different temperature programmed techniques: Temperature Programmed Reduction (TPR), Temperature Programmed Oxidation (TPO), Temperature Programmed Desorption (TPD) and Temperature Programmed Reaction (TPReaction). All these techniques have in common that chemical processes are observed while the temperature is increased linearly in time. Their instrumental realization is not expensive compared to other spectroscopic techniques; the experimental performance is simple and possible for both real catalysts and single crystals. Getting qualitative information is pretty straightforward. One drawback is the difficulty in obtaining reaction parameters. For calculating activation energies of reduction from TPR, for example, single, well defined processes are demanded. This requires in turn the same morphology of all particles and the same interaction with the chemical environment of every atom. Otherwise TPR patterns would represent only combinations of different reduction processes. These requirements are especially difficult to achieve in supported catalyst systems. Deriving desorption energies from TPD spectra is also complex, since they depend on the coverage of the surface and have to be separately determined for every coverage. Nevertheless, simplifications are commonly used and can be found in literature.

The instrumental realization for investigation of powder samples is based on a plug-flow-reactor in an oven which is capable of raising the temperature linearly in time at a defined rate and a detection system. The detector can be realized as a thermal conductivity detector (TCD) or a mass spectrometer (MS).

In case of the TPR and TPO hydrogen respectively oxygen diluted by an inert gas are flown over the pre-oxidized or pre-reduced sample. Reduction or oxidation processes at certain temperatures result in a change of the composition of the carrier gas and in a signal at the detector (usually a TCD). The obtained signal gives information about the hydrogen or oxygen consumption of the sample with temperature.

For TPReaction and TPD a mass spectrometer is indispensable, because MS allows differentiating the complex processes that can occur (desorption, decomposition, reaction with catalyst surface). [38]

2.4 Detection Systems for Reactivity Tests

As the proper detection system is very important for obtaining good results in reactivity tests, a very brief overview of the theoretical background of some detectors used in this work is given in the following.

2.4.1 Mass Spectrometry

Mass spectrometry is a method where molecules are ionized and subsequently separated according to their mass-to-charge ratio (m/z) before being detected. The whole spectrometer has to be kept under high vacuum in order to obtain (only) stable analyte ions that can be focussed on the separating system.

A widely used ionization method is the electron impact. Electrons are emitted from a tungsten or rhenium thermionic cathode and accelerated to the anode by a voltage of 70 – 100 V. On the way to the anode the electrons collide with the gas molecules ionizing them. The mainly formed cation radicals are directed and focussed via an electrical field according to their charge on the entrance slit of the mass separation system. [41]

The quadrupole mass analyzer is – maybe due to its price and compactness – one of the most common mass filters. It consists of 4 metal rods (symbolized in figure 2.5), which are connected to a variable direct current source in a way that the opposite pairs are equally polarized. In addition to the direct current field, alternating radio frequency potentials are applied, so that only ions of a specific m/z ratio will have a stable trajectory and will pass through the detector. By changing the radio frequency various ions with different m/z ratios can be selected, forming the spectrum in the end.

The correlation of the m/z ratio and the quadrupole field can be easily calculated after some simplifications [41, 42]:

$$\frac{m}{z} = \frac{5.7 * V}{\omega^2 * r^2} \qquad \text{equation 6}$$

V: alternating voltage

r: quadrupole radius

ω: angular frequency

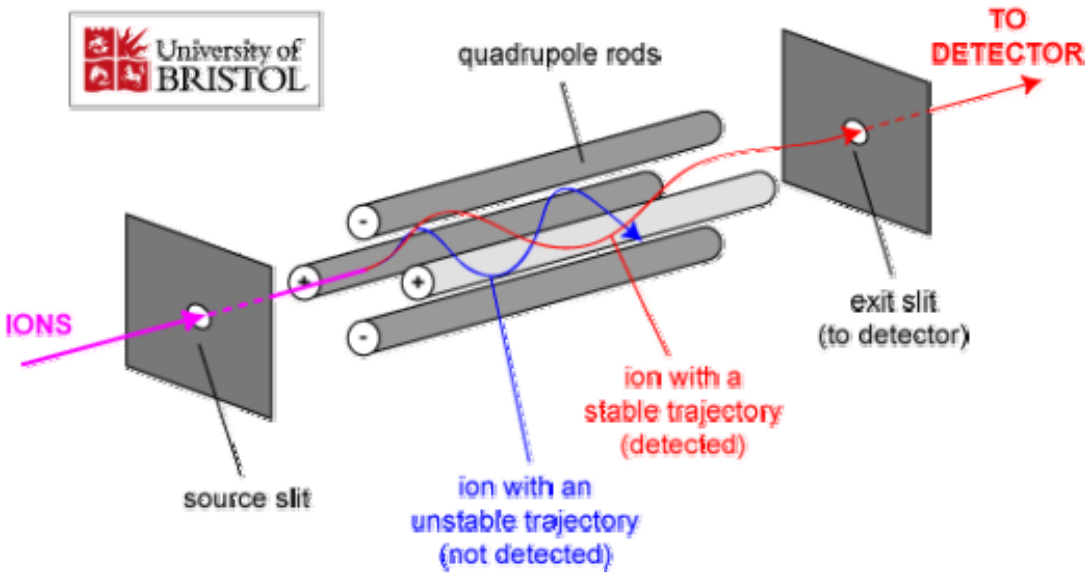

Figure 2.5: Schematic of a seperator based on quadrupoles. Taken from literature [42]

For the detection of the separated ions two systems are common. A Faraday cup is the simpler variant of these two. Therefore it is cheaper, nevertheless, has long life time, high measurement accuracy and good reproducibility. Usually ion currents $>10^{-15}$ A can be detected. The Faraday cup consists of a metal cup that has one small entrance slit on one side. The ions are caught by the cup and when touching the metal surface, the positive ions are neutralized by electrons. This causes a discharging of the metal resulting in an electrical current that can be measured. The current is proportional to the number of ions being caught by the cup.

A second type of widely used detectors is the electron multiplier whose principle is used in several subtypes. The advantage is a lower limit of detection (for a Secondary Electron Multiplier (SEM) 10^{-17} – 10^{-18} A); however, SEMs suffer from a shorter life time and higher costs. Electron multipliers are based on the effect of the generation of 2 – 3 electrons when a single electron hits an emissive material in vacuum. The emissive material is realized as an electrode, called dynode. In case of a SEM several dynodes are arranged consecutively. The application of an electrical field directs the electrons from one dynode to the next so that an avalanche of electrons emerges. A Channel Electron Multiplier on the contrary consists of a continuously working dynode, which has the form of a juvenescent horn. The created and extensively multiplied electrons are detected at a collector electrode. [41, 43-45]

2.4.2 Gas Chromatography

Gas chromatography is a chromatographic method, whose mobile phase is a gas. The gas chromatograph consists of an injector, the separating column and the detection system. The injection system has to guarantee that a representative part of the sample is transferred to the column without altering the chemical composition of the analytes. The column, which can be realized as a packed or a capillary column, is responsible for the separation of the analytes in the sample. Each substance undergoes a different interaction with the stationary phase of the column, resulting in different retention times. For a proper and as fast as possible separation of the analytes in the sample, it is necessary to optimize one or more parameters of the system: the stationary phase, the flow of the mobile phase or the temperature program of the column. [41]

As detection system the combination of a thermal conductivity detector (TCD) and a Flame Ionization Detector (FID) is most commonly used, since they both operate over a wide range of concentrations and are sensitive to a wide range of substances. The TCD which works non-destructively is based on the different thermal conductivities of gases. The detection is realized by an electrically heated filament which is kept in a temperature-controlled cell. While only the carrier gas is flowing through the cell, the temperature of the filament is stable. When an analyte elutes from the column the thermal conductivity of the gas phase (usually) decreases, heats up the filament and changes the resistance. The thermal conductivity of the measurement cell is constantly compared to the one in a reference cell flowed through with carrier gas only. Classically the transformation to an analyzable signal is based on a Wheatstone bridge circuit, which produces a measurable voltage change. [46]

FIDs belong to the destructively working detectors and are sensitive to hydrocarbons. The eluent from the column is burnt in a hydrogen-air-flame, which first reduces the hydrocarbons to methane and oxidizes them in the oxygen-rich part of the flame via the formation of radicals to ions. The positive ions are collected by a voltage of several 100 V on a negatively charged electrode so that a current that is proportional to the amount of formed ions can be measured. [41]

In all cases after a calibration for each substance the peak area of the chromatograms can be used to obtain quantitative information of the sample composition.

For more detailed information books dealing with analytical chemistry can be consulted.

3 Experimental

3.1 Sample Preparation

In this thesis materials based on two different metal oxides – V_2O_5 and Bi_2O_3 – were investigated. Usually metal oxide catalysts are only active at elevated temperatures in many gas phase reactions. However, the CNT-inorganic hybrid materials to be tested are only stable up to ~300 °C. Preliminary tests on bulk V_2O_5 and bulk Bi_2O_3 assured that adequate temperatures for testing the materials in methanol oxidation would be too high for the hybrid materials. For these reasons palladium, which is known to lower temperatures at which a catalyst is active, was added to the catalyst systems by impregnation. Beside the CNT – inorganic hybrid materials, the respective bulk oxides were prepared which served as reference materials.

3.1.1 Preparation of the Reference Samples

An impregnation treatment was performed to obtain finely dispersed Pd nanoparticles on the metal oxide surface. Therefore the bulk metal oxide powders V_2O_5 (Pluratronic, 99,99%, CAS # 1314-62-1) or Bi_2O_3 (purum, >98%, CAS # 1304-76-3) were suspended in toluene by stirring. A calculated amount of palladium acetate to obtain samples with 2 wt% of Pd was dissolved in toluene at elevated temperatures and added to the suspension of the metal oxide. The solvent was evaporated at elevated temperatures under stirring. Finally, the samples were calcined at 250 °C for four hours.

3.1.2 Preparation of the Oxide - CNT Hybrid Materials

The metal oxide – CNT hybrids were prepared by a cooperation partner from the Westfälische Wilhelms-Universität Münster (group of Dominik Eder).

The CNTs were prepared by a CVD-process. Toluene served as a carbon source and 4 wt% of ferrocene were used as catalyst. Both carbon source and catalyst were injected together into the furnace reactor at 180 °C in an argon stream. The reaction took place in a quartz tube at 760 °C for 5 hours. After the synthesis the carbon nanotubes were heat treated in argon atmosphere at 1000 °C for 6 hours.

The subsequent synthesis of the hybrids was done by a sol-gel process. The CNTs were suspended in ethanol with the help of ultrasonication. For one V_2O_5-hybrid sample benzyl alcohol, which should serve as a linker, was added dropwise to the suspension. For all other

Bi_2O_3 or V_2O_5-hybrid samples no linker at all was used. The sample for which the linker was used in the synthesis was only characterized by TEM in this work.

The alkoxide precursors of the metal oxides – tri-tert-butyl orthovanadate ($VO(OC_3H_9)_3$) for the vanadium oxide hybrid samples and bismuth 2-ethyl hexanoate ($Bi(O_2C_8H_{15})_3$) for the bismuth oxide hybrid samples – were diluted with absolute ethanol and added drop by drop to the suspension of CNTs. After aging of the reaction mixture for 72 hours, an autoclavation treatment was performed at different temperatures ranging from 120 – 180 °C for 48 hours. The obtained samples were filtered and washed with ethanol. In order to obtain a crystalline coating the samples had to be calcined. The V_2O_5 – CNT – hybrids were calcined at 330 °C, the Bi_2O_3 – CNT – hybrids only at 270 °C. Higher calcination temperatures would have entailed combustion of the CNTs, which can be oxidized by a Mars van Krevelen mechanism. [47]

The obtained hybrid materials were further impregnated with 2 wt% palladium in the same way as the reference bulk metal oxides, as described in 3.1.1.

The prepared samples with their designation and synthetic properties are listed in table 2.1.

Table 3.1: Sample designations and their contents.

sample name	**content**		
	organic compound	**metal oxide**	**metal**
Pd-V_2O_5	-	V_2O_5	2 wt% Pd*
Pd-Bi_2O_3	-	Bi_2O_3	2 wt% Pd*
V_2O_5-CNT	CNT	V_2O_5	-
Bi_2O_3-CNT	CNT	Bi_2O_3	-
Pd-V_2O_5-CNT	CNT	V_2O_5	2 wt% Pd*
Pd-Bi_2O_3-CNT	CNT	Bi_2O_3	2 wt% Pd*
Pd-CNT	CNT		2 wt% Pd*

*percentage refers to the sample mass without Pd

In order to obtain a well-defined state of the catalyst for further kinetic or adsorption studies the catalysts were pretreated directly before every analysis either in oxidizing or in reducing conditions, which will be abbreviated as ox. for an oxidizing pretreatment and red. for a reducing pretreatment.

3.2 Transmission Electron Microscopy

Transmission electron microscopy was performed at the USTEM (Universitäre Service-Einrichtung für Transmissionselektronenmikroskopie) on a FEI TECNAI F20 transmission electron microscope. This microscope has a field emission gun as an electron source and the operation voltage can be varied from 60 kV to 200 kV. It is equipped with an EDX detector, can be switched to STEM mode and offers the possibility to use EELS (electron energy loss spectroscopy) and EFTEM (energy filtered TEM). High resolution TEM (HRTEM) can be performed with this microscope, since a lattice resolution of 0.14 nm and a point resolution of 0.21 nm can be attained.

For the measurements a copper grid was dipped into the powdered samples. Adhesive forces allowed small particles to stick to the copper grid; so the grid was fixed on the sample holder, which was introduced into the microscope. The voluminous partially agglomerated CNT samples had to be crushed with a bristle brush to smaller parts prior to dipping the grid into the samples. The reference metal oxide samples were reduced at 250 °C for 30 min ex-situ before they were introduced into the microscope. All measurements were performed in the brightfield mode. Due to the Z-contrast and the shape of the particles the different species were identified. Only for the reference Pd-Bi_2O_3 STEM measurements were performed because of the low Z-contrast difference between Bi_2O_3 and Pd preventing an analysis in the brightfield TEM mode. In this case EDX was applied to get information about the composition of the particles.

3.3 TPReaction

3.3.1 Reactor Setup

The setup for the TPReaction measurements is displayed in scheme 3.1. The sample was fixed in a quartz tube with an outer diameter of 6 mm with the help of quartz wool plugs, resulting in a fixed bed reactor. The temperature was measured with a thermocouple type K, consisting of a chromel-alumel combination, which is placed inside the quartz glass reactor via a septum so that the tip of the thermocouple was situated a few centimeters above the catalyst bed. The electrical oven was regulated by an Eurotherm controller connected to the thermocouple. The detection was realized by a mass spectrometer, Prisma Plus QMG 220 equipped with a Faraday detector and a HiCube 80 Eco turbo pumping station (Pfeiffer Vacuum). Gas flows were controlled by mass flow controllers (MKS, type 1179A Mass-Flo® Controller) or rotameters.

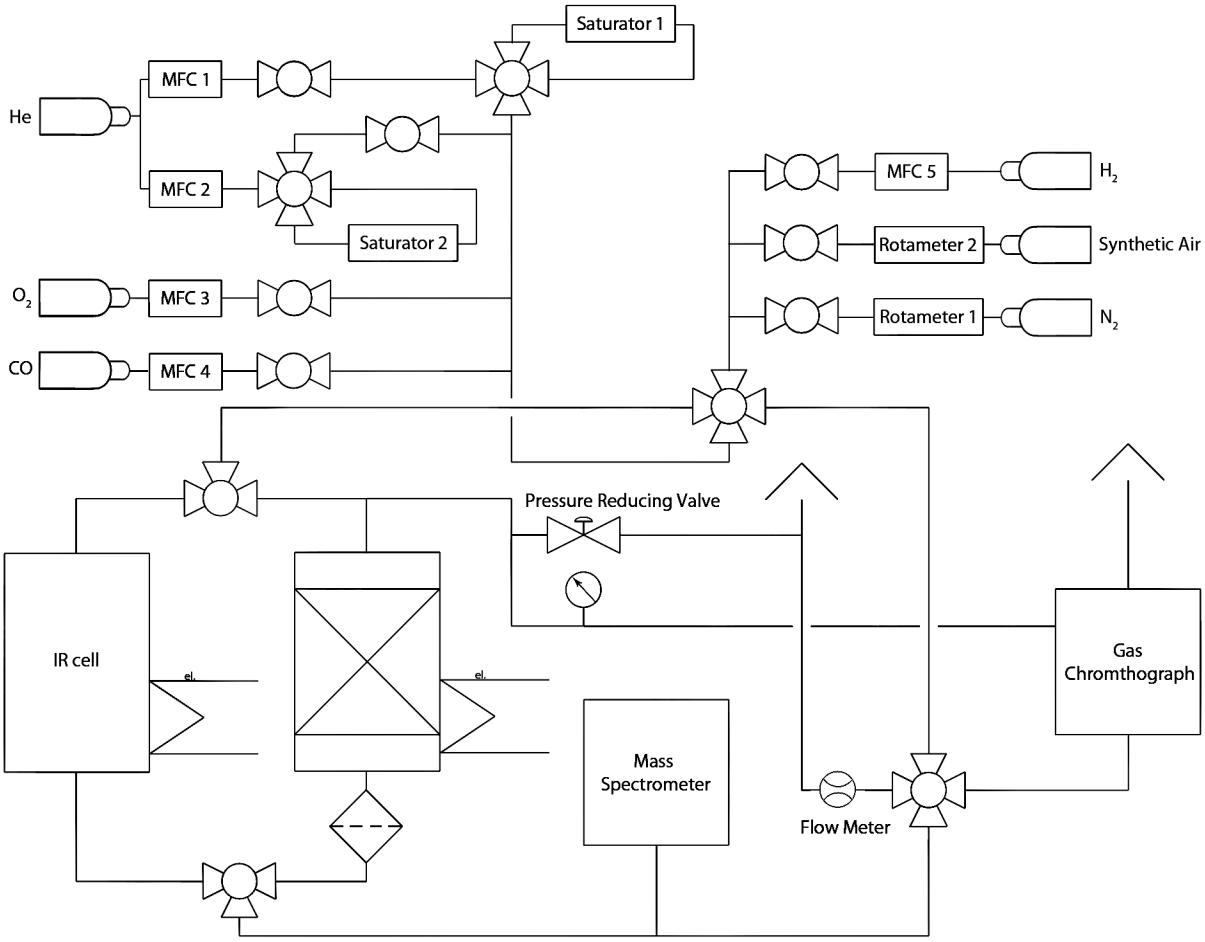

Scheme 3.1: Experimental setup for the kinetic and TPR measurements.

3.3.2 Sample Pretreatment and Reaction Conditions

If not stated differently, for all measurements 50 mg of the sample were first pretreated under oxidizing or reducing conditions at 250 °C for 30 min. As an oxidizing agent synthetic air was used, for the reducing pretreatment a mixture of ~20 % H_2 in N_2 was employed. A total flow of 70 ml/min was chosen for the pretreatment. After the pretreatment the samples were cooled to room temperature in the pretreatment gas flow. At room temperature the gas flow was switched to the reaction gas mixture, which consisted of 2 % methanol and 2 % O_2 in He at a total flow of 50 ml/min. The methanol flow was realized by a saturator kept at 0 °C (saturation vapor pressure at 0 °C for methanol: 39.95 mbar). When a stable reaction gas flow over the catalyst was detected, a temperature ramp of 2 °C/min to a final temperature of 250 °C for the CNT samples and to 300 °C for the reference metal oxide samples was applied, while the composition of the outlet gas flow was recorded by the mass spectrometer.

3.4 Infrared Spectroscopy

3.4.1 FTIR Spectrometer and Experimental Setup

Infrared measurements were performed on a Vertex 70 infrared spectrometer from Bruker Optics. A globar was installed in the spectrometer as an infrared radiation source and a HeNe laser as the internal wavelength standard. The detection was realized by a liquid nitrogen cooled mercury cadmium telluride detector (MCT-detector). The spectrometer was equipped with two sample chambers – a vacuum cell and a flow cell. Since the measurement cells are designed for transmission measurements, the samples had to be pressed to thin disks of a diameter of ~1 cm, which were inserted in the sample holder. The sample holder in the vacuum cell could be cooled by flowing liquid nitrogen through a cooling loop and heated by an electrical heating; the sample holder of the flow cell could only be heated. The temperature was measured with a type K thermocouple fixed at the edges around the sample holder. It was connected to a Eurotherm controller, which was reading out the temperature and controlling the electrical heating. The measurable temperatures ranged from 158 K to 773 K. The flow cell was connected to the apparatus used for TPReaction and kinetic measurements (as shown in scheme 3.1). The vacuum cell was connected to a turbomolecular pump (HiCube, Pfeiffer Vacuum) with a base pressure in the range of 10^{-6} mbar and a rotary vane pump providing the required prevacuum for the high vacuum pump and cleaning of the gas dosing system. The pressure in the chamber could be monitored by a MKS type 626 pressure gauge for pressures above 1 mbar and by a cold cathode Balzers pressure gauge type IKR 260 for pressures below 0.1 mbar. Gases could be introduced into the chamber via a UHV gas dosing valve.

Scheme 3.2 shows the setup of the infrared measurements.

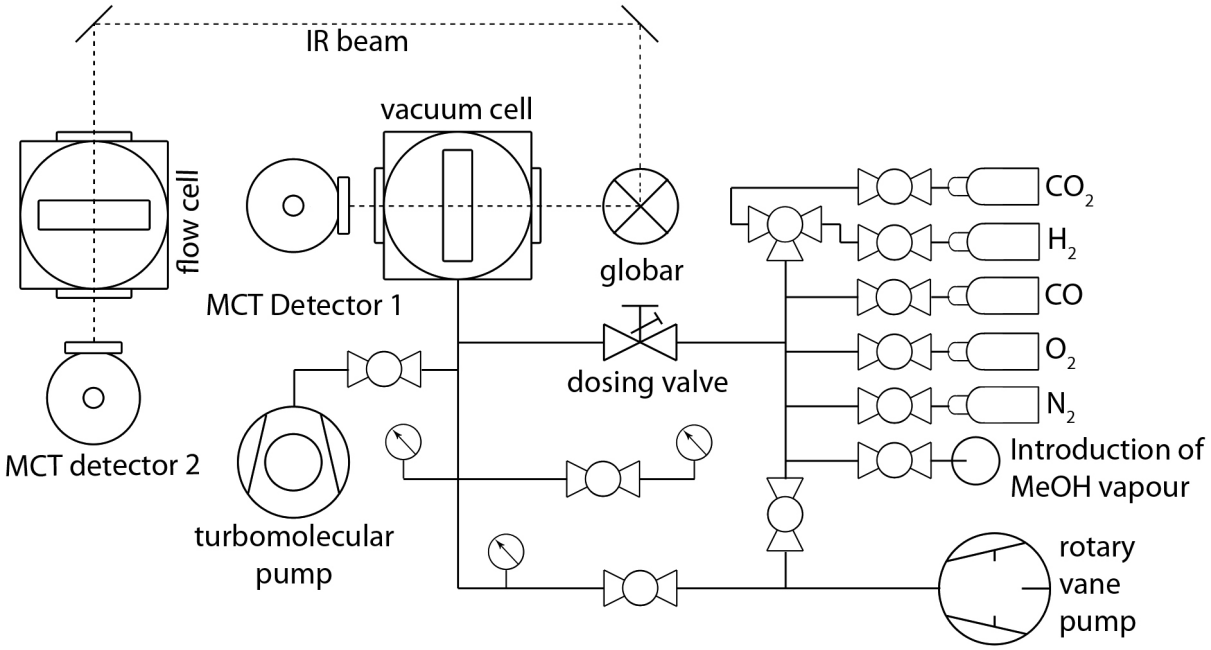

Scheme 3.2: Setup for the IR measurements.

3.4.2 Acquisition of the Spectra

The resolution was set to 4 cm^{-1} and spectra were acquired in the frequency range of 800 – 4000 cm^{-1}. For each spectrum 256 scans were averaged in order to obtain a good signal to noise ratio, except for the measurements performed at 158 K, which were partly acquired by averaging only 128 scans, because of a shorter acquisition time. The aperture was chosen corresponding to the sample from 1.5 – 2.5 mm for ensuring sufficient infrared radiation transmission.

A spectrum, obtained in a completely evacuated chamber without inserted sample, served as a background for all spectra. Furthermore, directly before the adsorption of gas molecules spectra of the clean samples were acquired in vacuum or in oxygen at the same temperature. These spectra were subtracted from the according spectra with the molecules adsorbed.

3.4.3 Pretreatment and Adsorption Measurements

In the vacuum cell all samples were treated the same way: First the samples were oxidized at 250 °C for 30 min in 100 mbar oxygen. Having cooled down the sample to 30 °C a ramp of 4 °C/min up to 250 °C was started, acquiring a spectrum every 2 min. After evacuation and cooling down to about -110 °C a background spectrum for the later on subtraction was

measured and subsequently 5 mbar of CO were dosed into the chamber. A spectrum was recorded at -110 °C in 5 mbar CO before evacuating for 5 min and acquiring another spectrum at the low temperature in vacuum. Then the sample was heated again to 250 °C in 100 mbar O_2, kept at the temperature for 30 min and cooled to 30 °C. After evacuation and acquisition of the background spectrum in vacuum at that temperature, 0.5 mbar of methanol were dosed into the chamber. A spectrum was recorded with 0.5 mbar methanol in the gas phase and after evacuation for 5 min. Then again the temperature ramp with 4 °C/min was started while evacuating and recording a spectrum every 2 min.

The same procedure was performed after reduction pretreatment. Reduction was done in 80 mbar of H_2 mixed with 720 mbar of nitrogen; the reduction temperature and the dwell time at this temperature were 250 °C and 30 min as in the oxidative pretreatment.

For the measurements in the flow cell the same pretreatment and reaction parameters as used for the kinetic measurements were applied. (see chapter 3.5.)

3.5 Kinetic Measurements

3.5.1 Experimental Setup and Evaluation of the Chromatograms

For the steady state kinetic measurements the same apparatus was used as for the TPReaction measurements (chapter 3.1.1. and scheme 3.1). However, in the kinetic measurements a gas chromatograph, HP 6890 equipped with a Plot Q column (30 m x 0.53 mm x 40 µm), served as detection device for quantitative analysis of the gas phase composition. The injection of the samples was realized with a 6-port valve connected to the product flow, a sample loop of a constant volume (0.25 ml) and the column. As detection unit in the gas chromatograph an FID was employed to detect all carbon containing substances. The oven temperature program was adjusted in a way that all expected peaks were thoroughly separated.

The obtained chromatograms were evaluated by the peak areas. For each substance a calibration (peak area versus amount of the substance) was performed resulting in a factor that could be applied for the quantitative analysis. Since a methanizer was installed before the detection unit, CO and CO_2 were converted to CH_4 prior to being detected by the FID. As a result the detector has the same sensitivity for these three gases.

3.5.2 Carrying Out Kinetic Measurements

The amount of the samples was varied from 10 to 20 mg. The pretreatment was always performed at 250 °C with a dwell time of 30 min both in oxidizing and in reducing conditions. For an oxidative pretreatment 70 ml/min of synthetic air were flown through the reactor, for a reductive pretreatment 70 ml/min of a 20 % H_2 / N_2 mixture were used. The sample was cooled to the respective reaction temperature varying from 40 to 200 °C in the same gas flow as for the pretreatment. After reaching the desired reaction temperature, the reaction gas mixture was flown over the catalyst isothermally. After 5 min, to allow for stabilization of the system, GC measurements were started every 17 min. The reaction gas mixture consisted of 2 % MeOH (achieved by flowing He of a determined flow through a saturator containing liquid methanol, kept at 0 °C) and 2 % O_2 in He at a total flow of 25, 50, 75 or 100 ml/min.

3.5.3 Temperature Difference Measurements

One of the expected benefits of the hybrid materials is the improved heat management in the catalytic reaction due to the excellent thermal conductivity of the CNTs, avoiding hotspots because of the exothermicity of the methanol oxidation. In order to evaluate the impact of the thermal conductivity of the CNTs during the reaction, the steady state kinetic measurements were repeated at selected temperatures. This time, however, a second thermocouple was introduced into the quartz glass tube, so that one thermocouple was positioned 5 cm above the catalyst directly in the quartz wool and the second thermocouple 15 cm above the catalyst. The second thermocouple should regulate the oven without being influenced by the exothermic reaction on the catalyst; the first thermocouple, which was positioned notably closer to the catalyst bed, should just read out the temperature near the catalyst surface. Apart from the alteration of the setup by the additional thermocouple the measurements were performed in exactly the same way as described in 3.4.2. with 10 mg of catalyst at a total flow of the reaction gas mixture of 100 ml/min.

4 Results and Discussion

4.1 Transmission Electron Microscopy

4.1.1 Bi_2O_3 Samples

The reference Pd-Bi_2O_3 sample could neither be evaluated in the brightfield TEM measurements, because of the low Z contrast of Pd and Bi_2O_3, nor did STEM analysis combined with EDX bring about clear results. For this reason it was tried to determine the size of the Pd particles on the metal oxide by two other methods. The first one was X-ray diffraction (XRD) analysis. However, due to the low percentage of Pd in the sample (2 wt%) this technique was not sensitive enough to detect Pd nanoparticles on the bulk oxide. Therefore, no reflections of crystalline Pd were found in the diffractogram. Nevertheless, XRD revealed that at apart from the monoclinic Bi_2O_3 a second phase, the carbonate $Bi_2O_2CO_3$, was present in the sample. The low quality of the reflections attributed to this phase made a quantitative analysis impossible, meaning in turn that the content of $Bi_2O_2CO_3$ must be lower than 3 wt%. When comparing the diffractograms before the Pd impregnation and after the impregnation, a difference of the reflections was realized, although no additional reflections for Pd emerged: While the reflections of the carbonate phase stayed within the range of statistical fluctuations, the intensities of monoclinic Bi_2O_3 were altered, being a hint for the presence of Pd. The diffractogram of the pure Bi_2O_3 and a comparison with the impregnated sample can be found in the attachment.

In a second approach it was tried to do a quantitative chemisorption analysis with H_2 and CO as analysis gas to determine the accessible Pd surface and thereby the dispersion of the Pd particles. However, neither this technique allowed a calculation of reliable results.

TEM measurements of the Bi_2O_3-CNT samples (figure 4.1) revealed that Bi_2O_3 was extensively coating the nanotubes in a layered way. Only few bigger crystals were attached to the tubes in a particulate manner. It seemed that in most parts of the sample a homogeneous coating was achieved. The crystalline coating of the carbon nanotubes could not be proven. Although in HRTEM images lattice fringes were visible, they could not be attributed to a Bi_2O_3 crystalline phase, but seemed to stem from the graphitic structure of the carbon nanotubes. Furthermore, the measurable space between the atomic planes varied according to the curvature.

The diameter of the nanotubes varied from ~5 to ~100 nm, including the metal oxide coating.

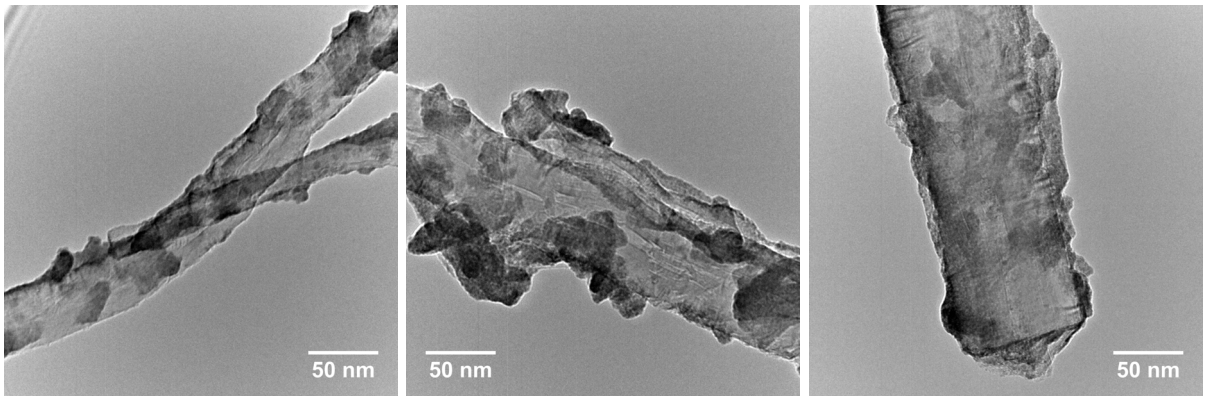

Figure 4.1: TEM images of Bi_2O_3-CNT

The Pd-Bi_2O_3-CNT sample showed a similar picture (figure 4.2). The nanotubes' diameters were ranging from ~5 to ~100 nm and they were in large parts coated with the metal oxide. Additionally, in this sample finely dispersed small dots were visible. These dots had a rounded hexagonal or elliptical form, which is characteristic of Pd crystals. Due to their characteristic form, the contrast and the comparison to the hybrid sample without the Pd impregnation step, they could definitely be attributed to Pd nanoparticles, grown on the surface. The Pd particles were observed on the oxide coating as well as on pure carbon nanotubes that have not been coated. The diameter of the Pd-nanoparticles ranged from ~2 to ~7.5 nm with an average value of 5.1 nm.

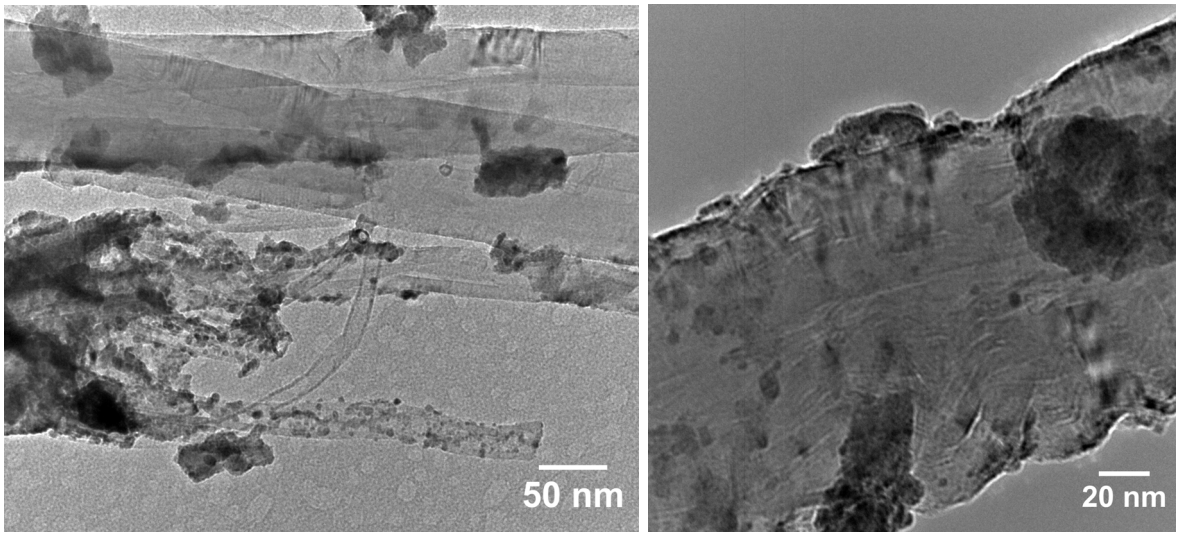

Figure 4.2: TEM images of Pd-Bi_2O_3-CNT

4.1.2 V_2O_5 Samples

The reference vanadium oxide samples impregnated with palladium were reduced before the TEM measurement. As the oxide particles were rather big, an analysis could only be performed at the edges of the material (figure 4.3). Palladium particles could be identified, due to their shape and the Z-contrast. High resolution images of the edges enabled the visualization of lattice fringes, which did not arise from atomic planes of Pd crystals, but were attributed to crystalline VO_x phases. The palladium particles seemed to be rather homogeneously distributed over the surface. Their size ranged from ~3 to ~6 nm with an average particle diameter of 4.5 nm.

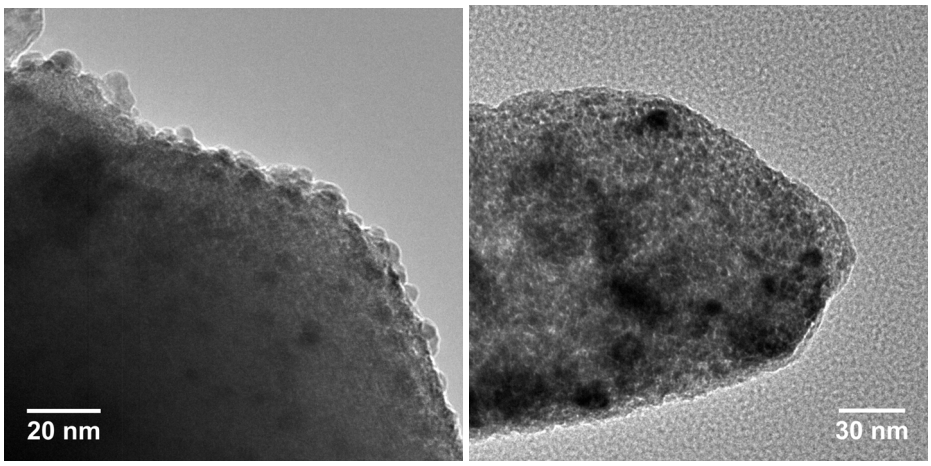

Figure 4.3: Tem images of Pd-V_2O_5

The V_2O_5-CNT samples were prepared in two different ways. In one attempt benzyl alcohol was used as a linker, in the other batch the synthesis was performed without any linker. The results of the TEM analysis showed that the coating of the nanotubes was very dense, but particulate, if a linker was used. (figure 4.4) Crystal-like particles of ~25 – 45 nm were covering the tubes and were attached vertically to them. In some areas the crystals had agglomerated to bigger particles.

In contrast to this sample, the one prepared without benzyl alcohol as a linker was covered less densely with the metal oxide; however, most of the metal oxide particles were attached to the tubes in layers. Perpendicularly oriented particles appeared in most cases in combination with agglomerated particles. (figure 4.5) The size of the metal oxide particles which seemed to cover the nanotubes' surface as a layer was approximately in the same range as the size of the particles on the sample prepared with the linker (~30 nm). However, perpendicularly oriented particles seemed to be bigger with a length up to 80 nm.

For both samples the shape of the metal oxide particles could be a hint for a crystalline, in many parts non-amorphous coating. Their elongated shape with sharp edges reminded of a tetragonal form.

Compared to the Bi_2O_3-CNT sample the coverage of the V_2O_5-CNT sample prepared without a linker was less dense, but the metal oxide particles seemed to be more crystalline. The diameter of the nanotubes with the V_2O_5 coating was approximately in the same range as the one of the nanotubes with the Bi_2O_3 coating: 5 -100 nm.

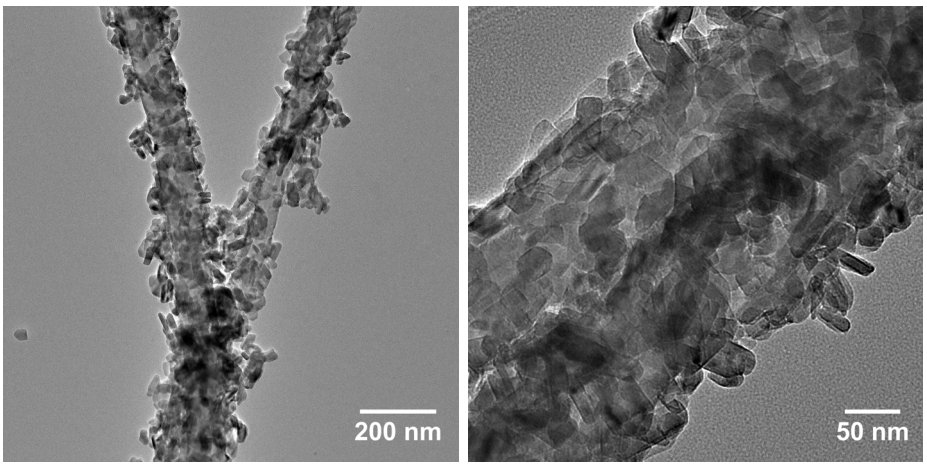

Figure 4.4: Tem images of V_2O_5-CNT synthesized with benzyl alcohol as a linker

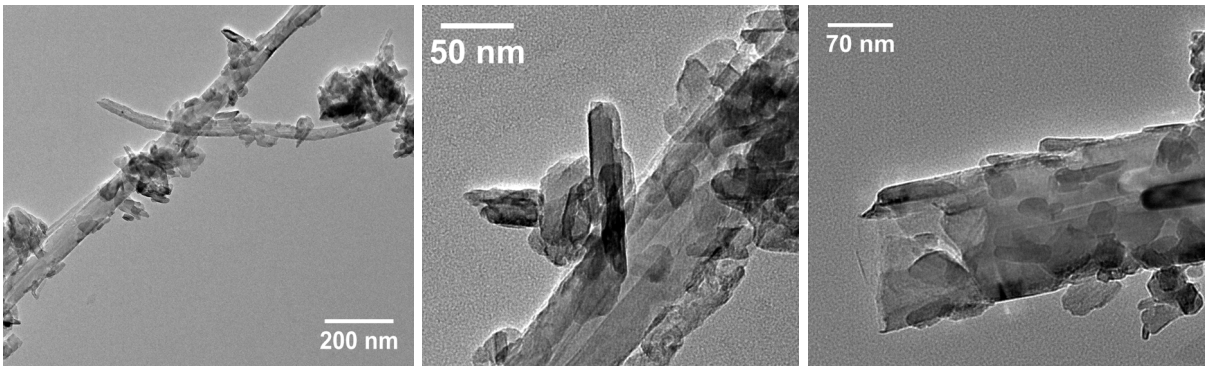

Figure 4.5: TEM images of V_2O_5-CNT synthesized without a linker.

The impregnation step for the V_2O_5-CNT sample with Pd led to the same results as the impregnation of the Bi_2O_3-CNT sample, concerning palladium: The Pd particles were finely dispersed on the sample, both on the nanotubes which were not covered (~10 %) and on the metal oxide. Their size ranged from 4 – 8 nm with an average size of 5.9 nm. Again the Z-contrast and the shape of the particles served as a basis for the identification of Pd on the sample. (figure 4.6)

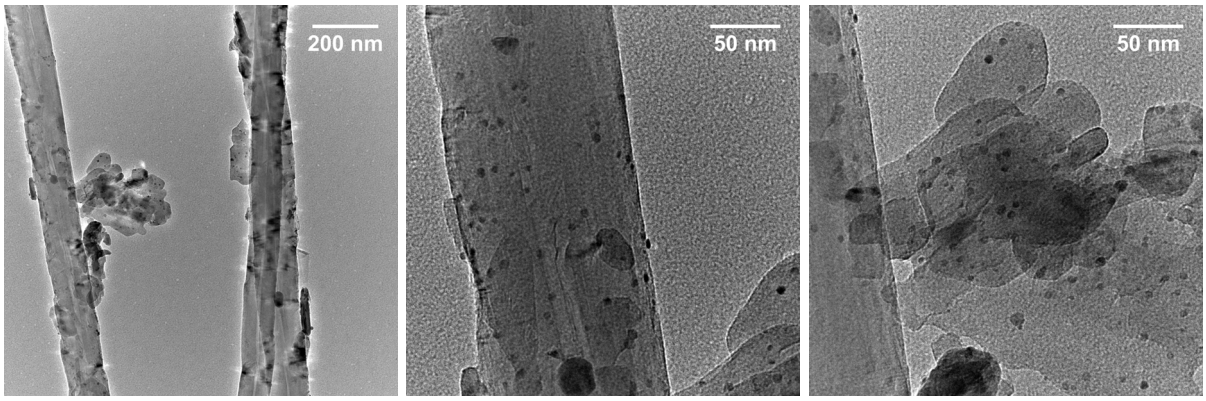

Figure 4.6: TEM images of Pd-V_2O_5-CNT

4.2 Temperature Programmed Reaction

4.2.1 Bi_2O_3 Samples

TPReaction measurements revealed that samples containing Pd and Bi_2O_3 were active already at low temperatures (~70 °C). The observed products were in all samples the same: water, hydrogen, carbon dioxide, carbon monoxide, methyl formate and dimethylether. Nevertheless, the temperatures, where the formation of certain products and the consumption of MeOH and O_2 were observed, depended on the catalyst and on the pretreatment. MFA was observable as a peak in a certain temperature range (about 60 – 190 °C). Characteristic masses of this molecule that could be detected in presence of methanol were 60 and 59. The formation of CO_2, water and DME increased steadily from about 60 °C on up to a constant level. Typical ion masses of CO_2 and its fragments are 44, 28 and 12. For the identification of CO_2, however, the ion mass 44 was most relevant, since 12 and 28 could stem from other molecules as well. The ion masses 17 and 18 in turn, are very characteristic of water. In the analyzed spectrograms the slope of these two masses was about the same, indicating that the trend was reliable. For DME several ion masses are characteristic; however, considering the possible other molecules being present, only the same trend of the mass signals 45 and 46 gave reason for the assumption that DME was indeed formed: Other fragments of DME were masked by methanol fragments and the ion mass 45 is a characteristic fragment of dimethoxymethane as well. However, DME shows no signal at m/z 75, which is another characteristic fragment of dimethoxymethane. As a result the presence of a signal at m/z 45 and 46 and the absence of a signal at the ion mass 75 ensured that DME was formed.

In all measured samples the ion mass 2, representing hydrogen, showed a trend with temperature that differed from all other ion masses. In all samples the same trend for the ion mass 28 and 2 could be monitored at temperatures higher than 200 °C, however, by far stronger on the reference samples: Both ion mass signals increased steadily from 200 °C onwards, 2 much stronger than 28. Although the mass 28 can be attributed to several molecules, in this case CO seemed to be the most appropriate assignment, since for no other ion mass the same trend could be observed. The fraction molecules of CO which should be observable with lower intensities – 12 and 16 – were masked by other molecules, so that they did not allow a backup of this assumption. The ion mass 2 only represents hydrogen. The observation of CO and H_2 production seemed to be an evidence for the known reaction of methanol decomposition on Pd to CO and H_2. Below 200 °C the ion mass signal 28 was more or less constant; 2, however, showed in nearly all measurements a negative peak, exactly at the same temperatures, where a strong decrease of the masses for methanol and oxygen could be observed. Since also the ion mass 4, representing the constant He flow, decreased in the same temperature range, this phenomenon was attributed to the strong change of the partial pressures in the detection system caused by the rather sudden product formation. Low ion masses (such as 2 and 4 for H_2 and He) are known to be difficult to detect. Therefore, these observed features were assigned rather to baseline effects than to a reduction process in the sample.

The only sample, where a positive peak of the hydrogen signal could be observed in a temperature range from 80 – 210 °C, before an increase of this signal set in above 200 °C as observed in every sample, was the reduced reference sample Pd-Bi_2O_3. Obviously, on this sample reactions forming H_2O and H_2 started at 80 °C. However, at ~150 °C the product formation changed in favor of water. At 200 °C a completely different reaction which was producing hydrogen – the methanol decomposition – set in.

In all spectra it was clearly visible that the formation of products involved a decrease of the reactants. Therefore, a decline of the mass signals 32 and 16, representing oxygen, and of the masses 31, 30, 29, 15, 14 and 13 being fragment ions of methanol could be observed in parallel to an increase of the intensities of product molecule masses.

Since the fragment ion masses of methanol and formaldehyde coincide, formaldehyde could not be detected reliably by this technique, if it is not formed in big quantities. However, other techniques such as gas chromatography revealed that formaldehyde did not arise on Bi containing samples.

The most informative ion masses detected on the Bi containing samples are displayed in figures 4.7 to 4.10.

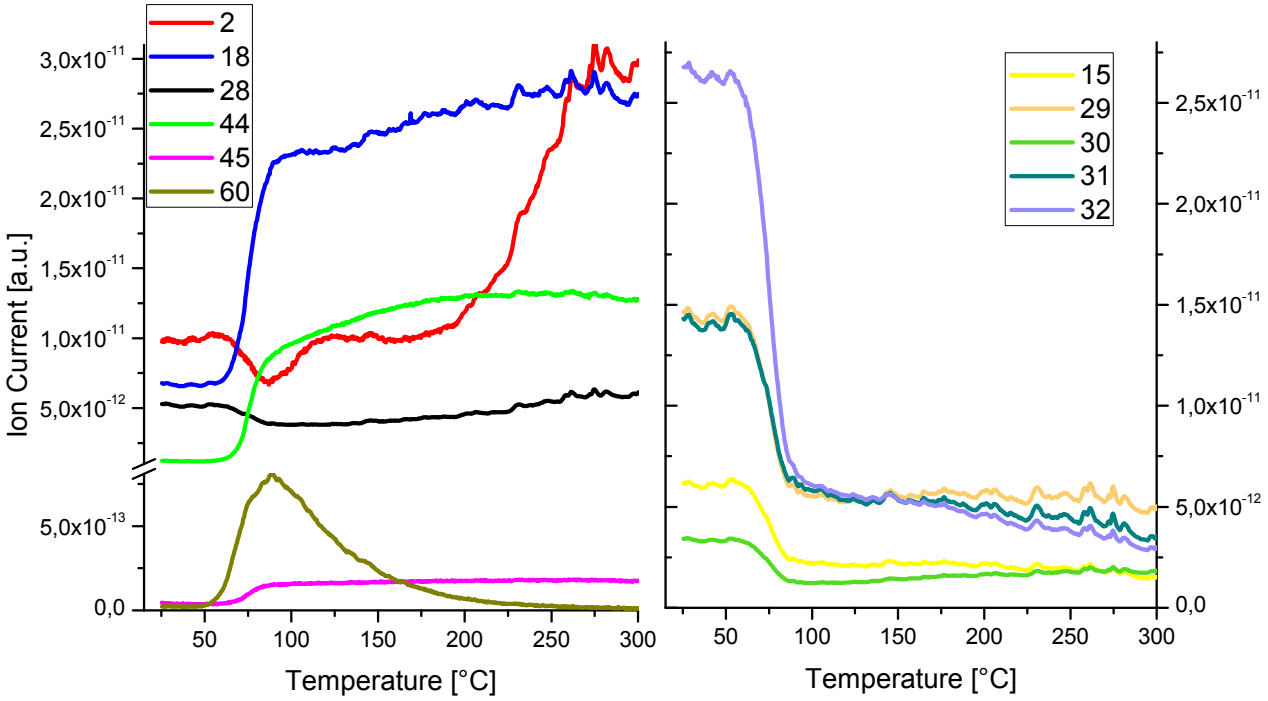

Figure 4.7: TPReaction measurement of methanol oxidation on the oxidized Pd-Bi_2O_3 catalyst.

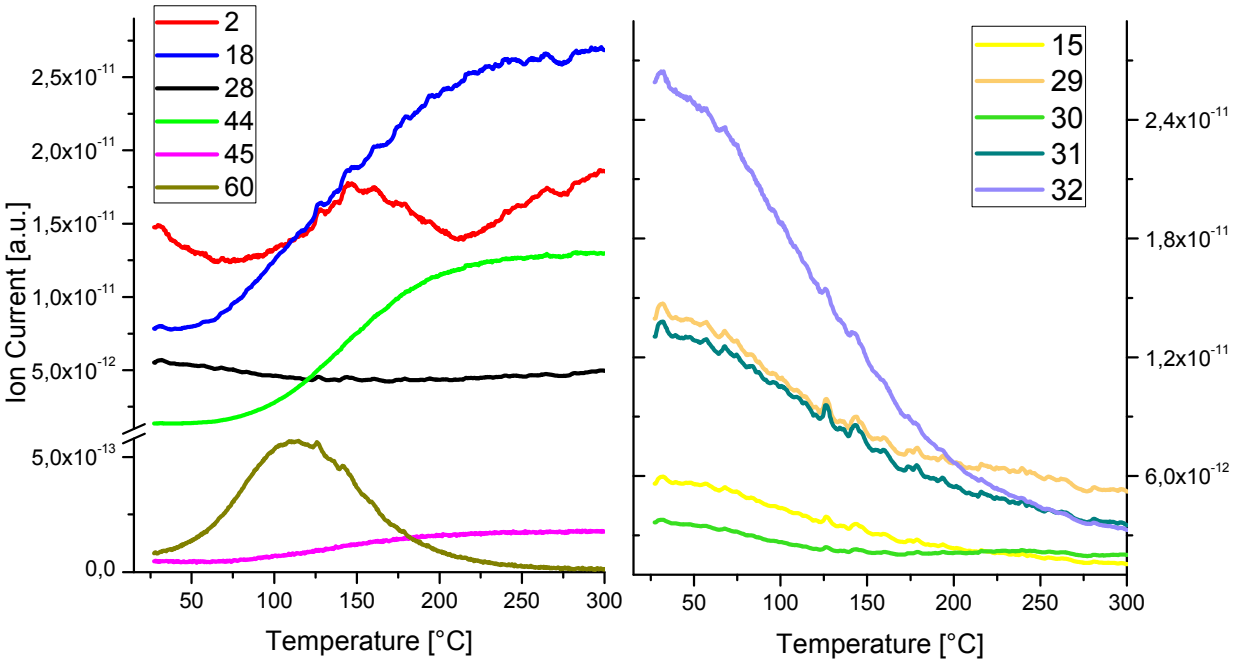

Figure 4.8: TPReaction measurement of methanol oxidation over the reduced Pd-Bi_2O_3 catalyst.

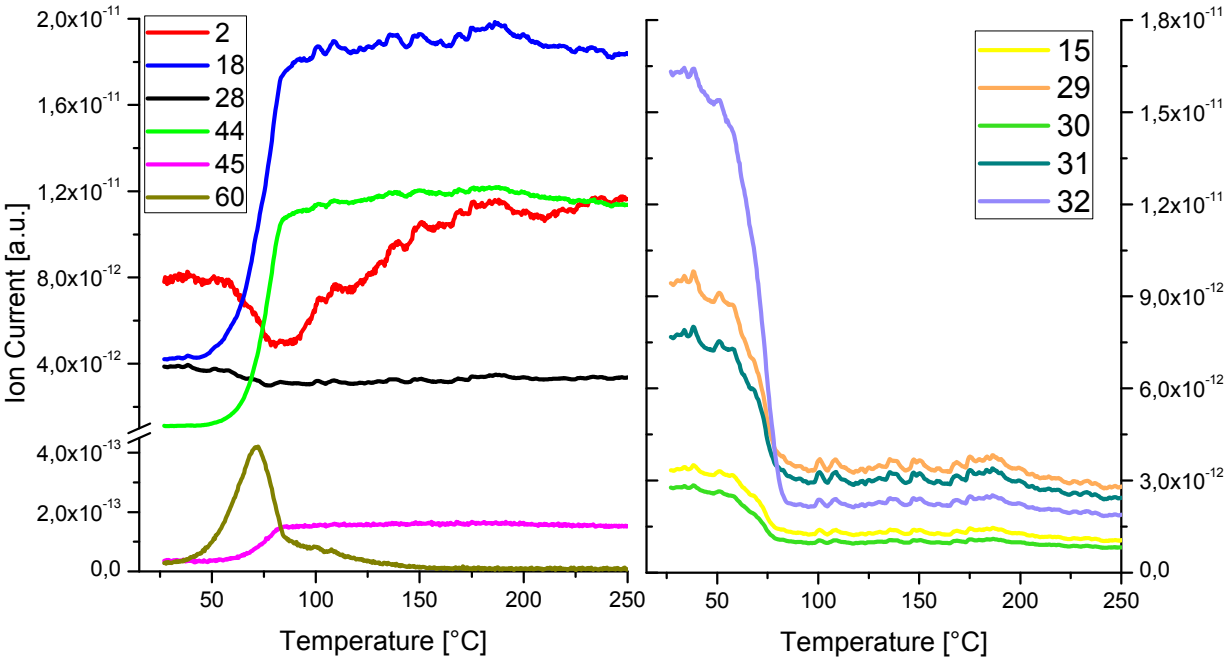

Figure 4.9: TPReaction measurement of methanol oxidation over the oxidized Pd-Bi_2O_3-CNT catalyst.

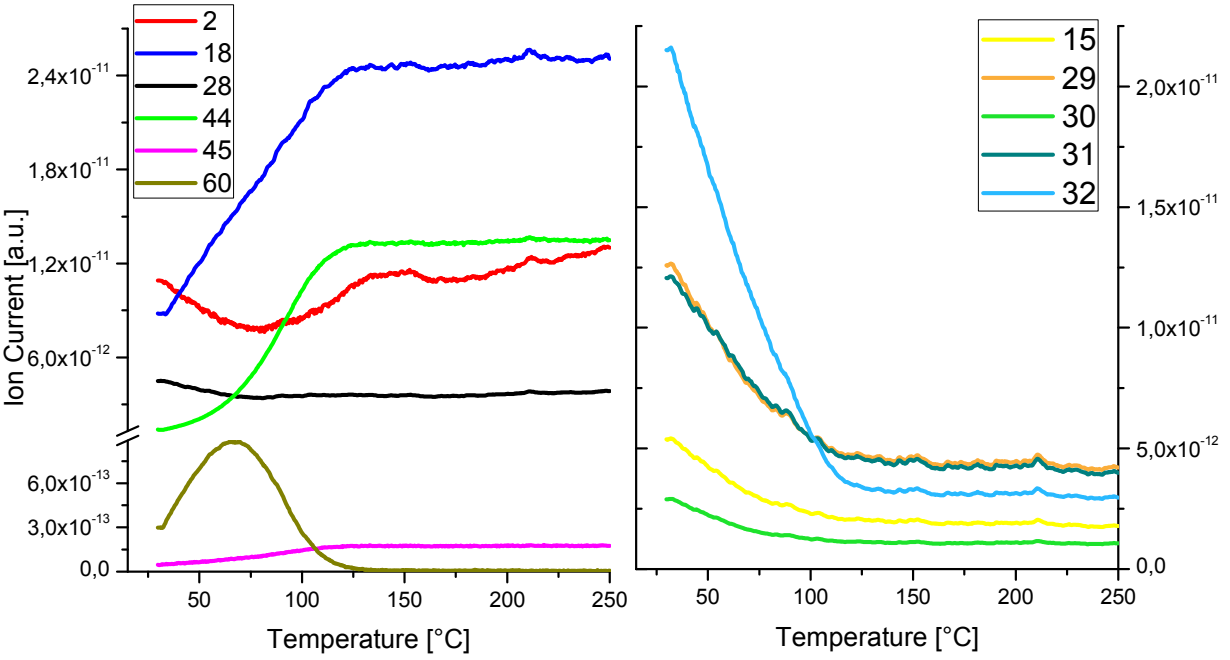

Figure 4.10: TPReaction measurement of methanol oxidation on the reduced Pd-Bi_2O_3-CNT catalyst.

Comparing the CNT based catalyst with the reference catalyst, reactions started at lower temperatures (~20 °C) and maxima in the product formation rates were reached faster and at lower temperatures over the hybrid material. However, the product formation trend was roughly the same for both Bi_2O_3 containing samples.

A difference could be observed when applying different pretreatments: After reduction the reaction started already at room temperature. Nevertheless, the product formation rate increased much more slowly upon heating compared to the oxidizing pretreatment, where a steeper increase was detected. Regarding the formation of MFA, which took place only in a narrow temperature range, the effect of the pretreatment on the reference and hybrid sample was different. On the reference sample the MFA formation (mass signals 59 and 60) started at lower temperatures after reduction; however, the peak was broader with a maximum at a higher temperature (110 °C) than after oxidation (90 °C). On Pd-Bi_2O_3-CNT the formation of MFA started already at 30 °C (which equaled to the start temperature of the measurement) both after oxidation and reduction. Also the temperature of the peak maximum was about the same (~70 °C). However, after oxidation the peak was sharper than after reduction.

The observed temperature trends are summarized in table 4.1

Table 4.1: Temperature range of product formation observed in the TPReaction measurements over Pd-Bi_2O_3 and Pd-Bi_2O_3-CNT samples

m/z	**12, 44 (CO_2) 17, 18 (H_2O) 45, 46 (DME)**	**59, 60 (MFA)**	**16, 32 (O_2) 13, 14, 15, 29, 30, 31, 33 (MeOH)**
Temperature [°C]	increase to a plateau	peak range / peak maximum	decrease to a plateau
ox. Pd-Bi_2O_3	60 - 90	50 – 230 / 90	60 - 90
red. Pd-Bi_2O_3	60 - 230	30 – 250 / 110	60 - 230
ox. Pd-Bi_2O_3-CNT	45 - 85	30 – 150 / 71	45 - 85
red. Pd-Bi_2O_3-CNT	30 - 125	30 - 125 / 68	30 - 125

Finally, the results were compared to the Pd-CNT sample, which only contained Pd particles on CNTs. Figure 4.11 displays the results of the TPReaction measurement on this sample

after oxidation. Very similar products were detected as on Pd-Bi_2O_3 samples. Although the reaction products were the same, the relative intensities of the formed products were different. DME could hardly be detected, due to the absence of acid sites present on the oxide; in turn the relative intensity of MFA was higher than on the Bi_2O_3 containing samples. The temperatures, where reaction products were formed, were comparable to those on the Pd-Bi_2O_3-CNT hybrid material. Overall, most reactions occurring on the Pd-Bi_2O_3 samples seem to be catalyzed by Pd. Hardly any influence of the oxide component was observed, except for DME formation, which proceeds on acidic sites on the oxide surface.

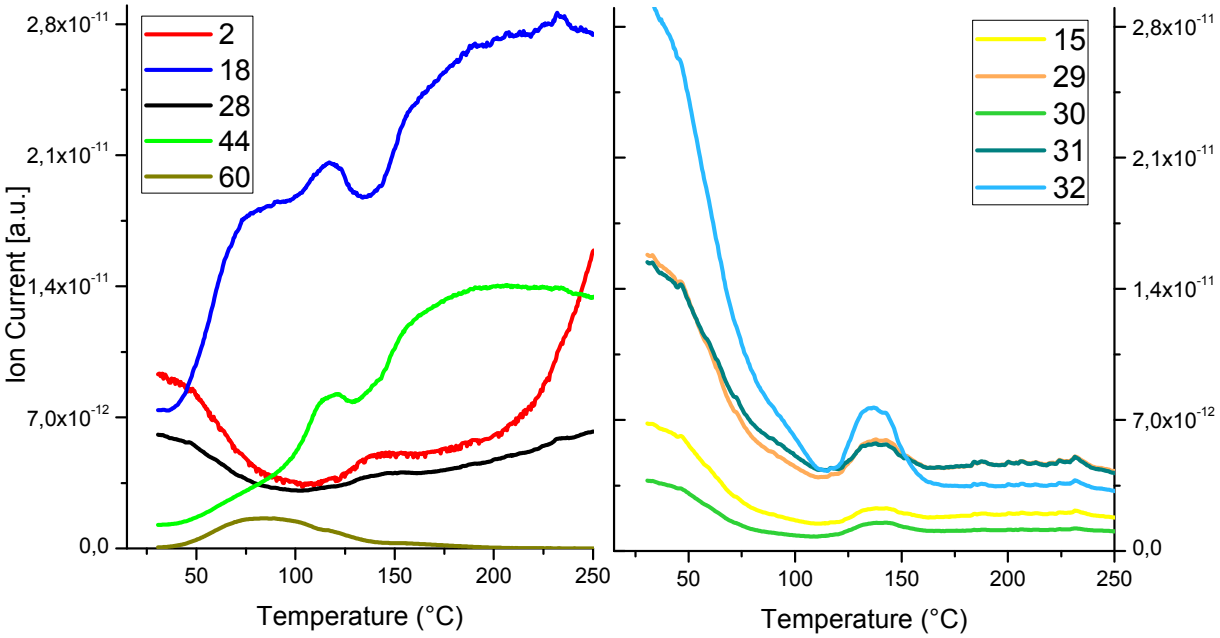

Figure 4.11: TPReaction measurement of methanol oxidation over oxidized Pd-CNT.

4.2.2 V_2O_5 Samples

In general, the V_2O_5 containing catalysts were active at higher temperatures compared to the Bi_2O_3 containing samples. Furthermore, more different products formed on the V_2O_5 containing catalysts: Water, carbon dioxide, carbon monoxide, hydrogen, methyl formate, dimethyl ether, dimethoxymetane and formaldehyde were detected. The presence of formaldehyde in the product stream was evidenced by IR spectroscopy and GC. FA could not be registered by MS, because fragments of the methanol feed masked the mass signals of FA, which was formed only in low quantities.

The formation trend of CO_2, H_2O and DME with temperature was similar. First the intensities of the characteristic masses of CO_2, H_2O and DME increased very quickly with temperature; in the following temperature range, the intensities increased only slightly, before they decreased again at ~250 °C. As already mentioned above, the characteristic masses for these molecules are 44 for CO_2, 17 and 18 for H_2O and 45 and 46 for DME. For DME the ion mass 46 was more informative, because of the formation of dimethoxymethane, which also contributed to the ion mass 45.

The ion masses 45 and 75 showed a peak in a very narrow temperature range (about 50 - 100 °C). Another peak in a broader temperature range was recorded for the ion masses 59 and 60 (about 100 - 200 °C). The exact temperature ranges, however, strongly depended on the sample and are summarized in table 4.2. The peak of the ion masses 45 and 75 was found in all of the samples and was assigned to DMM formation. The mass signal 75 went back to the initial level, while the mass signal 45 stayed at a higher level than the initial intensity value. This was caused by the simultaneous formation of DME and DMM. While DMM was only formed in a narrow temperature range (about 50 – 100 °C), DME formation also took place at higher temperatures (>100 °C). The ion masses 59 and 60 were attributed to MFA. According to the measured data, MFA was produced over a wider temperature range than DMM with a peak maximum at higher temperatures (~120 °C).

Like on the Bi_2O_3 containing samples the intensities of the ion masses 2 and 28 increased only at higher temperatures. (>200 °C) The increase of 28, representative of CO, started already at lower temperatures than the increase of hydrogen (2). Over all samples the hydrogen production started very suddenly in large quantities. In the temperature range before the hydrogen formation, a decrease of this mass signal was observed. This decrease may be partly due to the decrease of the concentration of methanol, which influences the ion mass 2 as well, and partly due to reduction processes.

The ion mass signals 15, 16, 29, 30, 31 and 32, which were characteristic of the reactants MeOH and O_2, all showed the same trend: When the increase of CO_2 and water formation was observed, these masses decreased. At even higher temperatures a further decrease was observable, accompanied by the increase of the ion mass signals 2 and 28 which indicated further decomposition of methanol to CO and H_2.

Overall, several reactions proceeded on the Pd-V_2O_5 catalysts. DME and DMM e.g. formed on the acid sites of V_2O_5. In literature [6] it was suggested that DME is the intermediate in the DMM formation. Since DMM could be observed only in a very narrow temperature range, it

seemed that already slightly higher temperatures entailed desorption of the intermediate DME before further reaction to DMM.

MFA was also formed only in a certain temperature range (100 - 200 °C). In contrast, carbon dioxide evolved over the whole measured temperature range. It is likely that too high temperatures entailed the total oxidation, whereas at lower temperatures more MFA formed and desorbed from the surface. Above 200 °C the decrease of water and CO_2 production evidenced that the reaction mechanism changed towards hydrogen and CO formation, indicating methanol decomposition catalyzed by the Pd.

Figures 4.12 to 4.15 show the mass spec traces of the most relevant ion masses.

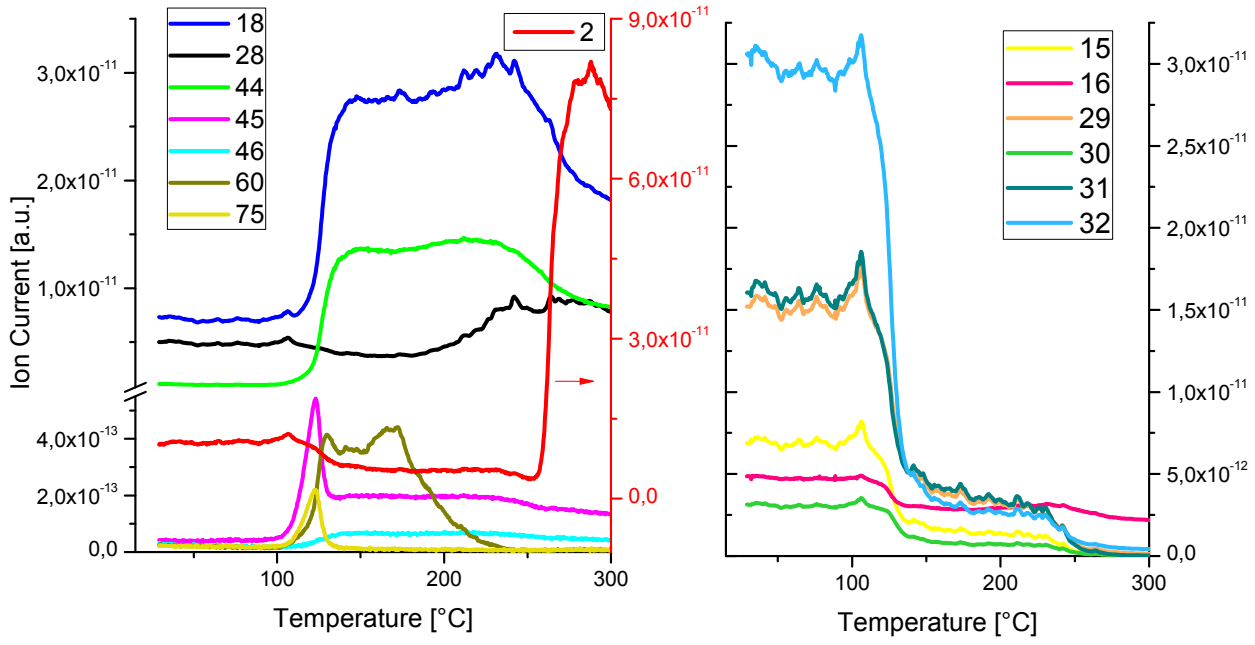

Figure 4.12: TPReaction measurement of methanol oxidation over Pd-V_2O_5; the pretreatment was performed at 250 °C under oxidizing conditions.

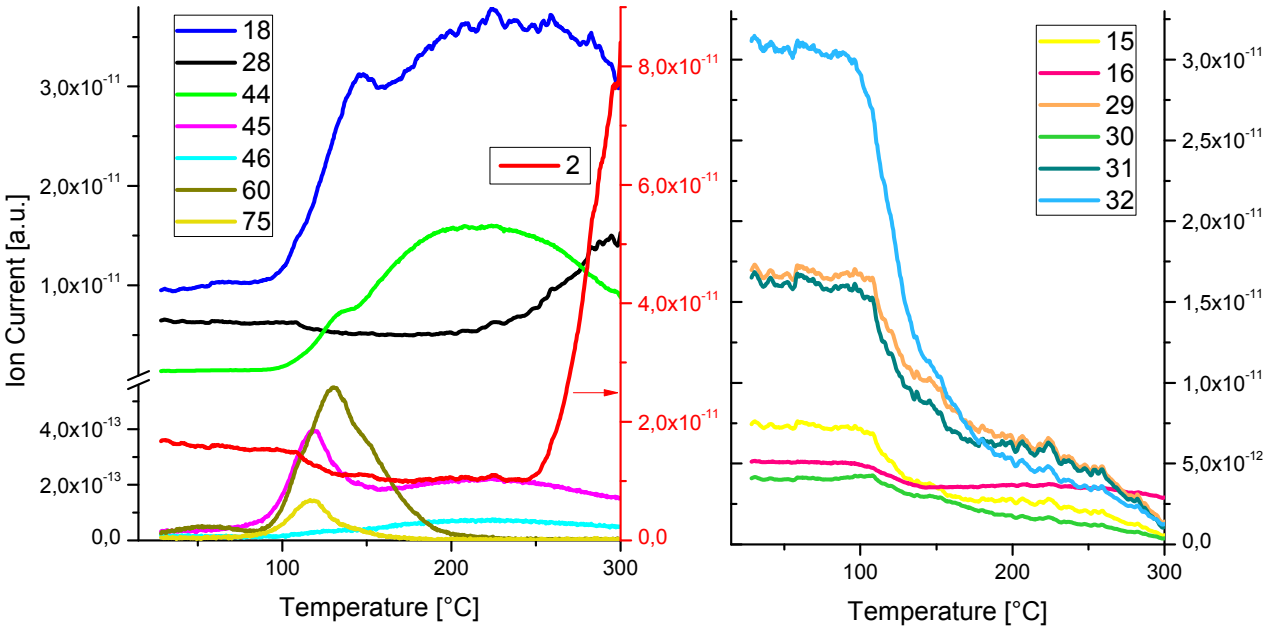

Figure 4.13: TPReaction measurement of methanol oxidation on Pd-V_2O_5; the pretreatment was performed at 250 °C under reducing conditions.

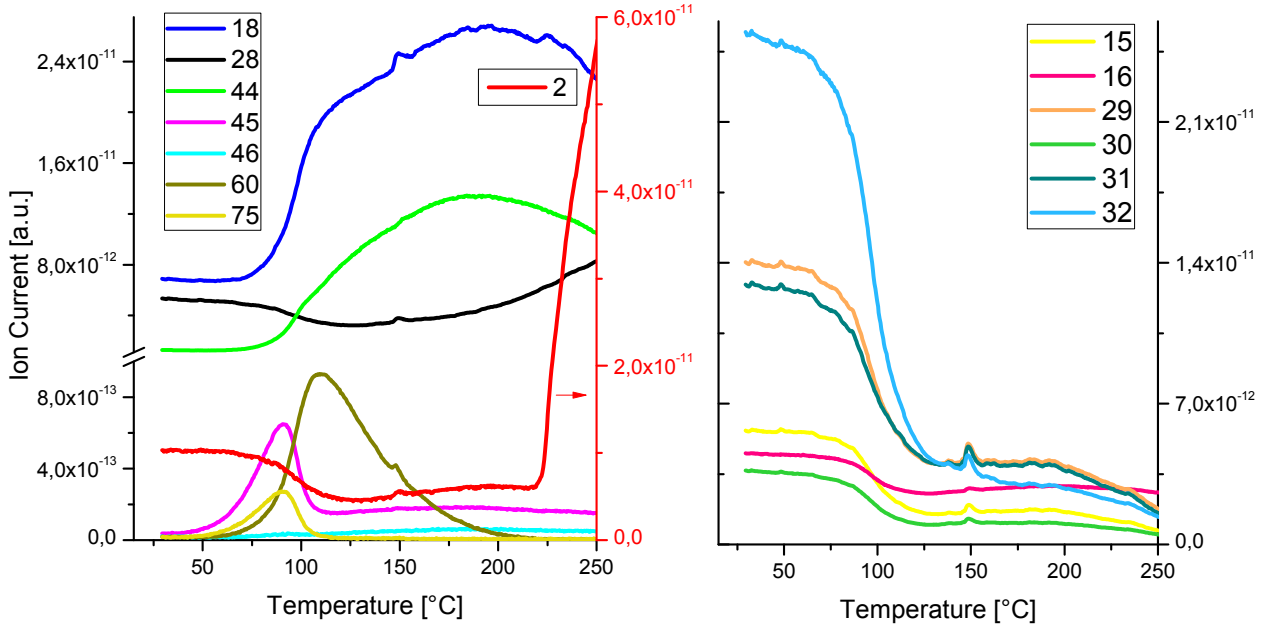

Figure 4.14: TPReaction measurement of methanol oxidation over Pd-V_2O_5-CNT; the pretreatment was performed at 250 °C under oxidizing conditions.

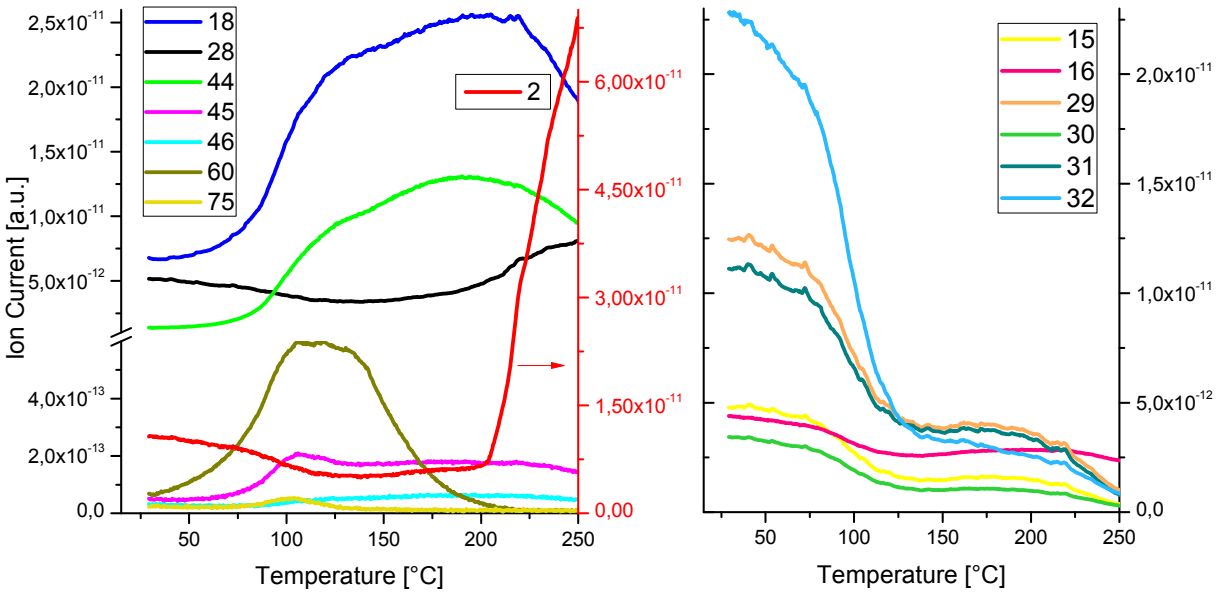

Figure 4.15: TPReaction measurement of methanol oxidation on Pd-V_2O_5-CNT; the pretreatment was performed at 250 °C under reducing conditions.

When comparing the hybrid sample with the reference sample, again a shift of all reactions to lower temperatures could be observed. (see table 4.2) Even the decomposition process of methanol to CO and H_2 started at lower temperatures.

The difference between oxidizing and reducing pretreatment was marginal for the hybrid sample. On the reference sample, however, the pretreatment conditions seemed to be crucial, as the temperatures at which the reactions set in were distinctly lowered by a reducing pretreatment (by ~20 °C). Interestingly, variation of the oxidation temperature had a strong effect on the reactivity: When the Pd-V_2O_5 catalyst was pre-oxidized at 300 °C, it was only active at about 200 °C, whereas the same catalyst pretreated at 250 °C was already active at about 120 °C. It is likely that an oxidation process took place in the temperature range from 250 °C to 300 °C, which was responsible for the temperature shift in the catalytic activity. Another possible explanation could be a different degree of (de)hydroxylation of the V_2O_5.

A further difference between the oxidation at 250 °C and 300 °C was observed for the trend of the mass signals of CO_2 and water. While after oxidation at 250 °C the mass signals 17, 18 and 44 first increased fast with temperature followed by a slower increase and a decrease above 250 °C, after oxidation of Pd-V_2O_5 at 300 °C the regime of a slow increase of the masses was missing: Directly after the strong increase of the intensities of the signals for

CO_2 and water from 160 – 240 °C the decrease of the intensities followed. Figure 4.16 displays the spectrogram of TPReaction over Pd-V_2O_5 oxidized at 300 °C.

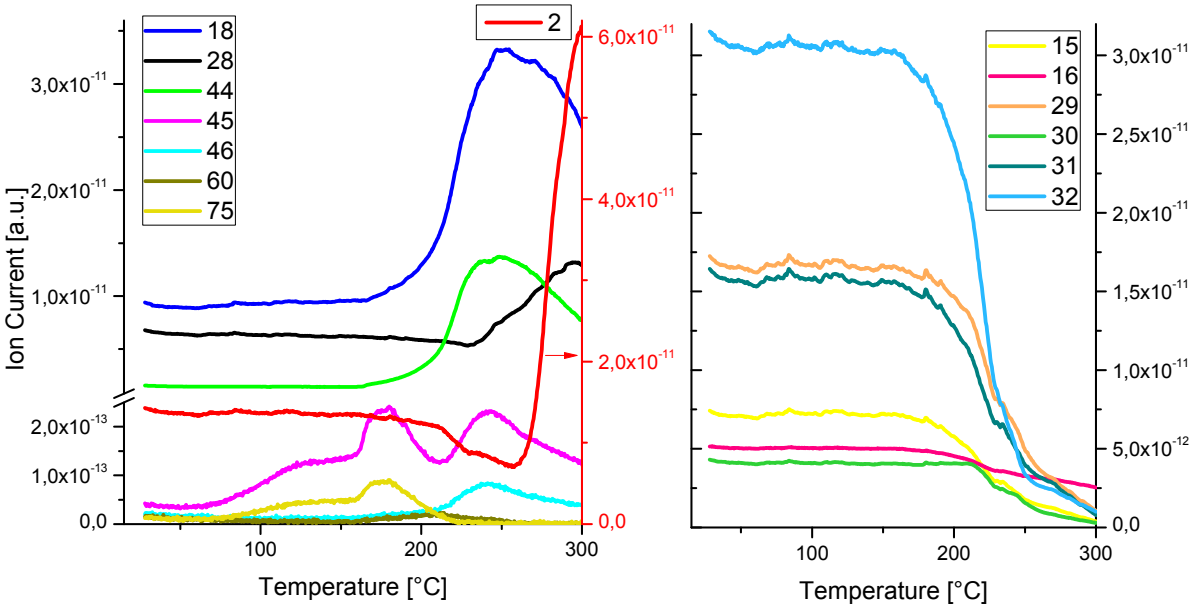

Figure 4.16: TPReaction measurement of methanol oxidation over Pd-V_2O_5; the pretreatment was performed at 300 °C under oxidizing conditions.

The temperature trends over the different samples and pretreatment procedures are summarized in table 4.2.

Table 4.2: Temperature range of product formation observed in the TPReaction measurements over Pd-V_2O_5 and Pd-V_2O_5-CNT samples.

m/z	17, 18 (H_2O); 12, 44, (CO_2); 46 (DME)		16, 32 (O_2);13, 14, 15, 29, 30, 31 (MeOH)		45, 75 (DMM)	59, 60 (MFA)	28 (CO)	2 (H_2)
Temperature [°C]	1st (strong) increase	2nd (weak) increase	decrease to plateau	further decrease	peak range / maximum	peak range / maximum	increase	increase
ox. Pd-V_2O_5	110 – 145	-	110 - 145	>230	95 - 135 / 122	100 - 240	>190	>250
ox. Pd-V_2O_5 (*)	160 - 240 (')	-	160 - 240	-	153 - 215 / 175	-	>230	>250
red. Pd-V_2O_5	90 - 135	145 - 200	90 -170	>250	90 - 150 / 120	80 - 200 / 130	>200	>250
ox. Pd-V_2O_5-CNT	70 - 120	120 - 180	70 - 130	>200	35 - 110 / 90	60 - 215 / 110	>160	>220
red. Pd-V_2O_5-CNT	60 - 130	130 - 200	60 - 130	>200	60 – 130 / 100	30 - 215 / 110	>150	>200

(') not for m/z = 46; instead peak of m/z = 45 and 46 from 200 – 300 °C (maximum at 240 °C)

(*) oxidation at 300 °C instead of 250 °C

4.3 Infrared Spectroscopy

Transmission infrared spectroscopy was a challenge with the hybrid samples, because of the high absorption of the black carbon nanotubes. Although spectra of acceptable quality could be obtained, adsorption studies turned out to be nearly impossible. In presence of gases only the gas phase was visible superimposed as peaks on the background of the sample absorption. Even in vacuum after adsorption of organic molecules no peaks of adsorbed species were detected. It is likely that the strong absorption of the sample together with the small amount of adsorption sites exposed to the infrared beam, made the detection of adsorbed species on the surface impossible. However, the reference samples provided information that is very likely transferable to the hybrid samples due to the similar reactions going on (described in 4.2). Both the Pd containing samples and the pure metal oxides were investigated to facilitate band assignment and interpretation.

4.3.1 CO Adsorption

Pure Bi_2O_3 appeared to be completely inert towards CO adsorption. No peaks in the relevant CO stretch vibration region could be observed. Only the region of carbonate vibrations around 1500 cm^{-1} was rich of absorption bands.

It was expected that the Bi_2O_3 sample impregnated with Pd would show the typical absorption bands of CO on palladium. [48-50] However, only reduced Pd-Bi_2O_3 provided the anticipated results:

On the reduced Pd-Bi_2O_3 sample an asymmetric band at 2065 cm^{-1} was detected in presence of CO in the gas phase. The band was assigned to CO on-top of Pd on different sites. It was not stable upon evacuation, which is unusual for Pd. However, the intensity of the absorption band was already very low in presence of the gas phase so that the complete disappearance in vacuum was not astonishing. The absence of bands of CO adsorbed at bridging or hollow sites (figure 4.18 a)) could be a hint to small Pd particles.

V_2O_5 on the contrary showed a variety of absorption bands: First, a broad absorption band was present from 2075 to 1960 cm^{-1} with peak maxima at 2025 and 1975 cm^{-1} prior to CO adsorption. (Figure 4.17) These bands were assigned to overtones and summation bands of bulk vanadyl groups (mainly V=O) observed at 1020 and 980 cm^{-1}. [51, 52] Further bands were observable at 1285 and 1205 cm^{-1} with a shoulder at 1345 cm^{-1}. They were suggested

to originate from overtone modes of the skeletal vibrations. [51] Although these bands should not change and consequently disappear after subtraction of the background spectrum, several features were observed in these regions (2100 – 1950 cm^{-1} and 1400 – 1100 cm^{-1}), when CO was present in the gas phase. However, these features did not stem from adsorbed species on the surface, but rather from slight shifts due to temperature differences at -110 °C, where stable thermal conditions were difficult to achieve, when the background pressure was varied.

The spectra of CO adsorption recorded for the reduced and oxidized V_2O_5 sample were very similar; however, some of the peaks slightly shifted. On both CO adsorption bands were observed at -110 °C in 5 mbar CO, but they were not stable upon evacuation. A weak broad peak at 2337 cm^{-1} with a shoulder at 2350 cm^{-1} was detected on the reduced and oxidized sample at the same position. According to literature [51] these bands could be attributed to CO_2, which likely formed by oxidation of CO even at low temperature (-100 °C) on V_2O_5, giving rise to reduced V species. On the reduced VO_x sample a weak broad CO peak at 2204 cm^{-1} could be observed. This peak was even weaker on the oxidized sample and had a maximum at slightly lower frequencies. Due to the low intensity, a more precise designation was not reliable. In literature this peak was attributed to CO chemisorbed on V^{4+} species. [53, 54]

Further peaks were visible in the CO stretch vibration region: A peak appeared at 2173 cm^{-1} on the reduced sample, which shifted to 2165 cm^{-1} on the oxidized sample. Another band appeared at 2153 cm^{-1} which was independent of the pretreatment. In literature it was argued about the assignment of CO stretch vibrations on vanadium below 2180 cm^{-1}. Bands in the range from 2180 – 2150 cm^{-1} were either attributed to CO adsorbed on V^{3+} sites or to CO interacting with hydroxyl groups on the vanadium oxide surface. [51, 53-56] An even lower oxidation state of vanadium than V^{3+} seemed unlikely. Unfortunately, a change of OH-vibrations due to CO adsorption could not be detected, because of the low transmittance in the frequency range beyond 3000 cm^{-1} for V_2O_5 samples. Finally, in accordance with literature [51] the band at 2153 cm^{-1} was assigned to V^{3+} sites, as this band did not show a shift after different pretreatments of the sample. Consequently, the band around 2170 cm^{-1} was assigned to CO on hydroxyl groups, as suggested in literature [53, 54]. Another hint supporting this assignment concerned the intensities of the bands: It can be assumed that the pretreatment temperature of 250 °C was too low for a reduction of pure V_2O_5, because the bands of the overtones of the V=O stretch vibration at around 2000 cm^{-1}, typical of fully oxidized V_2O_5, did not disappear in the background spectrum after reduction. As a consequence V^{3+} sites were neither present on the sample after reduction nor after

oxidation, but only formed by the oxidation of CO. Therefore, the intensity of the band for CO on V^{3+} was the same for the reduced and oxidized sample, as displayed in figure 4.18 b). In contrast, the amount of hydroxyl groups on the surface was likely increased during reduction in hydrogen, entailing an increasing intensity of the band of CO interacting with OH a 2170 cm^{-1}. Also the shift could be explained by the higher coverage of the surface with hydroxyl groups.

Finally, a shoulder at 2140 cm^{-1} was detected, which is typical of physisorbed CO. [53, 54]

The Pd-V_2O_5 sample in its reduced form showed the strongest CO absorption bands. In presence of CO gas phase a large, narrow peak was detected at 2147 cm^{-1}, which almost completely vanished upon evacuation, but did not shift in frequency. Furthermore, two broad bands at 2094 and 1983 cm^{-1} were detected in 5 mbar CO. These two bands shifted a little bit to lower frequencies (2070 and 1979 cm^{-1}) upon evacuation accompanied by a decrease in intensity. The band at 2094 cm^{-1} respectively 2070 cm^{-1} was assigned to CO adsorbed on-top of Pd. The band at 1983 respectively 1979 cm^{-1} was attributed to CO on bridging adsorption sites on Pd. The assignment of the intense peak at 2147 cm^{-1} to CO bound to V^{3+}, equivalent to the band at 2153 cm^{-1} on the pure V_2O_5, was corroborated by the absence of the overtone vibrations of V=O after reduction which revealed that the reduction temperature of V_2O_5 is lowered by the addition of Pd.

The oxidized Pd-V_2O_5 sample could not be reliably analyzed for absorption of CO on Pd, because of the overtones arising from vanadyl groups, which overlapped with absorption peaks in the relevant range.

The relevant CO adsorption spectra are visualized in figure 4.18.

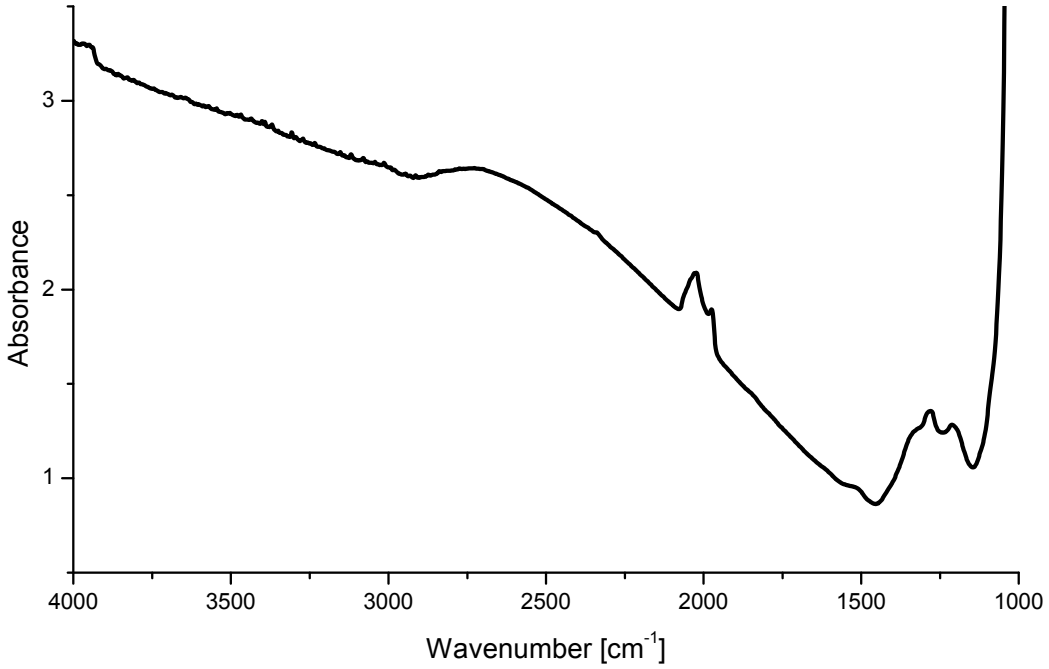

Figure 4.17: IR-spectrum of oxidized V_2O_5 at 30 °C in vacuum.

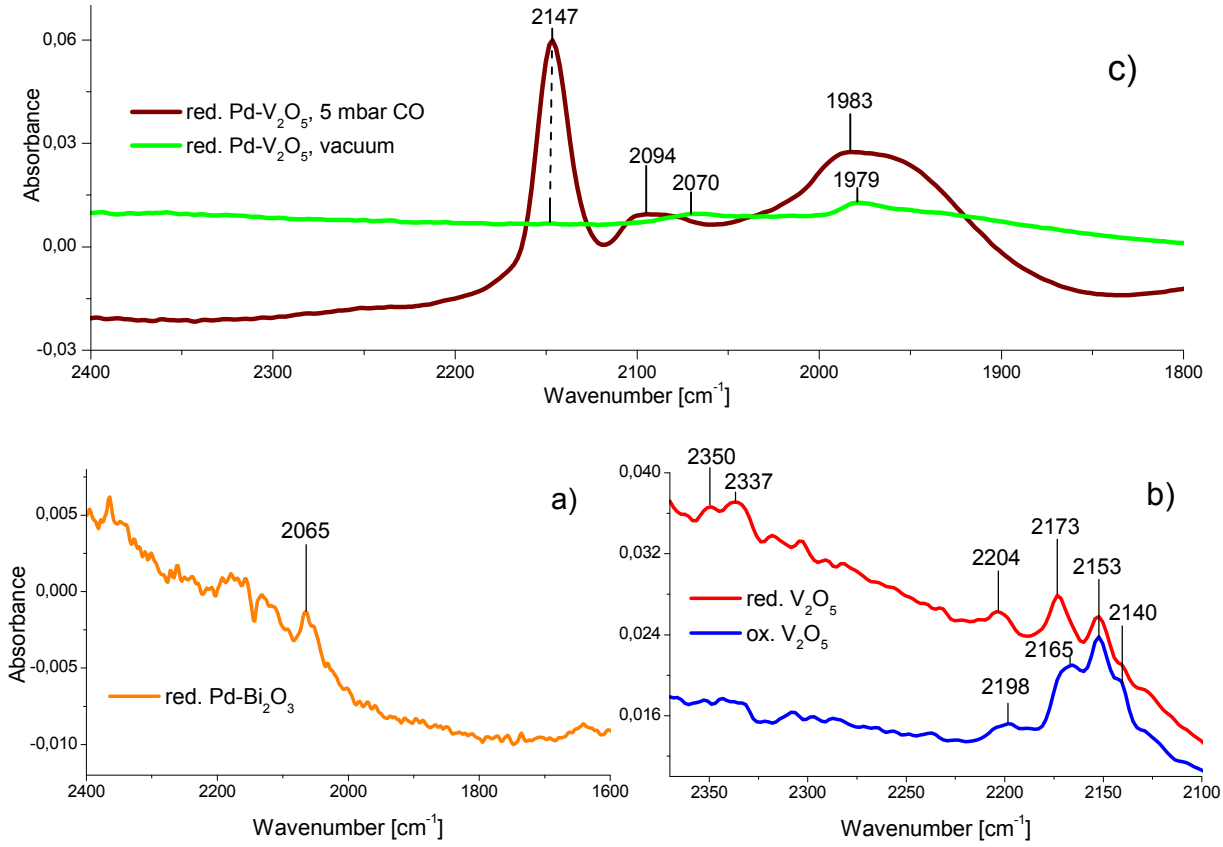

Figure 4.18: IR-spectra of CO adsorbed at -110 °C on different samples in CO atmosphere followed by evacuation: a) reduced Pd-Bi_2O_3 in 5 mbar CO; b) oxidized respectively reduced V_2O_5, each spectrum in 5 mbar CO; c) reduced Pd-V_2O_5 in 5 mbar CO and after evacuation.

4.3.2 Methanol Adsorption

Adsorption studies of methanol on Bi_2O_3 revealed that methanol was adsorbed both in an undissociated form and as methoxy. The observed bands, listed and assigned to respective vibration modes in table 4.3, were in good agreement with data from literature [57]. All bands were stable upon evacuation and heating in vacuum up to 250 °C. The same bands were observed on the reduced and oxidized sample. Figure 4.19 displays the IR spectra of methanol adsorbed on the reduced and oxidized Bi_2O_3 sample at room temperature.

Table 4.3: Recorded bands of methanol adsorption on the pure metal oxides (Bi_2O_3 and V_2O_5) and their assignment to undissociated methanol (I) and methoxy species (II) on the surface in good accordance with literature [57, 58].

catalyst	**$\nu_s(CH_3)$** **II**	**$2\delta_{as}(CH_3)$**	**$2\delta_s(CH_3)$**		**I**	**I**	**$\delta_{as}(CH_3)$**	**$\delta_s(CH_3)$**	**δ(OH)** **I**	**$r(CH_3)$**	**$\nu_s(CO)$**
Bi_2O_3	2906	2855	2787	2055	2030[s]		1460[s]	1440	1390		1046
V_2O_5	2923		2825				1445	1431		1150	1058

[s]shoulder; $2\delta_s$, $2\delta_{as}$ describe the first overtone of the symmetric respectively asymmetric deformation mode.

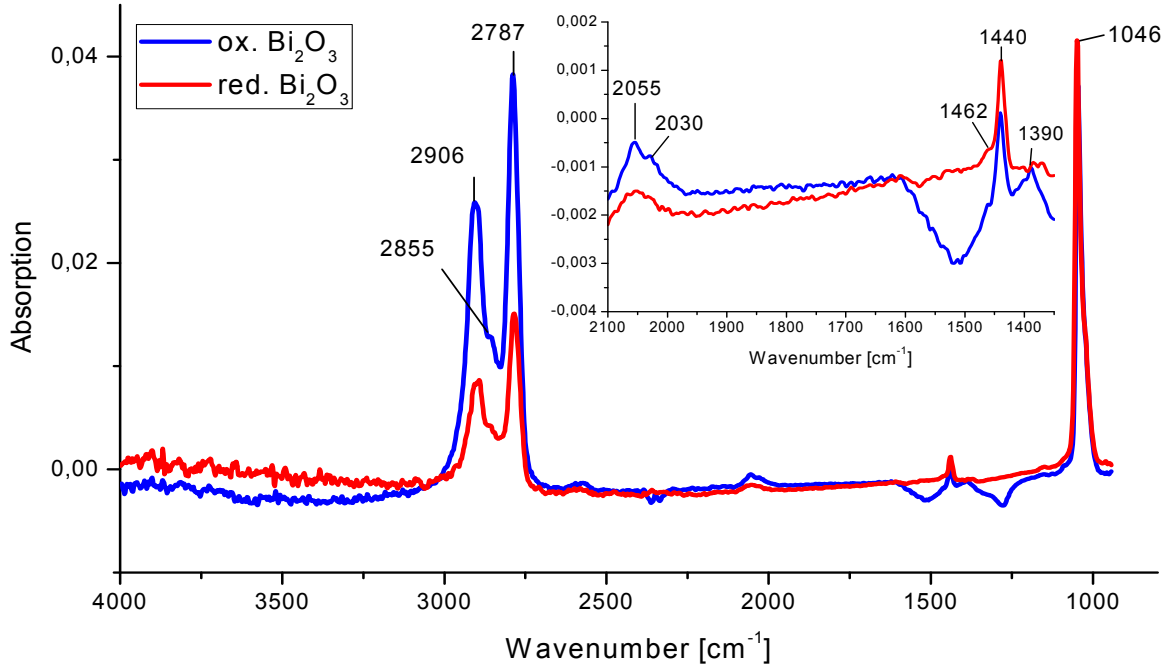

Figure 4.19: Methanol (0.5 mbar) adsorbed to Bi_2O_3 at 30°C, followed by evacuation after reduction or oxidation.

The adsorption of methanol on the Pd-Bi_2O_3 sample turned out to be especially instructive. For both the oxidized and the reduced sample the same results were obtained, however, the quality of the spectra of the reduced sample was better, which made an evaluation easier. At room temperature several bands in the range of about 3600 cm^{-1}, characteristic of O-H stretching vibrations, and in the range of ~2900 cm^{-1}, characteristic of C-H stretching vibrations, were observed, which were similar to IR bands of pure MeOH in the gas phase. Since these bands were stable upon evacuation at 30 °C, they were attributed to undissociated methanol adsorbed at the surface. In addition to the peaks of undissociated methanol methoxy species or other product molecules, absorbing in this range, could be hidden underneath the broad absorption bands. As on pure Bi_2O_3 two bands at 1440 and 1043 cm^{-1} were assigned to methoxy species on the surface. However, undissociated methanol seemed to absorb at the same frequencies, so that a contribution of both forms of MeOH to the two bands was likely.

Moreover, new peaks were observed at 1652, 1547, 1346, 1227 and 1165 cm^{-1}. Comparing these bands with infrared adsorption studies of methanol on different metal oxide and metal catalysts in literature ([50, 58-64]) it was concluded that the bands at 1654 and 1545 cm^{-1} could be assigned to the asymmetric stretching vibration of formate species adsorbed in different geometries. The band at 1346 cm^{-1} therefore corresponded to the symmetric

stretching vibration of the HCOO species. The two bands at 1227 and 1162 cm^{-1} were attributed to DME that had formed on the surface upon adsorption and dehydration of methanol.

A temperature ramp in vacuum revealed a change in the spectrum with increasing temperature. At about 100 °C the undissociated methanol species seemed to have desorbed or transformed to other molecules. One broad peak around 3250 cm^{-1} and the rotational bands around 1600 cm^{-1} gave reason for the assumption that water was formed and desorbed from the surface to the gas phase at these temperatures. In the C-H stretch vibration range distinct peaks were observable at elevated temperatures at 2957, 2920 and 2851 cm^{-1}. A definite assignment of bands in this region was difficult, since many possible molecules formed on the surface had similar vibrations in this region. The presence of methoxy species was confirmed by the bands at 1440 and 1043 cm^{-1}. Compared to the spectrum at room temperature their intensity, however, decreased because of the desorption of undissociated methanol at ~100 °C. A change in intensity of the formate peaks was difficult to determine, because of the rotational lines of water absorbing in this region. The bands for DME completely vanished already at about 50 °C.

Apart from a decrease and disappearance of bands when elevating the temperature, two new bands were detected at 1462 cm^{-1} and 1740 cm^{-1}. The band at 1462 cm^{-1} coincided with the asymmetrical deformation vibration of methoxy adsorbed on the Bi_2O_3 sample. It could be assumed that the large amount of undissociated methanol adsorbed at 30 °C simply masked this small peak at that temperature. The band at 1740 cm^{-1}, however, seemed to form only upon heating, as it still grew with increasing temperature. According to literature [65] this band was attributed to formaldehyde forming on V_2O_5 or Pd by dehydrogenation of methanol or methoxy.

At higher temperatures (up to 250 °C) the rotational bands of water disappeared again and the intensity of the OH stretch bands of water at ~3250 cm^{-1} decreased as well. In the absence of the rotational bands, it was possible to detect a decrease of formate species. At higher temperatures (>200 °C) this peak also shifted from 1545 to 1540 cm^{-1}. Furthermore, a decrease of methoxy bands with increasing temperature was observed. Only the peak for formaldehyde increased with temperature, as already stated above, and shifted from 1740 cm^{-1} at about 100 °C to 1743 cm^{-1} at ~200 °C.

Figure 4.20 visualizes the changes in the IR spectra of adsorbed methanol on Pd-Bi_2O_3 with increasing temperature.

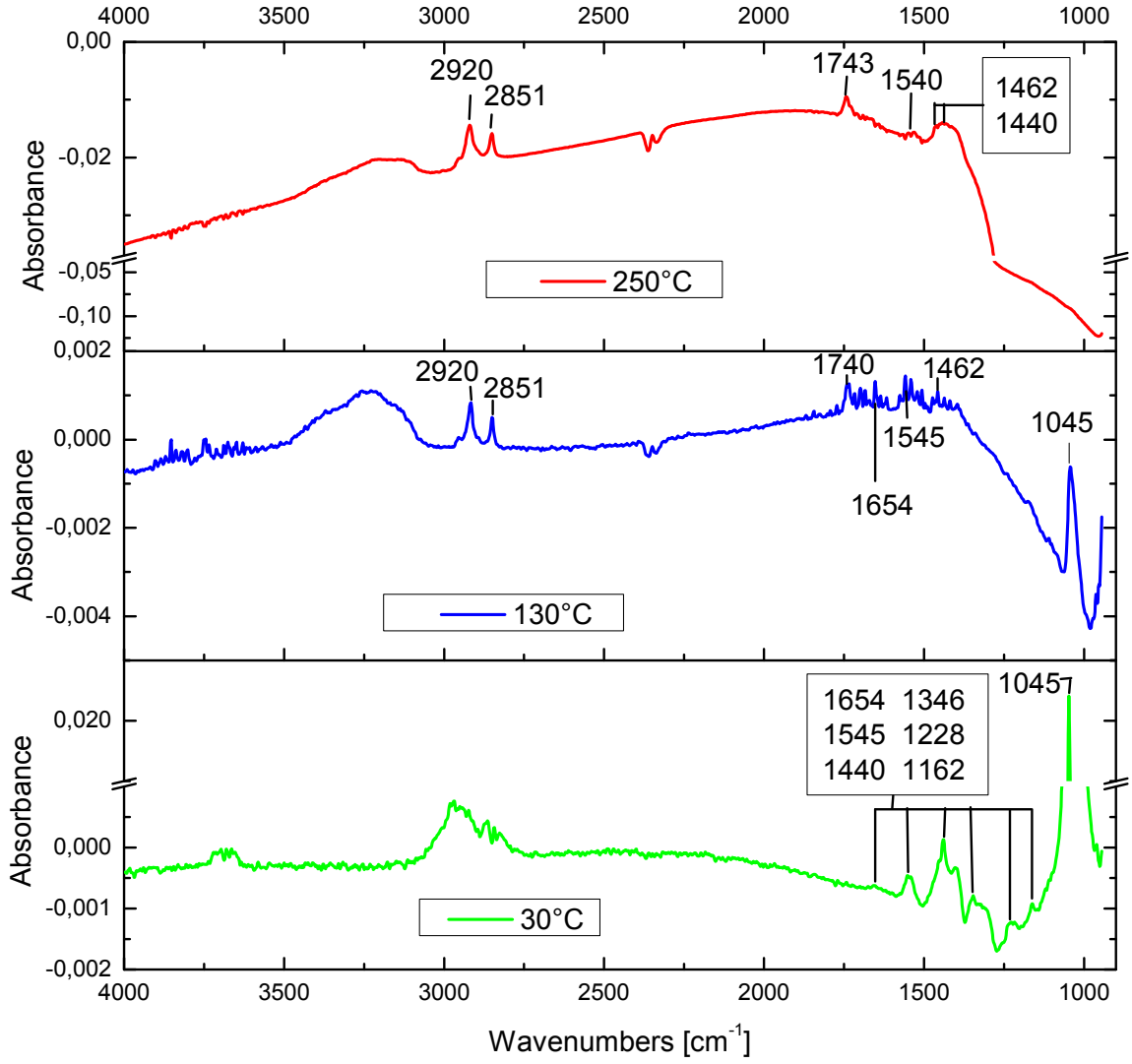

Figure 4.20: IR spectra of methanol adsorption on red. Pd-Bi_2O_3 followed by evacuation at 30 °C and after heating to 130 °C and 250 °C.

On pure vanadium oxide only methoxy species were detected. The band positions and their assignment are displayed in table 4.3; the detected bands were in accordance with references [58] and [57]. Most bands of methanol adsorbed on the oxidized or reduced sample were the same; however, on the reduced V_2O_5 sample bands in the C-H stretching region were not visible properly: The spectrum of the reduced V_2O_5 in the spectral region above ~2600 cm^{-1} was pretty noisy due to the low transmittance of the much darker sample after reduction. The C-O stretching band of methoxy at 1058 cm^{-1} on the oxidized sample was shifted to 1049 cm^{-1} on reduced V_2O_5. The methoxy species were stable upon evacuation at room temperature and with rising temperature in vacuum up to 50 °C. In

figure 4.21 the spectra of methanol adsorbed on oxidized and reduced V_2O_5 at 30 °C are shown.

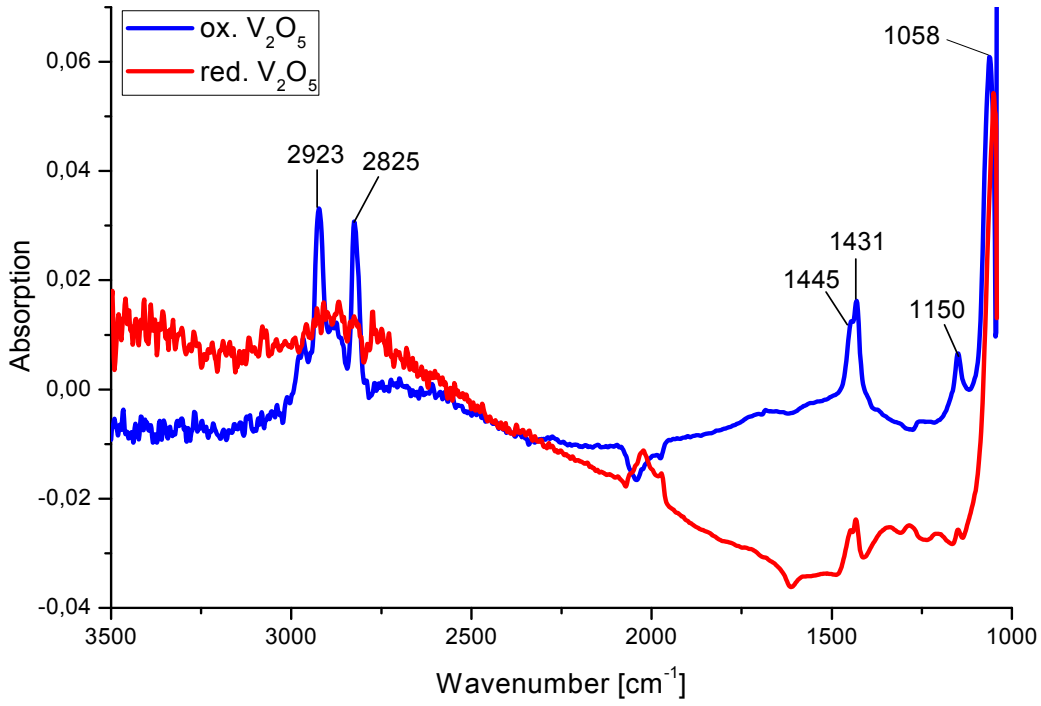

Figure 4.21: IR spectra of methanol adsorbed on reduced or oxidized V_2O_5 (0.5 mbar MeOH) at 30 °C followed by evacuation.

The oxidized Pd-V_2O_5 sample showed similar features as the pure V_2O_5 sample. Methoxy species could be detected at the same frequencies as on V_2O_5: 2923, 2825, 1446, 1432, 1150 and 1058 cm^{-1}. In addition to the bands of methoxy species, bands at 2960, 2882, 1684 (only at higher temperatures) and 1264 cm^{-1} were detected. Except for the band at 1684 cm^{-1} that showed up only at higher temperatures, all bands decreased with increasing temperature. Comparison with data from literature [58, 66] made an attribution of the bands appearing in addition to the methoxy bands to absorption modes of formaldehyde plausible. Formaldehyde is able to adsorb as a molecule on the surface as well as to polymerize on the catalyst. While the band at 1684 cm^{-1} was assigned to the C=O stretch vibration of the adsorbed formaldehyde molecule, the other bands likely corresponded to the polymer.

Like on the reduced pure V_2O_5 also the Pd-V_2O_5 sample did not allow a detailed study in the C-H stretch vibration range after reduction. Only a noisy broad peak could be observed, likely caused by the low transmission of the catalyst. A small peak at 2826 cm^{-1} could be assigned to adsorbed methoxy species. The shift of the band at 1058 cm^{-1} on the oxidized sample to 1049 cm^{-1} on the reduced Pd-V_2O_5 reminded of the pure metal oxide. Both the

bands at 1049 cm^{-1} and at 1446 cm^{-1} could be attributed to methoxy species. Further absorption features could not be clearly identified and may rather be caused by the background.

Figure 4.22 displays the spectra of methanol adsorbed on the reduced and oxidized Pd-V_2O_5 sample at 30 °C followed by evacuation.

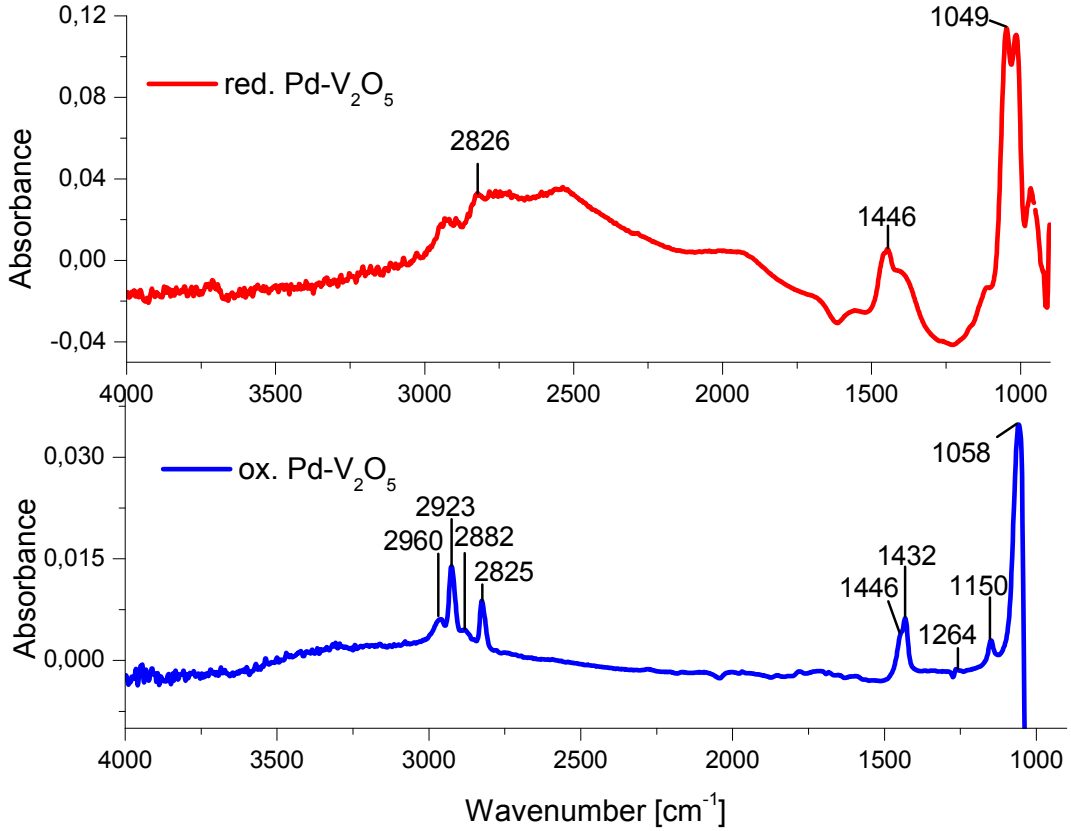

Figure 4.22: IR spectra of methanol (0.5mbar) adsorbed to oxidized and reduced Pd-V_2O_5 at 30 °C followed by evacuation.

4.3.3 In-situ Studies During Methanol Oxidation Reaction

Finally, in situ IR spectroscopy was performed under methanol oxidation conditions. The in-situ studies turned out to be difficult to evaluate, because of the higher partial pressure of reactant and product molecules in the gas phase. The best spectra of adsorbed species were obtained at 100 °C reaction temperature. Apart from the bands of methanol in the gas phase with characteristic features around 3600 cm^{-1}, below 3000 cm^{-1} and around 1033 cm^{-1} a well-defined, intense band was observed at 1559 cm^{-1} on the reduced Pd-Bi_2O_3. This band was assigned to MFA, which was the only product formed at this temperature according to GC measurements

On the oxidized Pd-V_2O_5 sample, again methanol vapor was visible. However, a rather large peak was detected at 1607 cm^{-1}, which could be assigned to water adsorbed on V_2O_5. [67] Further peaks at 1454, 1435 and 1146 cm^{-1} fit to the methoxy bands observed in the methanol adsorption studies; the band at 1347 cm^{-1}, however, could not be assigned up to now.

Finally, the spectra of the hybrid sample Pd-Bi_2O_3-CNT provided a means to identify, which products formed during the methanol oxidation reaction. Although no adsorbed species were visible in the spectrum, a mixture of all gas products present in the reaction chamber was detected: CO_2 was observed at around 2350 cm^{-1}, MFA had spectral features around 1750 cm^{-1} and around 1200 cm^{-1}; DME could contribute to the bands around 1200 cm^{-1} as well. Moreover, the rotational bands of water, visible around 1600 cm^{-1}, and unconverted methanol with characteristic bands as described above were detected in the spectrum.

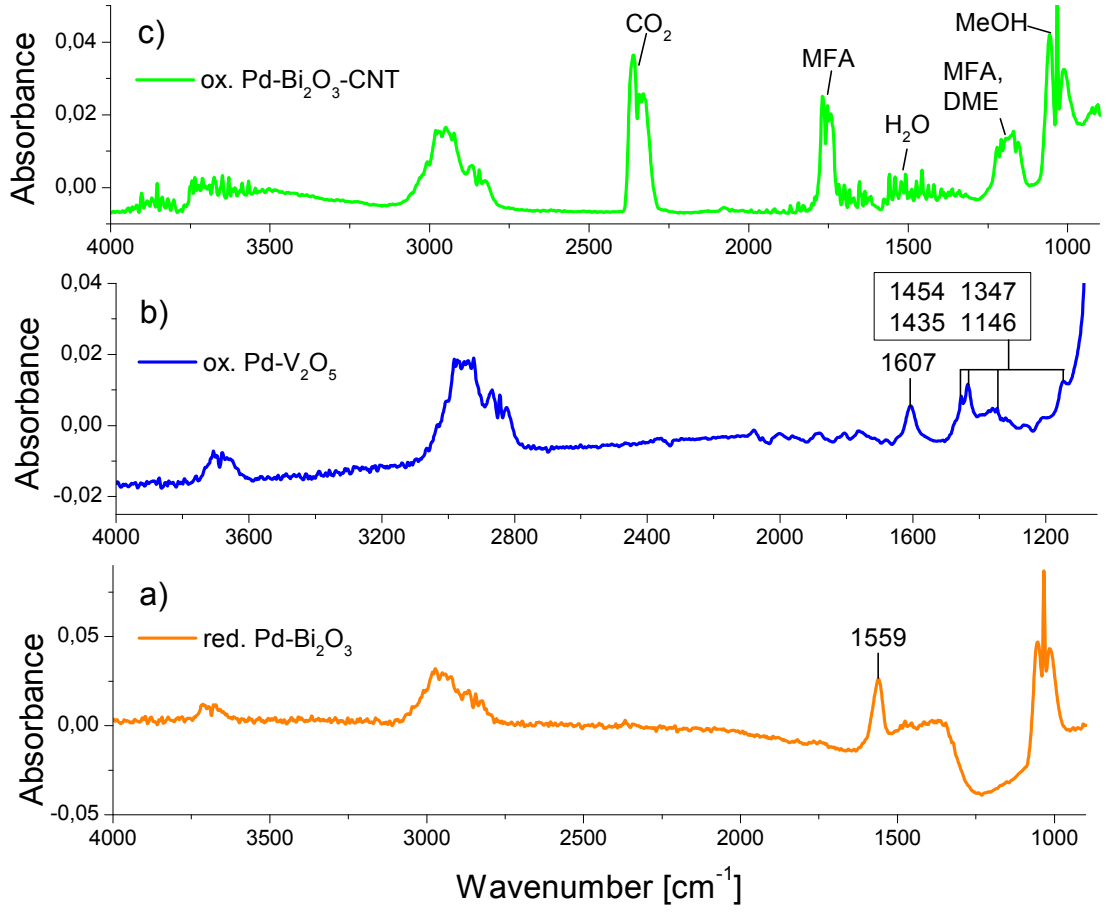

Figure 4.23: In-situ IR spectra of methanol oxidation (2 % MeOH and 2 % O_2 in He at a total flow of 50 ml/min) at 100 °C on a) red. Pd-Bi_2O_3, b) ox. Pd-V_2O_5 and c) Pd-Bi_2O_3-CNT.

4.4 Kinetic Studies

For the evaluation of the kinetic studies relevant kinetic parameters were calculated:

For a better comparability and in order to reduce the influence of variations of the gas chromatograph detection systems and the mass flow controllers, the calculations were based on a carbon balance (ΣC). This balance was calculated by summing up all carbon atoms measured in one chromatogram.

$$\Sigma C = \Sigma(i_x * n_x) \qquad \text{equation 7}$$

ΣC: carbon balance [mol]

x: nature of molecule

i_x: number of carbon atoms in molecule x

n_x: amount of molecule x [mol]

For example, in measurements with Bi_2O_3 containing catalysts 5 different molecules were detected in the product flow: CO, CO_2, DME, MeOH and MFA. In this case the carbon balance was calculated as followed:

$$\Sigma C = n_{CO} + n_{CO_2} + 2 * n_{DME} + n_{MeOH} + 2 * n_{MFA} \qquad \textbf{equation 8}$$

Consequently, the total conversion could be calculated according to equation 9:

$$conversion = 1 - \frac{n_{MeOH}}{\Sigma C} \qquad \textbf{equation 9}$$

The calculation of the yield for each formed product was based on the carbon balance as well:

$$yield(X) = \frac{i_X * n_X}{\Sigma C} \qquad \text{equation 10}$$

X: product molecule

The selectivity for each formed product was calculated excluding the reactant methanol:

$$selectivity(X) = \frac{i_X * n_X}{\Sigma C - n_{MeOH}} \qquad \textbf{equation 11}$$

Furthermore, the total reaction rate and the product formation rates were evaluated, whose computations were based on the feed flow. The feed flow in mol/s was approximated with the help of the general gas equation:

$$f_{feed} = \frac{f_{total} * p_{MeOH}}{R * T}$$ equation 12

f_{feed}: feed flow [mol/s]

f_{total}: total flow [m^3/s]

p_{MeOH}: partial pressure of methanol at the temperature in the saturator[Pa]

R: universal gas constant = 8.314 J/(mol*K)

T: temperature of the inlet system = 423.15 K

Finally, for the calculation of the reaction and formation rates on a catalyst, the rate was related to the amount of the catalyst used for the reaction.

$$r = \frac{f_{feed} * conversion}{m_{cat}}$$ equation 13

r: total reaction rate [mol/(g*s)]

m: mass of catalyst [g]

$$r_{p.f.} = \frac{f_{feed} * yield}{m_{cat}}$$ equation 14

$r_{p.f.}$: product formation rate [mol/(g*s)]

The investigated catalysts turned out to be highly active with conversion levels ranging from 50 – 98 %. Employment of even higher flow rates and smaller amounts of catalyst did not sufficiently reduce the conversion levels. Since for calculations of kinetic parameters such as activation energy and reaction order, conversion levels of about 10 % or less are needed in order to guarantee that the reactions are not limited by diffusion, these parameters could not be determined.

4.4.1 Bi_2O_3 Containing Samples

Both in the reference sample and in the hybrid sample the only observed products in a temperature range from 40 to 250 °C were CO_2, MFA and DME. DME, however, was only formed at higher temperatures (>100 °C) and up to 250 °C the selectivity for DME did not exceed 5 %. The selectivity towards the main products MFA and CO_2 depended on the temperature. At lower temperatures and conversion levels the formation of MFA was favored, while the selectivity to CO_2 rose with increasing temperature and conversion.

Although different pretreatment conditions were tested to achieve a stable catalytic performance of the reference Pd-Bi_2O_3 right after the respective pretreatment, a gradual deactivation of the catalyst with every reaction cycle was always observed. The different results for the selectivity were also connected to the decreasing conversion levels. (see figure 4.24) Additionally, even the use of a fresh catalyst for every run performed under the same conditions did not lead to reproducible results: Sometimes conversion levels of >90 % were calculated, for other runs with the same fresh catalyst conversion levels of only about 50 % were observed. These results would give reason to assume an inhomogeneous distribution of Pd in the sample, which could not be confirmed by other techniques.

The influence of the pretreatment atmosphere on the catalytic performance could not be assessed, because of the irreproducible results in both cases.

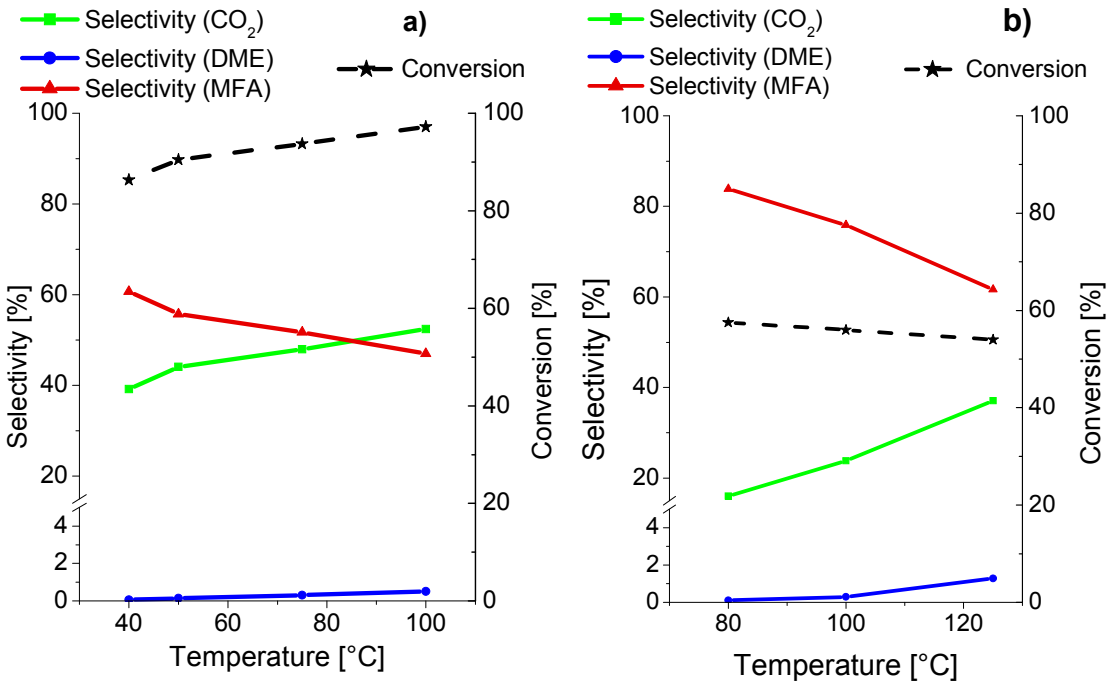

Figure 4.24: Methanol oxidation at a total flow of 50 ml/min over oxidized Pd-Bi_2O_3. a) first run, b) second run under the same conditions.

On the contrary, Pd-Bi_2O_3-CNT seemed to be more stable and provided reproducible results. The results obtained after an oxidizing pretreatment did not significantly differ from those after reduction. In figure 4.25 the change of the selectivity in favor of CO_2 with increasing temperature is displayed. Moreover, this figure shows the influence of different total gas flows: 4 different total flows were tested; though the difference between a total flow of 25 ml/min and 50 ml/min respectively 75 ml/min and 100 ml/min was marginal, a distinct

difference between the total flow of 50 ml/min (25 ml/min) and 100 ml/min (75 ml/min) was observed. First, when comparing the conversion levels at the same temperature, a lower conversion was measured at higher flow rates. This effect was considerably stronger at lower temperatures. Second, a higher selectivity to MFA was observed at higher temperatures when applying a higher flow rate. Both observed effects are reasonable, since higher flow rates result in shorter residence time of the reactants in the catalyst bed. Therefore, the achieved conversion level and the further oxidation of MFA to CO_2 are both significantly reduced. At higher temperatures the reaction rate was higher as well, so that the influence of the total flow on the conversion level and selectivity was lower at higher temperatures.

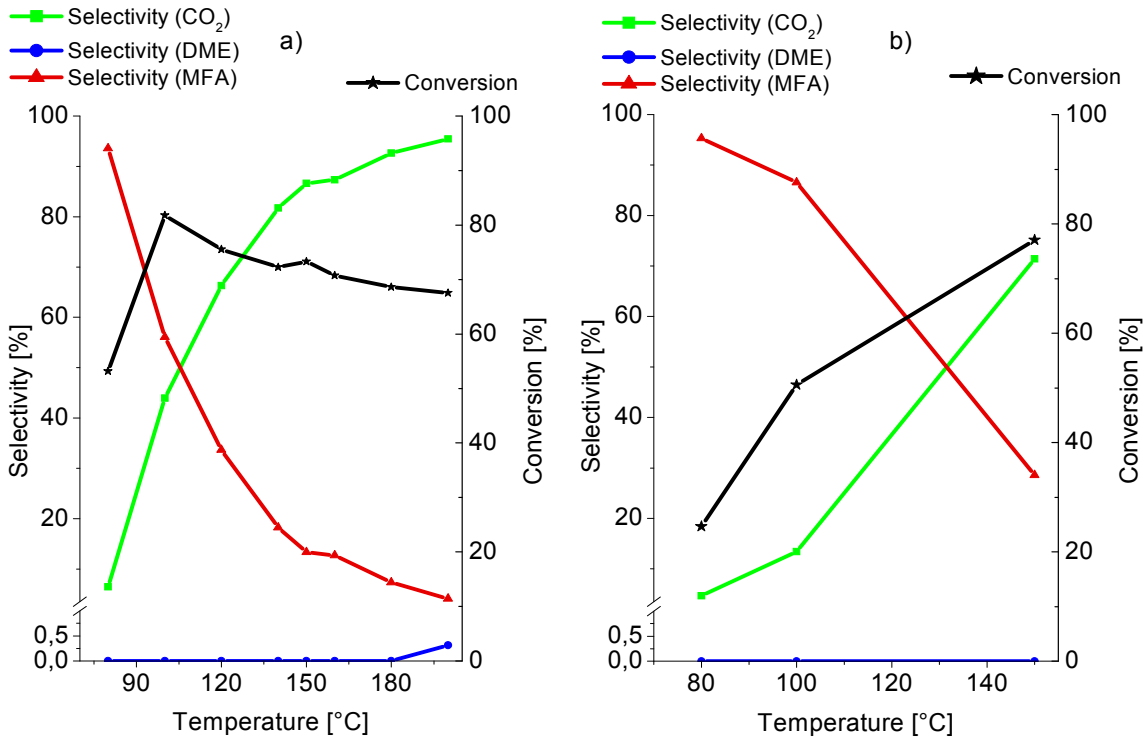

Figure 4.25: Methanol oxidation over ox. Pd-Bi_2O_3-CNT with 2 % MeOH and 2 % oxygen in helium at a total flow of a) 50 ml/min and b) 100 ml/min

Calculated kinetic parameters for the Pd-Bi_2O_3-CNT hybrid catalyst are listed in table 4.4.

Table 4.4 (a): Kinetic parameters for the methanol oxidation over Pd-Bi_2O_3-CNT. The catalyst was pretreated under oxidizing conditions at 250 °C; the reaction mixture was 2 % MeOH and 2 % O_2 in He as a carrier gas. The total flow was kept constant at 50 ml/min, while the temperature was varied.

Total Flow [ml/min]		**50**							
Temperature [°C]		**80**	**100**	**120**	**140**	**150**	**160**	**180**	**200**
Conversion [%]		53	82	76	72	73	71	69	68
Yield [%]	CO_2	3	35	50	59	64	62	64	64
	DME	0	0	0	0	0	0	0	0
	MFA	50	47	25	13	10	9	5	3
Selectivity [%]	CO_2	6	43	66	82	87	87	93	95
	DME	0	0	0	0	0	0	0	0
	MFA	94	57	34	18	13	13	7	4
Reaction Rate $*10^5$ [mol/(s*g)]		3.60	5.56	5.12	4.90	4.97	4.79	4.65	4.57
Product Formation Rate $*10^5$ [mol/(s*g)]	CO_2	0.23	2.38	3.40	4.00	4.30	4.19	4.31	4.37
	DME	0.00	0.00	0.00	0.00	0.00	0.00	0.00	0.01
	MFA	3.37	3.19	1.72	0.89	0.66	0.61	0.34	0.19

Table 4.4 b): Kinetic parameters for varying total flows and temperatures over the same catalyst, pretreatment and reaction mixture as in table 4.4 (a) (methanol oxidation over ox. Pd-Bi_2O_3-CNT with 2 % MeOH and 2 % O_2 in He).

Total Flow [ml/min]		**25**			**75**			**100**		
Temperature [°C]		**80**	**100**	**150**	**80**	**100**	**150**	**80**	**100**	**150**
Conversion [%]		82	77	63	33	53	73	24	51	77
Yield [%]	CO_2	21	42	58	2	8	54	1	7	57
	DME	0	0	0	0	0	0	0	0	0
	MFA	61	35	5	31	45	18	23	44	20
Selectivity [%]	CO_2	26	54	92	6	15	75	5	13	74
	DME	0	0	0	0	0	0	0	0	0
	MFA	74	46	8	94	85	25	95	87	26
Reaction Rate $*10^5$ [mol/(s*g)]		2.76	2.60	2.12	3.33	5.39	7.36	3.30	6.83	10.44
Product Formation Rate $*10^5$ [mol/(s*g)]	CO_2	0.71	1.41	1.95	0.20	0.83	5.49	0.16	0.92	7.71
	DME	0.00	0.00	0.00	0.00	0.00	0.00	0.00	0.00	0.00
	MFA	2.05	1.18	0.17	3.13	4.56	1.87	3.15	5.92	2.72

4.4.2 V_2O_5 Containing Samples

V_2O_5 containing catalysts were capable of forming formaldehyde in addition to CO_2, MFA and DME. Furthermore, small amounts of CO were registered. Nevertheless, the main products were also on these samples MFA and CO_2. Only at low conversion levels (<10 %) a higher selectivity towards formaldehyde (maximum 20 %) was observed. Moreover, formaldehyde was formed at the beginning of the reaction and its amount decreased with time.

Comparing the selectivities on V_2O_5 catalysts, a similar picture was found as for the Bi_2O_3 containing catalysts: At lower temperatures (100 °C) a high selectivity (~90 %) to MFA was observable. If the reaction was performed at higher temperatures, the selectivity changed more and more in favor of CO_2.

When comparing the V_2O_5 containing catalysts with the Bi_2O_3 containing samples, catalysts with V_2O_5 were active only at higher temperatures, which is in agreement with TPReaction measurements. An interesting observation concerned the temperature at which catalyst activity set in. The Bi_2O_3 catalysts were always active already at room temperature and never completely deactivated; V_2O_5 containing catalysts, however, were active only at around 100 °C, even if a fresh catalyst was used.

Fresh catalysts (both reference Pd-V_2O_5 and hybrid Pd-V_2O_5-CNT) were very active with conversions above 80 %. When the same catalyst was used several times to test its activity at different temperatures with pretreatment steps at 250 °C in-between the kinetic measurements, a continuous decrease of the total conversion of the catalyst and finally a complete deactivation after several cycles was observed. Neither application of higher reaction temperatures (up to 200 °C), nor oxidizing or reducing pretreatments were successful in reactivating the catalysts. Within one isothermal reaction cycle, however, the conversion was stable with time on stream.

For the reference catalyst Pd-V_2O_5 one could distinguish the oxidized or the reduced state by its color: Oxidized Pd-V_2O_5 was ochre-yellow, while its reduced form was dark brown. Though the catalyst had a dark brown color straight after reaction, where it had been active, reducing pretreatments were even more disadvantageous for activity than oxidation.

A potential deactivation of the catalyst under reaction conditions was tested by long-term experiments with a duration time of about 14 hours. An ox. Pd-V_2O_5-CNT sample was pretreated at 250 °C in synthetic air for 30 min; afterwards methanol oxidation was performed at 100 °C. The catalyst was highly active at that temperature and the conversion did not decrease over the whole reaction time. The same experiment was performed with the same catalyst at 125 °C and 150 °C reaction temperatures. In all three experiments no deactivation could be observed. Therefore, it was concluded that under methanol oxidation conditions the catalyst did not deactivate by side reactions. Figure 4.26 displays the long-term measurements.

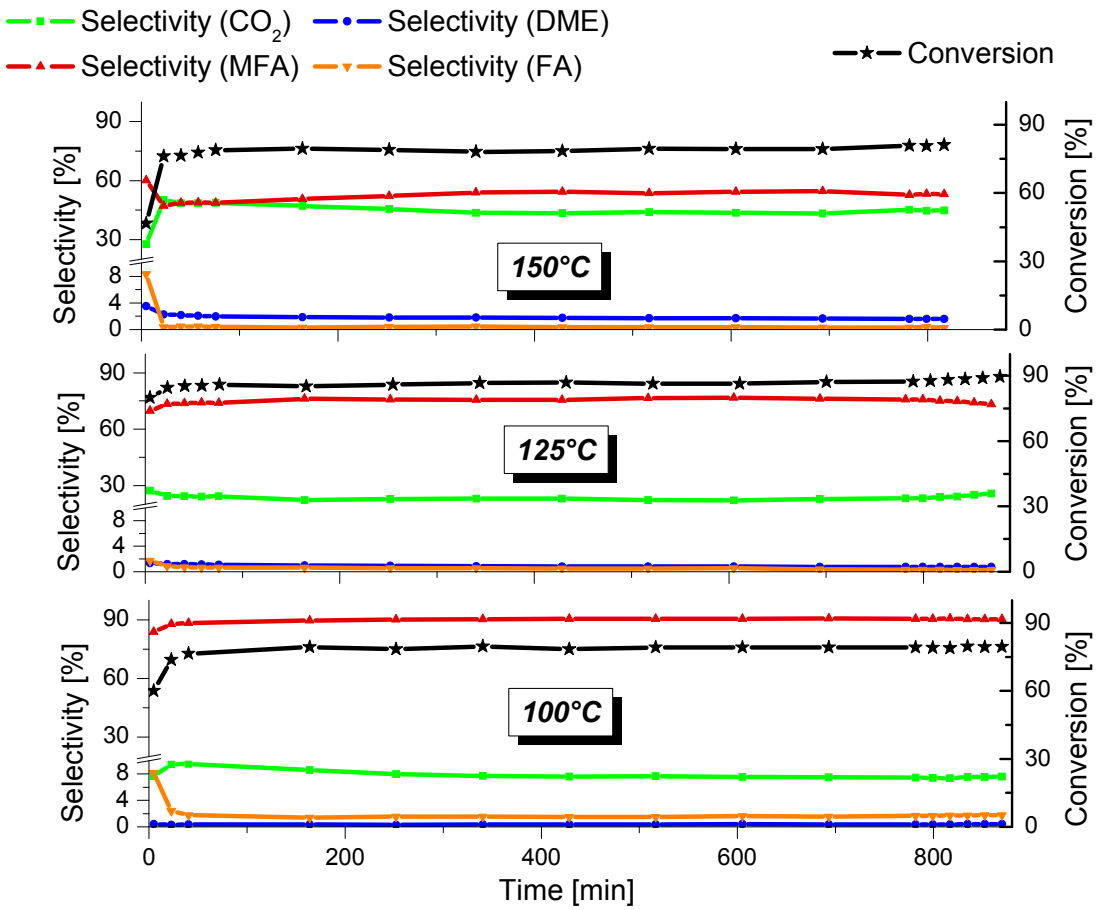

Figure 4.26: Methanol oxidation over ox. Pd-V_2O_5-CNT at a total flow of 50 ml/min at 100 °C, 125 °C and 150 °C.

Due to the stable performance of the catalysts in long-term measurements, but deactivation upon several pretreatment cycles at 250 °C, it seemed likely that the oxidation state of the catalyst was more and more altered during each pretreatment toward an inactive oxidation state. Another possible explanation for the deactivation based on a successive dehydroxylation of the catalyst surface with each pretreatment. Also a combination of these two variants would be imaginable.

Another observation, made only with V_2O_5 containing catalysts (both reference Pd-V_2O_5 and Pd-V_2O_5-CNT hybrid) was the formation of a yellow oily substance, condensing in the cold part of the glass reactor underneath the catalyst bed. Since formaldehyde is known for polymerization and V_2O_5 is able to catalyze polymerization reactions, a deactivation due to a polymer film on the catalyst surface blocking the active sites would be another possible explanation. However, oxidizing an inactive reference catalyst (which does not contain CNTs) at 500 °C, which should be a sufficiently high temperature to burn such a polymer, did not

reactivate the catalyst. As a consequence the yellow oil formation may only be the result of catalyst deactivation, but not the origin.

In studies on the application of vanadium based catalysts in partial oxidation reactions, it was suggested that addition of a small amount of water is necessary to stabilize vanadium in its active oxidation state, which is proposed to be V^{4+} or V^{3+}. [68, 69] The influence of water addition to the reaction system and in the pretreatment steps would be a possibility to stabilize the active oxidation state of the catalyst and to determine reliable kinetic parameters for V_2O_5 containing catalysts.

4.4.3 Temperature Difference Measurements

Temperature difference measurements were performed at 3 different temperatures for Bi_2O_3 containing samples: 80 °C, 100 °C and 125 °C. As expected the thermocouple, which was positioned close to the catalyst bed registered an increase of the temperature when the reaction was started, while the thermocouple further above regulated the oven at a constant temperature. It was supposed that the distance between the oven regulating thermocouple and the catalyst was big enough, so that it was not influenced by the reaction heat. The results of the measurements with the Bi_2O_3 containing samples are listed in table 4.5. At all chosen temperatures the temperature difference between oven temperature and temperature above the catalyst was bigger for the hybrid sample. One could interpret this fact in a way that the heat was better transferred and distributed to the quartz wool, due to the excellent heat conduction of the nanotubes. However, one has to keep in mind the different conversion and selectivity of the reference sample compared to the hybrid sample. Although the conversion was about the same, big differences have been registered for the selectivity. The hybrid sample was much more selective to CO_2 than the reference sample. The second detected product was in all cases only MFA. Comparing the exothermicity of the two reactions, one can easily find out that the conversion to CO_2 has a distinctly higher reaction enthalpy. Since it was impossible to obtain the same conversion and selectivity on both catalysts at the same temperature, it was difficult to assess the effect of the CNTs in the samples from the obtained data. The heat released was mainly governed by the conversion and the selectivity.

Table 4.5: Temperature difference measurements on the ox. Pd-Bi_2O_3 and ox. Pd-Bi_2O_3-CNT samples. The total flow was in all cases 100 ml/min.

Oven Temperature	Sample	ΔT [°C]	Conversion [%]	Selectivity [%] (CO_2)	(MFA)
80 °C	Pd-Bi_2O_3	**8**	67	20	80
	Pd-Bi_2O_3-CNT	**13**	75	50	50
100 °C	Pd-Bi_2O_3	**10**	65	30	70
	Pd-Bi_2O_3-CNT	**18**	77	87	13
125 °C	Pd-Bi_2O_3	**9**	62	40	60
	Pd-Bi_2O_3-CNT	**17**	71	95	5

The influence of the CNTs on the heat management for the V_2O_5 containing samples could only be evaluated at 150 °C. At temperatures below the reference catalyst was not active and prevented comparative studies at lower temperatures. However, the measurement at 150 °C was successful, because the conversion as well as the selectivity of the products was about the same for the reference and the hybrid sample. The registered temperature difference was in both cases 14 °C. (table 4.6) Consequently, it was followed that the setup for the temperature difference measurements was too imprecise to evaluate the effect of the CNTs on the heat management, or that CNTs hardly influence the heat management.

Table 4.6: Temperature difference measurements at the ox. Pd-V_2O_5 and ox. Pd-V_2O_5-CNT samples. The total flow was in all cases 100 ml/min.

Oven Temperature	Sample	ΔT [°C]	Conversion [%]	Selectivity [%] (CO_2)	(MFA)	(DME)
125 °C	Pd-V_2O_5	**-**	<1	-	-	-
	Pd-V_2O_5-CNT	**12**	79	50	50	-
150 °C	Pd-V_2O_5	**14**	70	90	2	6
	Pd-V_2O_5-CNT	**14**	69	85	11	2

The oven temperatures and the temperatures close to the catalyst bed are visualized in figure 4.27. The diagrams exemplify the measurements at 80 °C for the Bi_2O_3 containing samples and the measurements at 150 °C for the V_2O_5 containing samples.

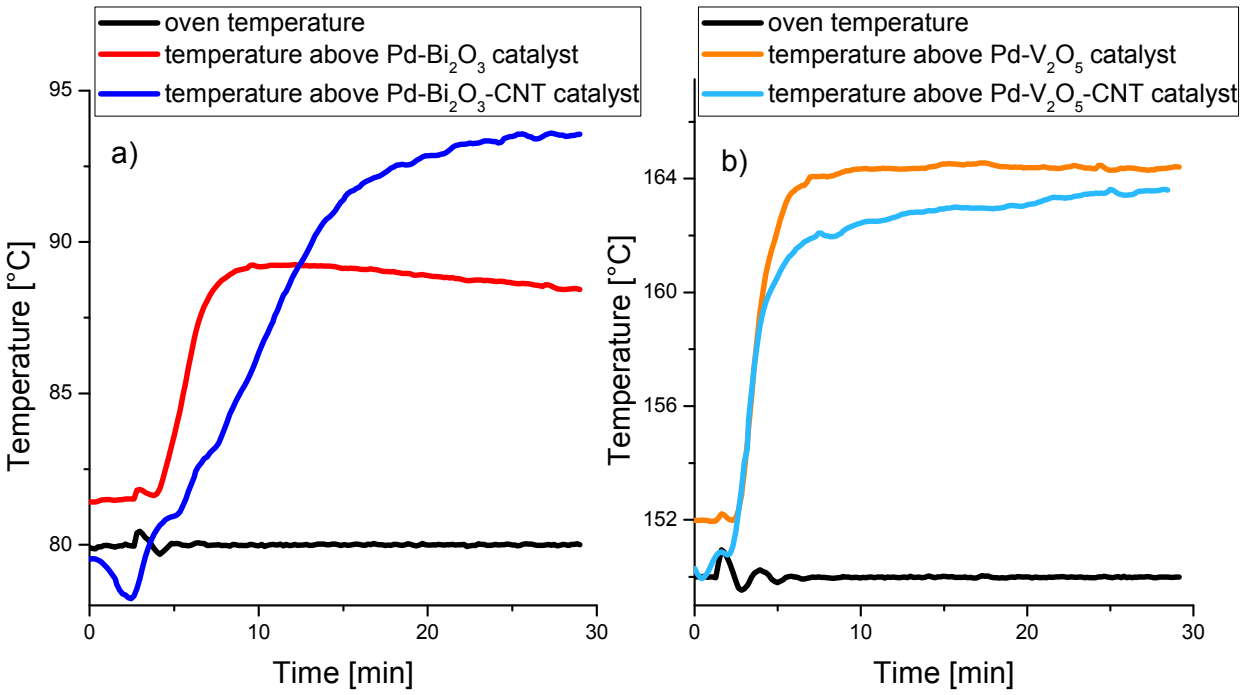

Figure 4.27: Temperature difference measurements on the oxidized reference and hybrid catalysts. a) comparison of the temperatures measured above the Pd-Bi_2O_3 catalyst and the Pd-Bi_2O_3-CNT catalyst at an oven temperature of 80°C, b) comparison of the temperatures measured above the Pd-V_2O_5 catalyst and the Pd-V_2O_5-CNT catalyst at an oven temperature of 150°C.

Though temperature difference measurements could not be used to evaluate the influence of CNTs on the heat management, they showed that the exact position of the thermocouple in the quartz tube, which regulated the oven in the kinetic studies, played a big role. Small variations of the space between thermocouple and sample could entail quite big differences in the real temperature on the catalyst in case of strongly exothermic reactions. This could be another reason for the difficulty in obtaining reproducible results in the kinetic studies.

5 Summary, Conclusions and Outlook

The objective of the thesis was the characterization of metal oxide – carbon nanotube hybrid materials applied as heterogeneous catalysts by adsorption and reactivity studies. Two different systems, based on two different metal oxides (Bi_2O_3 – CNT hybrids and V_2O_5 – CNT hybrids) were chosen and compared to the respective commercial bulk metal oxide powders as references. In order to prevent combustion of the carbon nanotubes (CNTs) during reactivity studies, palladium was added to the samples, which allowed performing the studies at sufficiently low temperatures. The influence of CNTs, which possess a high thermal conductivity, should be assessed by investigation of an exothermal reaction. Therefore, the methanol oxidation was chosen as a test reaction.

CNTs were prepared by a CVD process; subsequently, the metal oxides were synthesized directly on the CNTs by a sol-gel process, which was followed by a calcination step to create a crystalline metal oxide layer. Finally, Pd was added by impregnation.

The main characterization techniques applied were transmission electron microscopy (TEM), temperature programmed reaction (TPReaction), transmission infrared spectroscopy and kinetic studies.

Transmission electron microscopy confirmed that the metal oxides were successfully stabilized on the CNTs. While Bi_2O_3 led to a layered coating of the CNTs, V_2O_5 was attached in a more particulate way to the nanotubes. The V_2O_5 particles on the CNTs with diameters from 5 – 100 nm, had a size distribution varying from 25 to 45 nm. Pd was observed to be homogeneously and finely dispersed on the hybrid samples with particle sizes ranging from 3 to 8 nm. Pd was present on the metal oxides as well as on uncovered CNTs.

TPReaction measurements indicated a high activity of the samples. Over the Pd-Bi_2O_3 containing reference and hybrid samples water, hydrogen, carbon dioxide, methyl formate and dimethyl ether formation was observed, in accordance with the kinetic studies. The trends of product formation were similar on the reference and on the hybrid samples. However, on the hybrid sample reactions set in at about 20 °C lower temperatures. When comparing the Pd-Bi_2O_3 containing samples with a sample of only Pd impregnated on CNTs, very similar reactivities were observed. Only the amount of DME formed was distinctly lower than on the Bi_2O_3 containing samples. Consequently, it was assumed that most reactions proceeded on the Pd particles, except for DME formation, which requires acid sites that can be provided by the metal oxide.

V_2O_5 containing samples were active only at higher temperatures than Bi_2O_3 – based catalysts (~100 °C vs. 70 °C). Concerning the products detected on the vanadium oxide containing samples formaldehyde and dimethoxymethane were observed in addition to the products detected over Bi_2O_3 samples. Dimethoxymethane, however, only formed in a very narrow temperature range; at higher temperature the reaction proceeded in favor of dimethyl ether, which is an intermediate of the dimethoxymethane formation. Comparing the hybrid material with the reference bulk Pd-V_2O_5, as already observed for the Bi_2O_3 containing samples, on the Pd-V_2O_5-CNT sample reactions set in at about 20 °C lower temperatures than on the reference Pd-V_2O_5. An interesting effect concerning the pretreatment temperature was observed over the reference Pd-V_2O_5 sample. When oxidized at 250 °C the catalyst was active at 110 °C, however, after oxidation at 300 °C reactions set in only at ~160 °C. For explaining this shift in the reaction onset temperature because of a different pretreatment temperature two possible causes are proposed: Either a change of the oxidation state of the catalytically active sites or a change in the degree of hydroxylation of the catalyst surface or a combination of both seemed to be imaginable.

Transmission infrared spectroscopic adsorption studies could not be applied to the hybrid materials, because of the strong absorption of the carbon nanotubes. However, since TPReaction measurements and kinetic studies corroborated a very similar behavior of the hybrid materials and the respective reference materials, studies on the reference materials are most probably transferable to the hybrid samples.

CO adsorption studies revealed that CO did not at all adsorb on Bi_2O_3. CO adsorption on the reduced form of Pd-Bi_2O_3, however, resulted in the detection of CO on-top of Pd (2065 cm^{-1}). Bridging CO compounds were not observed, being an indication of small Pd particles on the surface. CO adsorption on pure V_2O_5 at -110 °C revealed CO adsorbed on V^{4+}, V^{3+} and vanadium hydroxyl sites (2204, 2153 and 2173 cm^{-1}). Obviously, CO was able to reduce vanadium sites by self-oxidation to CO_2 despite of the low temperature (-110 °C). On reduced Pd-V_2O_5 a large absorption band at 2147 cm^{-1} was observed assigned to CO bound to V^{3+}. Furthermore, CO adsorbed on-top and bridged to Pd (2094 and 1983 cm^{-1}) were detected on this sample. Oxidized V_2O_5 samples showed bands of overtones of lattice vibrations characteristic of fully oxidized V_2O_5. While these bands vanished after reduction at 250 °C of Pd-V_2O_5, they stayed unchanged in spectra of pure V_2O_5 after reduction at 250 °C. Consequently, it was concluded that Pd decreased the reduction temperature of V to a lower oxidation state.

Methanol adsorption studies on Bi_2O_3 revealed that on the pure oxide only methoxy species were formed. In presence of Pd two further species – formate and dimethyl ether - were

detected at room temperature beside undissociated methanol and methoxy. At higher temperatures (>100 °C) another absorption band at 1740 cm^{-1} appeared, which was assigned to formaldehyde. All other surface species decreased or completely disappeared at higher temperatures. For the methanol adsorption on V_2O_5 only methoxy species were observed on the surface. Addition of Pd entailed only few additional peaks (at 2960, 2882, 1684 and 1264 cm^{-1}) that were all attributed to formaldehyde.

Kinetic studies of methanol oxidation confirmed a high activity of all tested fresh catalysts that contained Pd with conversions up to 90%.

Low temperatures (~100 °C, depending on the sample) and low conversion levels favored a high selectivity towards methyl formate. Increasing the reaction temperature entailed higher conversion and an increasing selectivity towards the total oxidation product CO_2. Long-term measurements indicated a high stability of the catalysts under reaction conditions; however, several pretreatment cycles at 250 °C both under oxidizing and reducing conditions lead to a deactivation of the catalysts. Bi_2O_3 containing samples deactivated more slowly than V_2O_5 containing samples. The latter were completely deactivated after several heating cycles. Again changes in oxidation state and surface hydroxylation degree could be the reason for this.

The idea that CNTs as catalyst support would reduce local hot spots due to the exothermic reactions could not be proven with the techniques applied. However, comparison with commercial bulk oxides showed that hybrid materials were active already at lower temperatures.

The origin of deactivation of the samples is not clear yet. Further investigations on the properties and state of the catalysts upon reduction or oxidation may help to understand the ongoing processes.

The addition of water to the reaction feed and / or during pretreatment was suggested to help stabilizing the active site of vanadium containing catalysts for selective oxidation reactions. First tests based on this approach seem to be promising.

Another open question concerns the proper pretreatment conditions to reactivate the catalysts. Again water addition could be a promising strategy for this.

6 Abbreviations

CEM: Channel Electron Multiplier

CNT(s): carbon nanotube(s)

DME: dimethylether

DMFC: direct methanol fuel cell

DMM: dimethoxymethane

EDX: X-ray energy dispersive spectrometry

FA: formaldehyde

FID: Flame Ionisation Detector

GC: gas chromatograph(y)

MeOH: methanol

MFA: methyl formate

MS: mass spectrometer

ox.: oxidizing pretreatment

red.: reducing pretreatment

SEM: Secondary Electron Multiplier

TEM: Transmission Electron Microscope (Microscopy)

TCD: Thermal Conductivity Detector

TPD: Temperature Programmed Desorption

TPO: Temperature Programmed Oxidation

TPR: Temperature Programmed Reduction

TPReaction: Temperature Programmed Reaction

XRD: X-ray diffraction

Sample Designation:

sample name	content		
	organic compound	metal oxide	metal
Pd-V_2O_5	-	V_2O_5	2 wt% Pd*
Pd-Bi_2O_3	-	Bi_2O_3	2 wt% Pd*
V_2O_5-CNT	CNT	V_2O_5	-
Bi_2O_3-CNT	CNT	Bi_2O_3	-
Pd-V_2O_5-CNT	CNT	V_2O_5	2 wt% Pd*
Pd-Bi_2O_3-CNT	CNT	Bi_2O_3	2 wt% Pd*
Pd-CNT	CNT		2 wt% Pd*

*percentage refers to the sample mass without Pd

7 Attachment

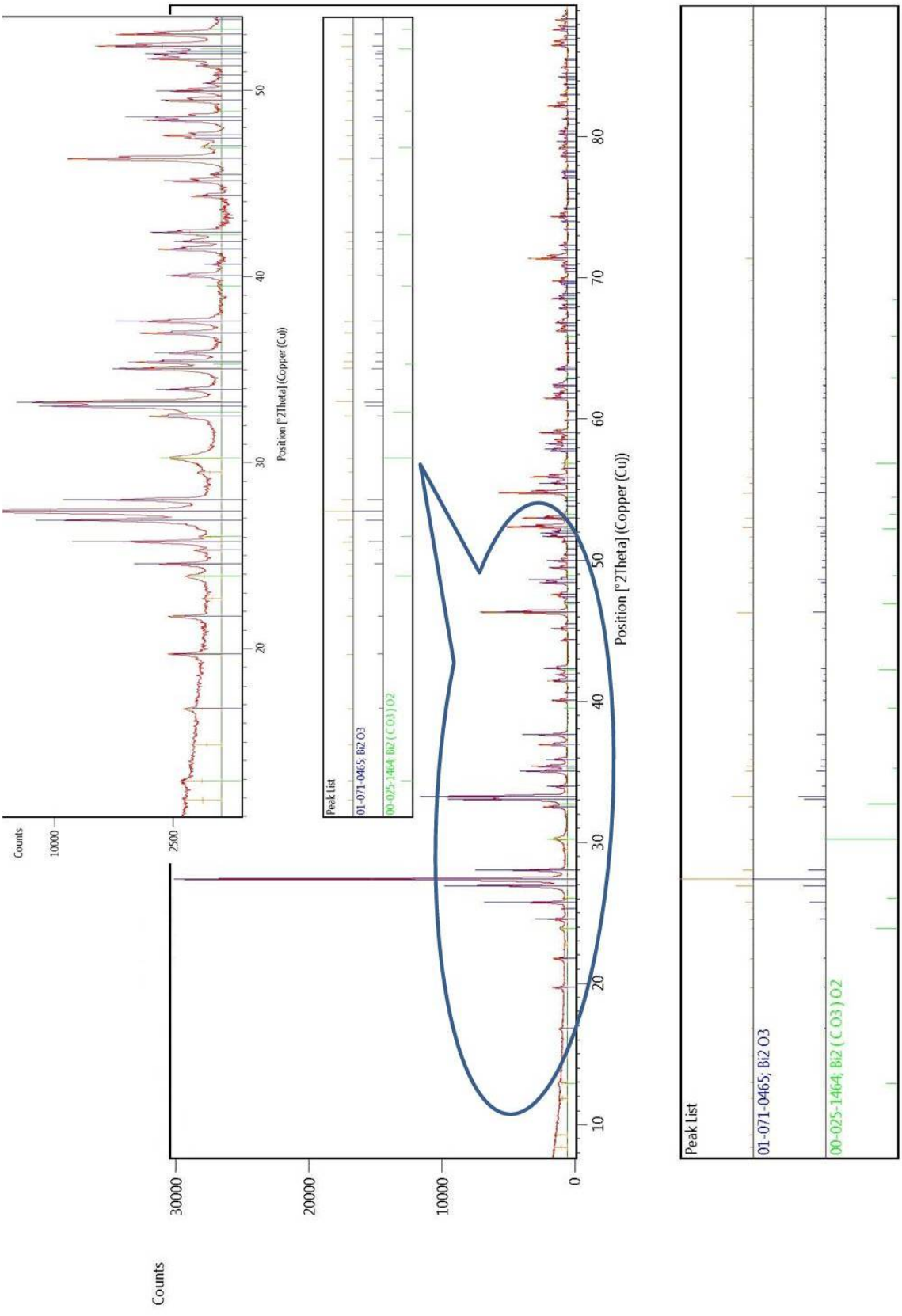

Figure 7.1: XRD pattern of Bi_2O_3

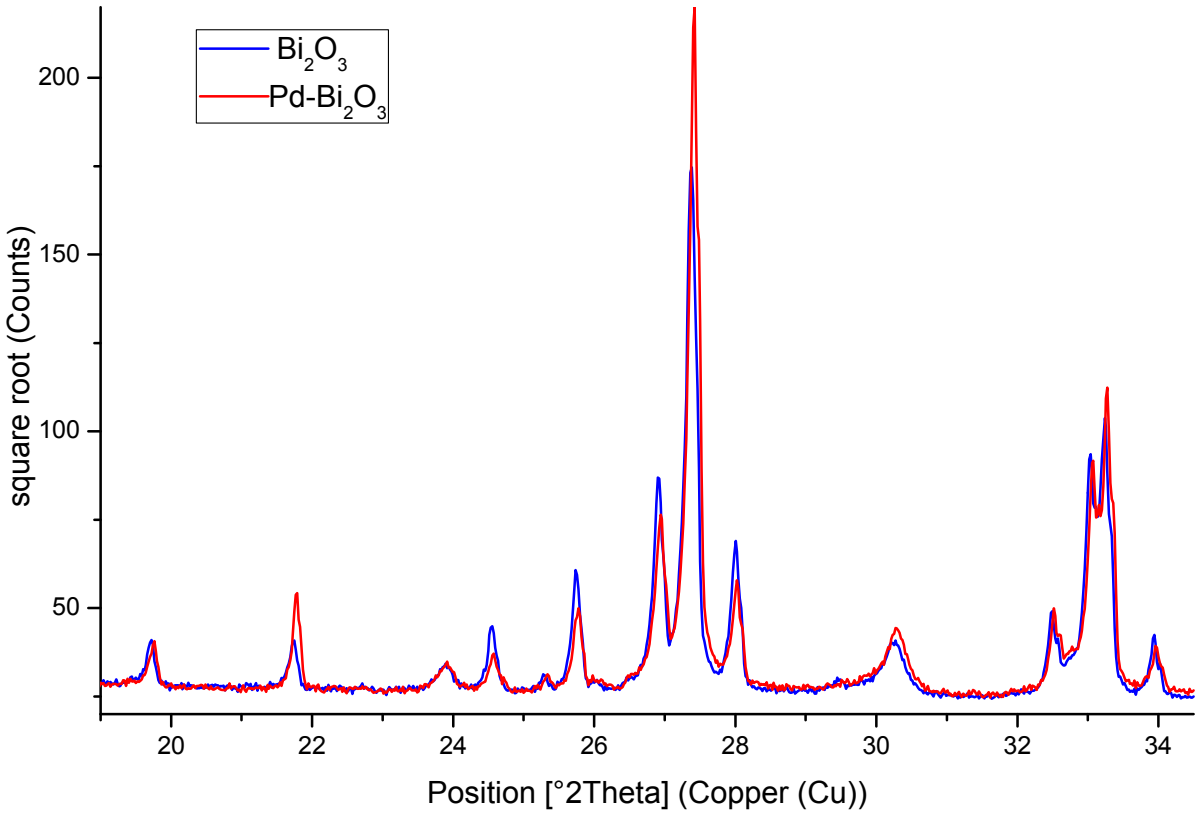

Figure 7.2: Comparison of XRD patterns of Bi_2O_3 and Pd-Bi_2O_3.

8 Literature

1. Nic, M.;Jirat, J. and Kosata, B.: *IUPAC. Compendium of Chemical Terminology (the "Gold Book")*. **1997**, A. D. McNaught and A. Wilkinson. Blackwell Scientific Publications: Oxford.
2. Lindstroem, B. and Pettersson, L. J.: *A brief history of catalysis.* CATTECH, **2003**, 7, p. 130-138.
3. Haber, J.: *The Role of Catalysis in Determining Men's Quality of Life.* Top. Catal., **2009**, 52, p. 970-981.
4. Huang, H. J.;Sun, D. P. and Wang, X.: *PtCo alloy nanoparticles supported on graphene nanosheets with high performance for methanol oxidation.* Chin. Sci. Bull., **2012**, 57, p. 3071-3079.
5. Kaichev, V. V.;Miller, A. V.;Prosvirin, I. P. and Bukhtiyarov, V. I.: *In situ XPS and MS study of methanol decomposition and oxidation on Pd(111) under millibar pressure range.* Surf. Sci., **2012**, 606, p. 420-425.
6. Forzatti, P.;Tronconi, E.;Elmi, A. S. and Busca, G.: *Methanol oxidation over vanadia-based catalysts.* Appl. Catal., A, **1997**, 157, p. 387-408.
7. Behera, G. C. and Parida, K.: *Selective gas phase oxidation of methanol to formaldehyde over aluminum promoted vanadium phosphate.* Chem. Eng. J. (Amsterdam, Neth.), **2012**, 180, p. 270-276.
8. Papes, F. A. C. and Maciel, F. R.: *Hybrid training approach for artificial neural networks using genetic algorithms for rate of reaction estimation: Application to industrial methanol oxidation to formaldehyde on silver catalyst.* Chem. Eng. J. (Amsterdam, Neth.), **2010**, 157, p. 501-508.
9. Roeper, M.: *Oxygenated base chemicals from synthesis gas. Methyl formate as a versatile intermediate.* Erdoel Kohle, Erdgas, Petrochem., **1984**, 37, p. 506-11.
10. Tronconi, E.;Elmi, A. S.;Ferlazzo, N.;Forzatti, P.;Busca, G. and Tittarelli, P.: *Methyl formate from methanol oxidation over coprecipitated V-Ti-O catalysts.* Ind. Eng. Chem. Res., **1987**, 26, p. 1269-75.
11. Elmi, A. S.;Tronconi, E.;Cristiani, C.;Gomez, M. J. P.;Forzatti, P. and Busca, G.: *Mechanism and active sites for methanol oxidation to methyl formate over coprecipitated vanadium-titanium oxide catalysts.* Ind. Eng. Chem. Res., **1989**, 28, p. 387-93.
12. Prado, N. T.;Nogueria, F. G. E.;Nogueira, A. E.;Nunes, C. A.;Diniz, R. and Oliveira, L. C. A.: *Modified Niobia As a New Catalyst for Selective Production of Dimethoxymethane from Methanol.* Energy Fuels, **2010**, 24, p. 4793-4796.

13. Ren, Y.;Huang, Z.;Jiang, D.;Liu, L.;Zeng, K.;Liu, B. and Wang, X.: *Combustion characteristics of a compression-ignition engine fueled with diesel-dimethoxy methane blends under various fuel injection advance angles.* Appl. Therm. Eng., **2005**, 26, p. 327-337.
14. Sinha, A. and Thomson, M. J.: *The chemical structures of opposed flow diffusion flames of C3 oxygenated hydrocarbons (isopropanol, dimethoxy methane, and dimethyl carbonate) and their mixtures.* Combust. Flame, **2004**, 136, p. 548-556.
15. Lide, D. R.: ed. *Handbook of Chemistry and Physics*. 86th ed. 86th Edition 2005-2006. **2005**, Taylor & Francis Group: New York.
16. Eder, D.: *Carbon Nanotube-Inorganic Hybrids.* Chem. Rev. (Washington, DC, U. S.), **2010**, 110, p. 1348-1385.
17. Kickelbick, G.: *Introduction to Hybrid Materials*. in *Hybrid Materials*. **2007**, Wiley-VCH Verlag GmbH & Co. KGaA. p. 1-48.
18. Gómez-Romero, P. and Sanchez, C.: *Hybrid Materials, Functional Applications. An Introduction*. in *Functional Hybrid Materials*. **2005**, Wiley-VCH Verlag GmbH & Co. KGaA. p. 1-14.
19. Terrones, M.: *Science and Technology of the twenty-first century: Synthesis, Properties and Applications of Carbon Nanotubes.* Annu. Rev. Mater.Res., **2003**, 33, p. 419-501.
20. Ajayan, P. M.: *Nanotubes from Carbon.* Chem. Rev. (Washington, D. C.), **1999**, 99, p. 1787-1799.
21. Dresselhaus, M. S.;Dresselhaus, G. and Avouris, P.: *Carbon Nanotubes: Synthesis, Structure, Properties and Applications*. **2001**, New York: Springer Verlag Berlin-Heidelberg.
22. Eder, D. and Windle, A. H.: *Carbon-inorganic hybrid materials: the carbon-nanotube/TiO2 interface.* Adv. Mater. (Weinheim, Ger.), **2008**, 20, p. 1787-1793.
23. Klein, K. L.;Melechko, A. V.;McKnight, T. E.;Retterer, S. T.;Rack, P. D.;Fowlkes, J. D.;Joy, D. C. and Simpson, M. L.: *Surface characterization and functionalization of carbon nanofibers.* J. Appl. Phys., **2008**, 103, p. 061301/1-061301/26.
24. Fu, K. and Sun, Y.-p.: *Dispersion and solubilization of carbon nanotubes.* J. Nanosci. Nanotechnol., **2003**, 3, p. 351-364.
25. Xie, X.-L.;Mai, Y.-W. and Zhou, X.-P.: *Dispersion and alignment of carbon nanotubes in polymer matrix: A review.* Materials Science and Engineering: R: Reports, **2005**, 49, p. 89-112.
26. Tasis, D.;Tagmatarchis, N.;Bianco, A. and Prato, M.: *Chemistry of Carbon Nanotubes.* Chem. Rev. (Washington, DC, U. S.), **2006**, 106, p. 1105-1136.

27. Whitsitt, E. A.;Moore, V. C.;Smalley, R. E. and Barron, A. R.: *LPD silica coating of individual single walled carbon nanotubes.* J. Mater. Chem., **2005**, 15, p. 4678-4687.
28. Han, L.;Wu, W.;Kirk, F. L.;Luo, J.;Maye, M. M.;Kariuki, N. N.;Lin, Y.;Wang, C. and Zhong, C.-J.: *A Direct Route toward Assembly of Nanoparticle-Carbon Nanotube Composite Materials.* Langmuir, **2004**, 20, p. 6019-6025.
29. Correa-Duarte, M. A. and Liz-Marzan, L. M.: *Carbon nanotubes as templates for one-dimensional nanoparticle assemblies.* J. Mater. Chem., **2006**, 16, p. 22-25.
30. Satake, A.;Miyajima, Y. and Kobuke, Y.: *Porphyrin-Carbon Nanotube Composites Formed by Noncovalent Polymer Wrapping.* Chem. Mater., **2005**, 17, p. 716-724.
31. Wang, X.;Liu, Y.;Qiu, W. and Zhu, D.: *Immobilization of tetra-tert-butylphthalocyanines on carbon nanotubes: a first step towards the development of new nanomaterials.* J. Mater. Chem., **2002**, 12, p. 1636-1639.
32. Chen, R. J.;Zhang, Y.;Wang, D. and Dai, H.: *Noncovalent sidewall functionalization of single-walled carbon nanotubes for protein immobilization.* J. Am. Chem. Soc., **2001**, 123, p. 3838-3839.
33. Schubert, U. and Hüsing, N.: *Synthesis of Inorganic Materials*. Third, Completely Revised and Updated Edition ed. **2012**, Weinheim: Wiley-VCH.
34. Williams, D. B. and Carter, C. B.: *Transmission Electron Microscopy*. 2nd ed. **2009**, New York: Springer Science+Business Media.
35. Thomas, G. and Goringe, M. J.: *Transmission Electron Microscopy of Materials*. **1979**, New York: John Wiley & Sons
36. Hunter, E. E.: *Practical Electron Microscopy: A Beginners Illustrated Guide*. **1993**: Cambridge University Press.
37. Colthup, N. B.;Daly, L. H. and Wiberley, S. E.: *Introduction to Infrared and Raman Spectroscopy*. Third Edition ed. **1990**: Academic Press, Inc.
38. Niemantsverdriet, J. W.: *Spectroscopy in Catalysis. An Introduction*. **1993**, Weinheim: VCH Verlagsgesellschaft mbH.
39. Engel, T. and Reid, P.: *Physikalische Chemie*. **2006**, München: Pearson Studium.
40. Jackson, S. D.;Hargreaves, J. S. J. and Editors: *Metal Oxide Catalysis; Volume 1*. **2009**: Wiley-VCH Verlag GmbH & Co. KGaA. 485 pp.
41. Cammann, K.: *Instrumentelle Analytische Chemie* **2001**, Heidelberg: Spektrum Akademischer Verlag.
42. Available from: http://www.chm.bris.ac.uk, downloaded on 27.09.2012
43. Allen, J. S.: *The Detection of Single Positive Ions, Electrons and Photons by a Secondary Electron Multiplier.* Physical Review, **1939**, 55, p. 966-971.

44. Heroux, L. and Hinteregger, H. E.: *Resistance Strip Magnetic Photomultiplier for the Extreme Ultraviolet.* Review of Scientific Instruments, **1960**, 31, p. 280-286.
45. Burroughs, E. G.: *Collection Efficiency of Continuous Dynode Electron Multiple Arrays.* Review of Scientific Instruments, **1969**, 40, p. 35-37.
46. Grob, R. L.: *Modern Practice of Gas Chromatography*. Fourth Edition ed, ed. Grob, R. L. and Barry, E. F. **2004**, New Jersey: John Wiley & Sons, Inc.
47. Dieterle, D. J.: *Nanocarbon Metal Oxide Hybrids as new Catalysts for Selective Oxidation Reactions*. Westfälische Wilhelms-Universität Münster, 2012
48. Haghofer, A.;Foettinger, K.;Girgsdies, F.;Teschner, D.;Knop-Gericke, A.;Schloegl, R. and Rupprechter, G.: *In situ study of the formation and stability of supported Pd2Ga methanol steam reforming catalysts.* J. Catal., **2012**, 286, p. 13-21.
49. Lear, T.;Marshall, R.;Lopez-Sanchez, J. A.;Jackson, S. D.;Klapotke, T. M.;Baumer, M.;Rupprechter, G.;Freund, H.-J. and Lennon, D.: *The application of infrared spectroscopy to probe the surface morphology of alumina-supported palladium catalysts.* J. Chem. Phys., **2005**, 123, p. 174706/1-174706/13.
50. Bertarione, S.;Scarano, D.;Zecchina, A.;Johanek, V.;Hoffmann, J.;Schauermann, S.;Libuda, J.;Rupprechter, G. and Freund, H.-J.: *Surface reactivity of Pd nanoparticles supported on polycrystalline substrates as compared to thin film model catalysts: infrared study of CH3OH adsorption.* J. Catal., **2004**, 223, p. 64-73.
51. Busca, G.;Ramis, G. and Lorenzelli, V.: *FT-IR study of the surface properties of polycrystalline vanadia.* J. Mol. Catal., **1989**, 50, p. 231-40.
52. Busca, G. and Lavalley, J. C.: *Use of overtone bands to monitor the state of the catalyst active phases during infrared studies of adsorption and catalytic reactions.* Spectrochim. Acta, Part A, **1986**, 42A, p. 443-5.
53. Concepcion, P.;M. Reddy, B. and Knozinger, H.: *FTIR study of low-temperature CO adsorption on pure Al2O3-TiO2 and V/Al2O3-TiO2 catalysts.* Physical Chemistry Chemical Physics, **1999**, 1, p. 3031-3037.
54. Concepcion, P.;Hadjiivanov, K. and Knozinger, H.: *Low-Temperature CO Adsorption on V-Containing Aluminophosphates: An FTIR Study.* J. Catal., **1999**, 184, p. 172-179.
55. Jonson, B.;Rebenstorf, B.;Larsson, R.;Andersson, S. L. T. and Lundin, S. T.: *Activity measurements and spectroscopic studies of the catalytic oxidation of toluene over V2O5/Al2O3-C catalysts.* Journal of the Chemical Society, Faraday Transactions 1: Physical Chemistry in Condensed Phases, **1986**, 82, p. 767-783.

56. Jonson, B.;Rebenstorf, B. and Larsson, R.: *An infrared spectroscopic investigation on carbon monoxide adsorbed on silica-supported vanadocene.* Acta Chem. Scand., Ser. A, **1988**, A42, p. 156-64.

57. Burcham, L. J.;Briand, L. E. and Wachs, I. E.: *Quantification of Active Sites for the Determination of Methanol Oxidation Turn-over Frequencies Using Methanol Chemisorption and in Situ Infrared Techniques. 2. Bulk Metal Oxide Catalysts.* Langmuir, **2001**, 17, p. 6175-6184.

58. Busca, G.: *On the mechanism of methanol oxidation over vanadia-based catalysts: a FT-IR study of the adsorption of methanol, formaldehyde and formic acid on vanadia and vanadia-silica.* J. Mol. Catal., **1989**, 50, p. 241-9.

59. Busca, G.;Rossi, P. F.;Lorenzelli, V.;Benaissa, M.;Travert, J. and Lavalley, J. C.: *Microcalorimetric and Fourier transform infrared spectroscopic studies of methanol adsorption on alumina.* J. Phys. Chem., **1985**, 89, p. 5433-9.

60. Sanchez-Escribano, V.;Larrubia, V. M. A.;Finocchio, E. and Busca, G.: *On the mechanisms and the selectivity determining steps in syngas conversion over supported metal catalysts: An IR study.* Appl. Catal., A, **2006**, 316, p. 68-74.

61. Larrubia, V. M. A.;Busca, G.;Costantino, U.;Marmottini, F.;Montanari, T.;Patrono, P.;Pinzari, F. and Ramis, G.: *An IR study of methanol steam reforming over ex-hydrotalcite Cu-Zn-Al catalysts.* J. Mol. Catal. A: Chem., **2007**, 266, p. 188-197.

62. Vohs, J.: *Landolt-Börnstein New Series III/42A3*, Springer-Verlag GmbH.

63. Gazsi, A.;Ugrai, I. and Solymosi, F.: *Production of hydrogen from dimethyl ether on supported Au catalysts.* Appl. Catal., A, **2011**, 391, p. 360-366.

64. Haghofer, A.;Ferri, D.;Foettinger, K. and Rupprechter, G.: *Who Is Doing the Job? Unraveling the Role of Ga2O3 in Methanol Steam Reforming on Pd2Ga/Ga2O3.* ACS Catal., Ahead of Print.

65. Rupprechter, G.: *A surface science approach to ambient pressure catalytic reactions.* Catal. Today, **2007**, 126, p. 3-17.

66. Busca, G.;Lamotte, J.;Lavalley, J. C. and Lorenzelli, V.: *FT-IR study of the adsorption and transformation of formaldehyde on oxide surfaces.* J. Am. Chem. Soc., **1987**, 109, p. 5197-202.

67. Jaeger, T. D.;Fielicke, A.;von, H. G.;Meijer, G. and Duncan, M. A.: *Infrared spectroscopy of water adsorption on vanadium cluster cations (V+x; x=3-18).* Chem. Phys. Lett., **2004**, 392, p. 409-414.

68. Jehng, J.-M.;Deo, G.;Weckhuysen, B. M. and Wachs, I. E.: *Effect of water vapor on the molecular structures of supported vanadium oxide catalysts at elevated temperatures.* J. Mol. Catal. A: Chem., **1996**, 110, p. 41-54.

69. Frank, B.;Fortrie, R.;Hess, C.;Schloegl, R. and Schomaecker, R.: *Reoxidation dynamics of highly dispersed VOx species supported on γ-alumina.* Appl. Catal., A, **2009**, 353, p. 288-295.